UNIVERSITY OF SOUTHAMPTON

FACULTY OF ENGINEERING AND PHYSICAL SCIENCES

Electronics and Computer Science

Repetitive Control and Electrode Array Pattern Selection for FES-based Drop-Foot Assistance

by

Aaron Peter Page

Thesis Submitted for the degree of Doctor of Philosophy

September 2020

UNIVERSITY OF SOUTHAMPTON

ABSTRACT

FACULTY OF ENGINEERING AND PHYSICAL SCIENCES
Electronics and Computer Science

Doctor of Philosophy

REPETITIVE CONTROL AND ELECTRODE ARRAY PATTERN SELECTION FOR FES-BASED DROP-FOOT ASSISTANCE

by Aaron Peter Page

Drop-foot is a problem resulting from a range of neurological conditions. It is currently diagnosed in over 3 million people worldwide. Current technologies addressing Drop-foot have significant limitations, with 30% of people rejecting the established mechanical solutions due to; muscle wastage, size, noise and damage to dignity. Alternatively, Functional Electrical Stimulation (FES) is a technology, which addresses the condition by directly recruiting the user's muscles. This overcomes significant issues such as muscle wastage or restriction of freedom. However, it has limitations which include increased rate of fatigue in users, dependence on pad positions, and limited battery life. Further to this, the control of FES commercially is very crude, often leading to jerky or unnatural motion. More advanced controllers exist in the academic domain, but they assume that gait can be modelled as a resetting motion, require large amounts of data, or are unsuitable for clinical application due to problems in demonstrating stability.

This thesis focuses on overcoming the limitation of current FES technology for drop-foot. It develops, simulates and applies a new form of closed-loop controller for FES that addresses the limitations of previous systems. In particular, this controller is a form of Repetitive Control (RC), which learns over the periodic nature of gait, does not assume resetting, reduces the data needed between periods, and has clear stability conditions. Simulations show that the 'point-to-point' generalisation of RC improves the convergence speed and robustness while only slightly decreasing the tracking accuracy of the entire reference. Experimental validation confirms that tracking accuracy is improved between $52\% - 140\%$ compared to existing drop-foot controllers, with a reduction in data used of 94%, compared to traditional RC. To address the challenge of pad placement, a framework to identify an optimal pad 'pattern' from thousands of pad combinations has been developed. Iterative learning control is then applied to tune the simulation levels for a static gesture. This was achieved with an error of $2.2° \pm 1.23°$. Applying commercially inspired constraints restricted the pool of patterns and enabled an investigation into hardware and software simplifications for a commercial device.

Contents

List of Figures

List of Tables

Declaration of Authorship

I, Aaron Peter Page , declare that the thesis entitled *Repetitive Control and Electrode Array Pattern Selection for FES-based Drop-Foot Assistance* and the work presented in the thesis are both my own, and have been generated by me as the result of my own original research. I confirm that:

- this work was done wholly or mainly while in candidature for a research degree at this University;
- where any part of this thesis has previously been submitted for a degree or any other qualification at this University or any other institution, this has been clearly stated;
- where I have consulted the published work of others, this is always clearly attributed;
- where I have quoted from the work of others, the source is always given. With the exception of such quotations, this thesis is entirely my own work;
- I have acknowledged all main sources of help;
- where the thesis is based on work done by myself jointly with others, I have made clear exactly what was done by others and what I have contributed myself;
- parts of this work have been published as: Page et al. (2018a,b); Page and Freeman (2020)

Signed:.....

Date:.....

Acknowledgements

First, I would like to thank my supervisor, Dr Chris Freeman, for his outstanding guidance, patience, and encouragement throughout my studies.

A special thanks to all participants, who modestly exchanged many hours in the lab, to help further our collective understanding of Functional Electrical Stimulation, for a couple of biscuits.

A huge thank you to all of my friends, especially those in the Southampton University Chinese Kickboxing Society who have provided me with numerous opportunities to release stress and frustration. As well as my colleague's at the Careers and Employability Center, I had the utmost pleasure getting to know everyone and I wish you all the best in the future.

I would also like to thank my dearest family, especially my wonderful sister, for their unwavering support, love and encouragement throughout my studies.

The financial support of the Engineering and Physical Sciences Research Council is gratefully acknowledged.

Finally, to everyone, who had even the smallest influence upon my work, thank you for helping make this all possible.

Nomenclature

P	Discrete plant
$A/\boldsymbol{A}$	State-space dynamics: state matrix (unlifted/lifted)
$B/\boldsymbol{B}$	State-space dynamics: input matrix (unlifted/lifted)
$C/\boldsymbol{C}$	State-space dynamics: output matrix (unlifted/lifted)
$D/\boldsymbol{D}$	State-space dynamics: feed-through matrix (unlifted/lifted)
m	Number of inputs
ϑ	Number of outputs
n_p	Number of states (of the plant)
x_p	State vectour (of the plant)
i	Sample
N	Cycle length
$u/\boldsymbol{u}$	Input (stimulation) (unlifted/lifted)
$y/\boldsymbol{y}$	Output (ankle angle) (unlifted/lifted)
$r/\boldsymbol{r}$	Reference (gait cycle) (unlifted/lifted)
k	Cycle number
q	One sample advance operator
$Q/\boldsymbol{Q}$	Robustness filter (unlifted/lifted)
$L/\boldsymbol{L}$	Learning filter (unlifted/lifted)
$e/\boldsymbol{e}$	Error (unlifted/lifted)
I	Identity matrix
M	Number of extracted and tracked point-to-point indices
$\boldsymbol{\Phi}$	Point-to-point projection operator
$\boldsymbol{s}$	Any lifted signal
β	Learning rate
a, b, c	Variables
$\boldsymbol{F}$	Filter to generalise minimum control effort
$\boldsymbol{H}$	Minimum control effort weighting
λ	Lagrangian multiplier
n_f	Number of states (of the filter)
p	Number of joints
n	Number of pads in a pattern

Chapter 1

Introduction

Drop-foot is a muscular weakness or paralysis that makes it difficult to raise the foot. However, it is a sign of an underlying problem rather than a condition itself. Drop-foot can be caused by; muscular damage, nerve damage, or the result of a brain or spinal injury (Graham, 2010; Westhout et al., 2007). Over 100,000 people (King, 2015) in the UK suffer from first-time strokes each year, with 20% of these developing drop-foot (Barrett and Taylor, 2010). It causes instability around the ankle and limits the ability to raise the foot while walking. This leads to a slow, tiring, abnormal gait with an increased probability of falls (Peterson, 2007). There are various commercially available technologies to assist with drop-foot. The simplest devices are canes, walking frames and passive mechanical orthoses which lock the foot in position. Although falls due to drop-foot are reduced, mechanical orthoses have high rejection rates as they promote muscle wastage leading to further ankle instability. The most prevalent assistive devices employ Functional Electrical Stimulation (FES) which is delivered via an implanted or surface electrode causing artificial muscle contraction. Systematic reviews and meta-analyses have concluded FES has a positive effect on activity, specifically increasing walking speed post-stroke (Howlett et al., 2015; Miller et al., 2017).

1.1 Research Motivation

Although prevalent, commercially available FES devices use simple ramping signals, initialised by a heel switch, to raise the foot. However, these do not produce movements that correspond to healthy, natural gait, and often use higher levels of stimulation than necessary. Iterative Learning Control (ILC) is an approach which has been able to produce more natural movements by combining a model of the underlying muscle dynamics with learning from experience (Longman, 2000; Pipeleers and Moore, 2014; Wang et al., 2009). ILC was applied to drop-foot in Seel et al. (2016) and out-performed existing methodologies. However, ILC assumes that the reference (gait) signal resets to a fixed

value after every task (step). It also requires large amounts of sensory data to be stored between trials. This motivates the need for a control framework that does not require resetting between tasks, while still utilising an underlying muscle model and learning from experience. This thesis addresses the need by applying a framework termed Repetitive Control (RC), to the problem of drop-foot, for the first time. It also undertakes a substantial expansion to the approach by extracting and tracking only a subset of points in the reference. This not only reduces the number of data points used but also the amount of data stored and shared between cycles. A substantial generalisation was then performed to allow the minimum control effort to be altered, i.e. allow the solution to converge to the minimum velocity, jerk or acceleration norms. By choosing to minimise effort, in the same way as the human body does naturally, the replication of a natural gait pattern is improved. A method to apply weightings to individual points within the gait pattern is then explored, offering the designer greater control over the convergence of the input and output signals.

Another problem is that commercial FES systems for drop-foot commonly use a small number of surface electrodes which are challenging and time-consuming to place (Taylor et al., 1999; Heller et al., 2013a). These also provide poor muscle selectivity, reducing fine movement control and leading to increased rates of fatigue (Li-Wei and Binder-Macleod, 2007). Multiple surface electrodes have been used by several research groups to form arrays able to address the problem. Here arrays allow for arbitrary placement and automation of the trial and error approach to select a suitable stimulation site. However, existing pad identification methods (e.g. Schill et al. (2009); O'Dwyer et al. (2006); Micera et al. (2010); Popović-Bijeli et al. (2005)) use a simplistic approach. The approach activates each pad within the array in turn. The pad with the best movement characteristics (e.g. greatest dorsiflexion, least roll) is selected. Although minor variations exist, they are all slow and imprecise. They also do not consider more complex patterns (e.g. a greater number of pads with different stimulation levels). This thesis develops an automatic test procedure to identify more general 'patterns' comprising of multiple electrodes with different stimulation levels that minimise a cost. By fusing the same idea of learning from experience, with an underlying model, a large number of pad patterns are evaluated, without the need for direct application (Illingworth, 1991). Here, ILC is fused with a set of constraints specially designed to restrict the search space in ways that correspond with potential hardware and manufacturing simplifications. These hardware simplifications have also been found to improve user comfort, set-up time and fine joint control.

1.2 Research Contribution and Structure of Thesis

This work has generated a number of key contributions, several of which have been published in conference and journal papers:

- The generalisation of repetitive control to extract and track only a subset of points within a reference, select the minimum control effort and prioritise individual points through weightings.
  - A. P. Page, C. T. Freeman and B. Chu, "Point-to-Point Repetitive Control with Application to Drop-Foot," IEEE, European Control Conference (ECC), Limassol, 2018, pp. 2399-2404.
  - A. P. Page, C. T. Freeman and B. Chu, "Weighted Point-to-Point Repetitive Control for Drop-Foot Assistance," UKACC 12th International Conference on Control (CONTROL), Sheffield, 2018, pp. 468-473.
- The first application of repetitive control to functional electrical stimulation for drop-foot. Experimental results directly evaluating the performance of point-to-point RC (error $2.99^\circ \pm 0.99^\circ$) with traditional RC formulation (error $2.56^\circ \pm 0.76^\circ$) and indirectly with various control strategies.
  - A. P. Page and C. T. Freeman, "Point-to-Point Repetitive Control of Functional Electrical Stimulation for Drop-Foot," Control Engineering Practice, 2020, 96, 104280. doi:10.1016/j.conengprac.2019.104280 (Impact Factor: 3.232)
- The first time an electrode array has been embedded into a wearable sock sleeve.
- A model-based iterative learning control for pad pattern selection with a set of commercially inspired constraints achieving an improvement of 628% compared to a traditional 1-element pattern and an average model error of $6.23^\circ \pm 3.6^\circ$ for 2-degrees of freedom across all 20 constraints.
  - A. P. Page and C. T. Freeman, "ILC for Electrode Array Pattern Selection," 21st IFAC World Congress, Berlin, 2020, Accepted.

The thesis structure is as follows; Chapter 2 briefly compares healthy gait with drop-foot gait, before critically reviewing current technologies and establishing limitations. It is shown that the approach that has had the most success in assisting drop-foot is FES.

Chapter 3 provides a detailed background about natural and artificially invoked motor function. Controllable inputs for FES are introduced, followed by a comprehensive review of available control approaches.

Chapter 4 introduces repetitive control and derives a substantial generalisation of the repetitive control update. Allowing; a subset of points to be extracted and tracked, the minimum energy properties of the controller to be altered, and a weighted extension to priorities points.

Chapter 5 performs the first validation of the control framework through multiple simulations focusing on convergence speed, robustness and tracking accuracy.

Chapter 6 first develops the model identification procedure required to produce a model of the system for the repetitive controller. The controller is then applied experimentally to control FES for drop-foot. The study includes five healthy participants. The ability to track and maintain the desired reference despite time-varying non-linearities is demonstrated. The repeatability, convergence speed, robustness and tracking error are also quantified and compared.

Chapter 7 explores pad pattern identification. It does this by developing commercially inspired constraints that restrict the shape, size and stimulation relationship between pads, leading to simplifications in hardware and software. A model-based iterative learning control, utilising superposition, selects multiple pads to produce a pattern. Experimental results investigate the model error and the effect of constraints on joint positions and their corresponding stimulation levels.

Chapter 8 outlines the remaining challenges and future considerations within the field, with a specific focus on how the contributions made here can be utilised. Additionally, the new research pathways available to explore because of this research are also discussed.

The appendices include the additional work relating to outreach with the general public, which includes contributing to the 'Right Trousers Project', presenting at a press conference for the 2018 Britsh Science Festival in Hull and exhibiting at the 'Trouser Fest' festival at the Bristol Robotic Labs. Additional information regarding the gait cycle and figures not presented in the main body are also included.

Chapter 2

Drop-foot Technologies

This chapter provides an overview of drop-foot, particularly focusing on its effect on normal gait and its impact on the quality of life. Current technologies available to support people with the condition are discussed, and their effectiveness is then critically reviewed.

2.1 Introduction to Drop-Foot

Stroke, Multiple Sclerosis (MS), Cerebral Palsy (CP) and Charcot-Marie-Tooth disease are all neurological conditions that affect the central and peripheral nervous systems. Neurological conditions often lead to difficulty in lifting the foot. This is called drop-foot. Drop-foot affects approximately 20% of people who have experienced strokes (Barrett and Taylor, 2010). This results in over 122,000 people in the US, and 11,400 people in the UK, developing the condition each year. This equates to approximately 3 million people worldwide currently living with the condition. Drop-foot prevents normal leg swing during gait, leading to abnormal, inefficient motion and an increased risk of falling. Studies show that 63% of people with MS fear falling, 83% thus avoid activity (Peterson, 2007) and 51% of people with stroke fell at least once within the last 12 months (Hyndman et al., 2002).

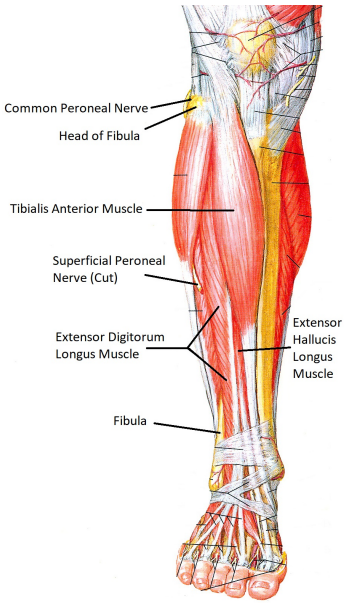

Figure 2.1: Lower leg anatomy.

Full recovery from drop-foot, if due to damage to the neurological pathways that control the common peroneal nerve, may not be possible. The peroneal nerve supplies the

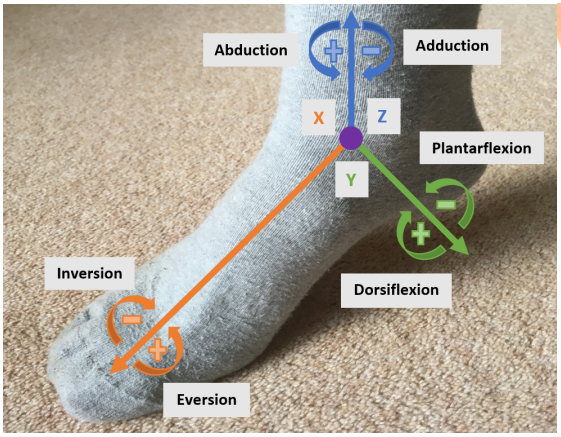

Figure 2.2: Illustrative picture of Drop-foot

Figure 2.3: Diagram showing degrees of freedom around the ankle

front (anterior) and sides (lateral) of the leg. It is responsible for producing dorsiflexion (lifting the foot around the y-axis) which is controlled by the tibialis anterior, extensor hallucis longus and extensor digitorum longus muscles. It also produces inversion/eversion (rotation around the x-axis) which is controlled by the hallucis and digitorum muscles. Figure 2.3 shows the degrees of freedom around the ankle, while Figure 2.2 shows that damage to the peroneal nerve reduces dorsiflexion. To better describe the damage drop-foot causes to gait an overview of healthy gait is now given.

2.2 Human Gait

Although the walking mechanism may appear automatic and easy to most, it is a complex and high-level motor function, requiring hundreds of muscles across the upper and lower body working in synchronous harmony. Human gait is characterised by an inverted pendulum movement, in which the centre of gravity moves over a contracted leg with each step.

2.2.1 Healthy Gait

Gait is a dynamic, periodic, cyclic, time-varying and continuous motion. The dynamic and continuous nature of gait means that the gait cycle is often normalised and expressed as a percentage, between 0% and 100%. Gait is commonly split into a stance (first 60% of motion) and swing (the remaining 40 % of motion). This can then be further partitioned into eight distinct sections (Zhang et al., 2012). By amalgamating experimental results from Postans and Granat (2005) and Neptune and Sasaki (2005), a full human gait cycle for the ankle is shown in Figure 2.4. Although gait periods vary, an average of 2 seconds is commonly assumed. Further details about each event within the cycle are contained in Appendix B.

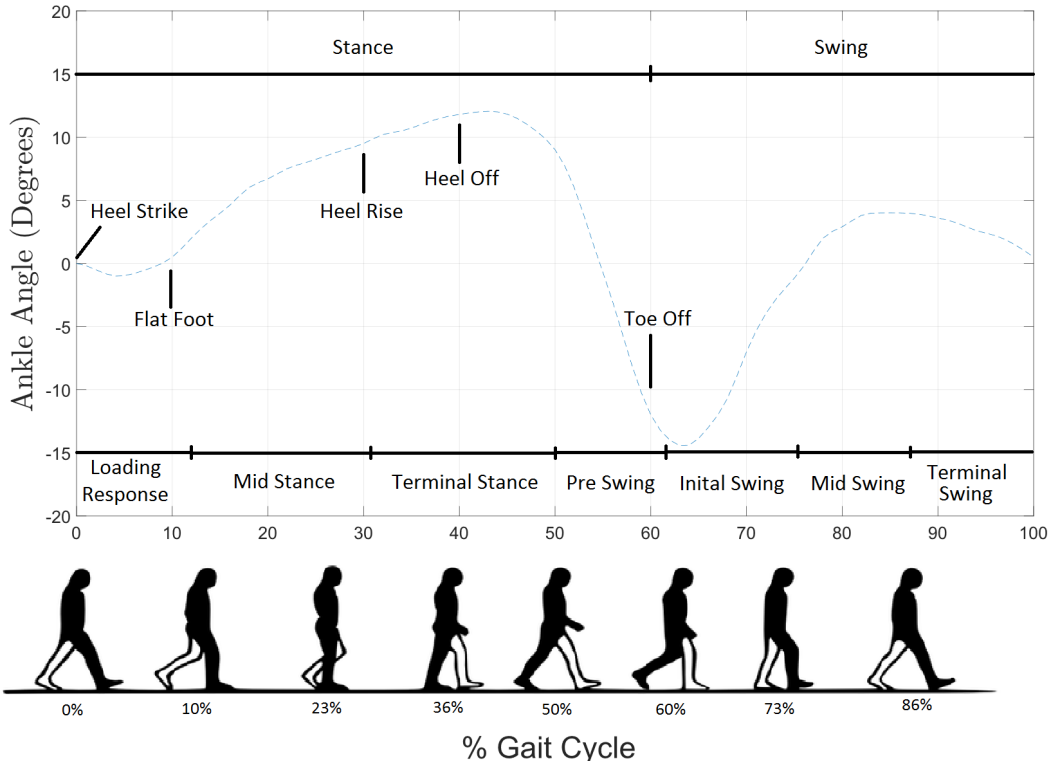

Figure 2.4: Standardised gait cycle, with gait events/phases labelled.

2.2.2 Abnormal Gait due to Drop-Foot

Drop-foot affects gait in several ways. Figure 2.5 and the subfigures therein illustrate the changes to the gait cycle: (A) shows the 'heel off' at the start of the cycle. Weakness in the anterior tibialis means force cannot be applied through the leg and into the floor during 'toe-off', causing the individual to shift weight to the other foot to provide clearance, commonly resulting in lateral movement of their centre of weight. This is often accomplished by the upper body shifting to the healthy side, as seen in (B). As the angle of the foot is no longer controllable, the foot hangs down due to gravity. This forces an extended lift around the knee joint and a high knee movement, as shown in (C). This increase in knee flexion causes a stair-like-climbing movement. The typical 'heel strike' that ends the swing phase is replaced with either a slapping motion against the ground or the entire foot being planted on the ground, as seen in (D). In severe cases, the subject may not have the ability to support their weight due to the weakness in the affected foot. A walker or cane will often be used to assist in this respect.

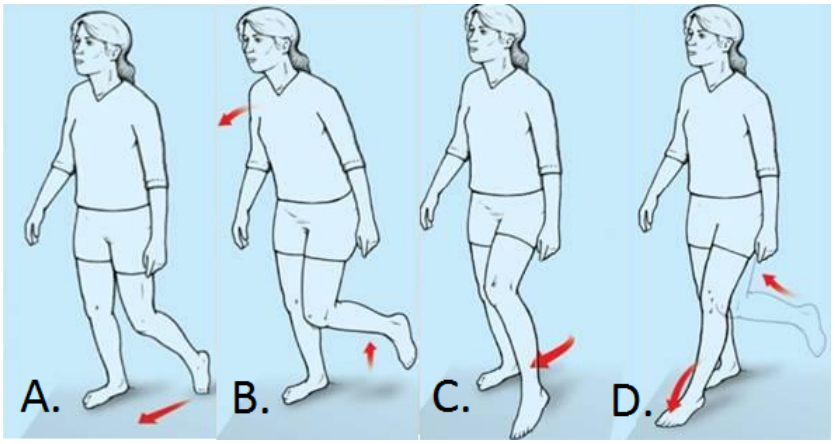

Figure 2.5: Drop-foot walking cycle. Source FootCare (2018).

2.3 Current Technologies for Drop-Foot

The range of current Assistive Technologies (ATs) to alleviate drop-foot can be broken down and categorised as: mechanical/electromechanical, functional electrical stimulation (FES), hybrids and soft robotics. The most often cited quantitative measurements to evaluate the effectiveness of assistive devices include; increased speed, reduction of effort and decreased feelings of anxiety and depression.

2.3.1 Electro-Mechanical

The most commonly prescribed interventions comprise mechanical ankle orthoses. These passive mechanical AT systems span a wide range of devices to limit the impact of drop-foot. Systems include splints, Ankle Foot Orthoses (AFO), knee and leg braces or even, most basically, walking frames and sticks. AFOs comprise a rigid or semi-rigid splint that fixes the ankle. These can rapidly and cheaply increase an individual's mobility. A substantial number of studies have evaluated the effect of AFOs on a range of medical conditions, including sub-acute or chronic stroke and MS (Pourhosseingholi et al., 2019; Moltedo et al., 2018; Momosaki et al., 2015; Tyson et al., 2013; Everaert et al., 2013). The prevalent assessment metrics are walking speed and energy efficiency. While there is little published evidence to support long term effectiveness, there is a strong consensus that they improve energy efficiency and gait during use (Khurana et al., 2013). However, these typically restrict motion and can discourage recovery, leading to increased spasticity and soft tissue shortening (Forghany et al., 2010). These flaws mean gait remains abnormal and may lead to a negative impact on dignity. These limitations are exacerbated by 60% of AFO users being fitted with inadequate orthoses (Kluding et al., 2013). For these reasons, clinicians are often unwilling to prescribe AFO devices, as reflected by studies in which 47% of people have never

used them (Esnouf et al., 2010). Even when used, rejection rates of 30% are typical, with an adverse effect upon dignity cited as a primary limitation (Esnouf et al., 2010). Advanced passive systems, conceived around superelastic elements, have focused on further reducing energy exertion via stiffness control and absorbing and re-releasing energy during the gait cycle (Mataee and Andani, 2014). Two concepts have been proposed to allow the stiffness to be set, (1) multi-axis elements, rotational and linear, loading conditions, and (2) an element designed as a hinge, with acting length varied by linear displacement. Both concepts show, via numerical simulations, good correlation with desired ankle stiffness for different walking speeds: (1) slow 78%, normal 85%, fast 87%, (2) slow 62%, normal 88%, fast 82%. By utilising pseudoelasticity, energy stored in the superelastic element is hypothesised to allow control of dorsiflexion. However, these concepts are yet to be built, implemented or tested clinically. Actively controlled mechanical systems have been developed and employ pneumatics, hydraulics and motor systems. Examples include fluid brake intelligent AFOs (Kikuchi et al., 2010), linear motor active AFOs (Hwang et al., 2006) and exoskeletons (Dollar and Herr, 2008). Exoskeletons have been shown to reduce torque on the hip by 62%. The most advanced research uses Quasi-Passive approaches within the exoskeleton, (Shamaei et al., 2014), pictured in Figure 2.6. Here a spring of desired stiffness is placed in parallel with the knee joint, engaging via an electromechanical clutch only during the weight acceptance phase ($0 - 12\%$). Experiments involving humans were conducted, and preliminary findings found the knee joint produces significant motor adaptation to retain reasonably invariant kinematic and kinetic movements. It was also found that the system provided substantial assistance to knee movements, by reducing stress on weak muscles/assisting stability and offering power assistance through some of the motion. However, like all active systems in the field, general limitations include their large invasive size, cost and considerable power requirements.

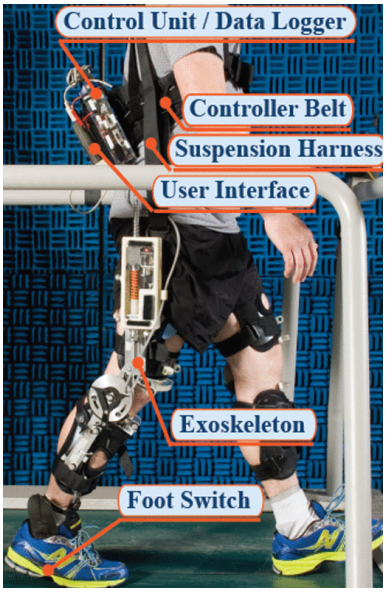

Figure 2.6: The quasi passive knee system from Shamaei et al. (2014)

2.3.2 Functional Electrical Stimulation

When 290 healthcare professionals and 120 patients and carers were asked what assistive devices they most commonly used 34% and 47% respectively quoted Functional Electrical Stimulation, making it the most frequently used device within the study (Hughes et al., 2014). FES operates by applying electrical pulses to the nerves supplying the user's muscles to generate useful movement that would otherwise be unavailable due

to nerve damage. FES was first proposed for drop-foot by Liberson in 1961 (Liberson et al., 1961) and is now recommended by the National Institute for Health and Clinical Excellence (NICE) (NICE, 2009). FES systems for drop-foot typically have a single pair of surface electrodes, an example being the Bioness L300, which is shown in Figure 2.7. Multi-channel systems are also available, such as the Odstock 4-channel and 2-channel stimulators. Here, further channels commonly stimulate hamstrings or gluteal muscles to address knee flexion, or hip stability, respectively. Implanted systems have been commonly available since 2006 with the introduction of the STIMuSTEP, a 2 channel device, and more recently, partially implanted systems such as Ottobock ActiGait. In all cases, preset stimulation profiles are triggered either via a pressure sensor in the shoe or via a tilt sensor mounted on the device.

Figure 2.7: L300 FES stimulator by Bioness.

Clinical evidence demonstrates that FES has significant advantages compared to passive orthoses (Prenton et al., 2017; Veerbeek et al., 2014). These advantages include promoting more natural walking, having a smaller size and reducing the number of falls by 72% (Esnouf et al., 2010; Barrett and Taylor, 2010; Mann et al., 2005). Meta-analyses of thirty studies from 1990 to 2008 showed an increase in walking speed by 16%, a reduction in effort of 29%, as well as reduced spasticity, anxiety and depression (Roche et al., 2009; Barrett and Taylor, 2010). Further meta-analyses, including nineteen studies recruiting 490 people with MS, revealed a significant initial orthotic effect, with a mean increase in gait speed of 0.05m/s (Miller et al., 2017). Additional studies show electrical stimulation provides long term recovery benefits (Rushton, 2003), assisting sit to stand due to having no restriction and greater clearance due to improved knee/hip flexion.

Despite positive effects, several limitations of FES are also present. Perhaps foremost is the time it takes to setup (Micera et al., 2010). Typically systems take between 10 and 15 minutes to don, even after training (Taylor et al., 1999; Dutta et al., 2012). Additionally, battery limitations and fatigue limit the length of a session (Micera et al., 2010; Stirling et al., 2011). Unfortunately, FES is unsuitable for lower motor neurone conditions, or in cases of severe muscle deterioration. Some users feel burning/prickly sensations which vary in intensity depending upon the quality of contact (Dutta et al., 2012). Electrode

pads also need replacing over time (Karu et al., 1995). Although a less prevalent system, implanted devices remove the need to position electrodes, regularly replace electrodes, and significantly reduce or eliminate sensations associated with external stimulation (Buentjen et al., 2019). However, they require surgery to implant.

2.3.3 Electrode Arrays for FES

An alternative solution to using large pads or implants is to use multiple electrodes arranged tightly to form an array. Electrode arrays embed several electrode pads in a predefined layout, that can be individually activated. There are two types of layout: the first has pads which are shaped to correspond to muscle positions, e.g. HandNMES (Snoek et al., 2000) and H200 Bioness. However, a mismatch between the muscle and pads can limit effectiveness (Crema et al., 2018) or require a bespoke system for every user. The second employs a grid layout which allows a broader application to different limbs and users, e.g. INTFES (Velik et al., 2011) and ShefStim (Kenney et al., 2016). However, an identification method is required to locate an appropriate electrode pad.

Existing pad identification methods (e.g. Schill et al. (2009); O'Dwyer et al. (2006); Micera et al. (2010); Popović-Bijeli et al. (2005)) share a common approach which replicates manual trial and error pad placement. Each pad is activated in turn, and the resulting movement is recorded. The pad which produces the best movement (e.g. greatest dorsiflexion, least roll) is selected. Minor variations exist, including activating pairs or groups of pads, in turn, (Schill et al., 2009) and exchanging cathode and anode positions (O'Dwyer et al., 2006). The most clinically studied approach is ShefStim. ShefStim employes 64 electrode pads and uses multiple active pads to form a "virtual electrode" (Prenton et al., 2014; Kenney et al., 2016). A "virtual electrode", comprises of 4 electrodes, in a 2x2 configuration. The input position is identified by shifting the virtual electrode along the array in the same way the single electrode system operated. A participant perception survey, involving 10 individuals, ranging from 26 to 79 years old, used ShefStim unsupervised for 2 weeks following initial consultations (Prenton et al., 2014). This found that the setup time took over 14 minutes on average, longer than their own FES devices. When participants were asked to score their own 2 channel FES devices against ShefStim, even with the easier pad placement, the long setup time resulted in the two systems receiving the same score on average.

Most arrays, like ShefStim, use conventional polycarbonate electrode pads (Neuman, 2000) which are not breathable or comfortable and have to be regularly replaced. Unfortunately, very few fabrication techniques have been developed that can fully realise a wearable electrode array. This is due to a lack of breathability, flexibility and issues with washability. Embroidery has been investigated by Keller (2007) to manufacture fabric electrode arrays, but this required high-quality, expensive custom made silver sputter yarns. These could only be produced with plasma vapour sputtering since degradation

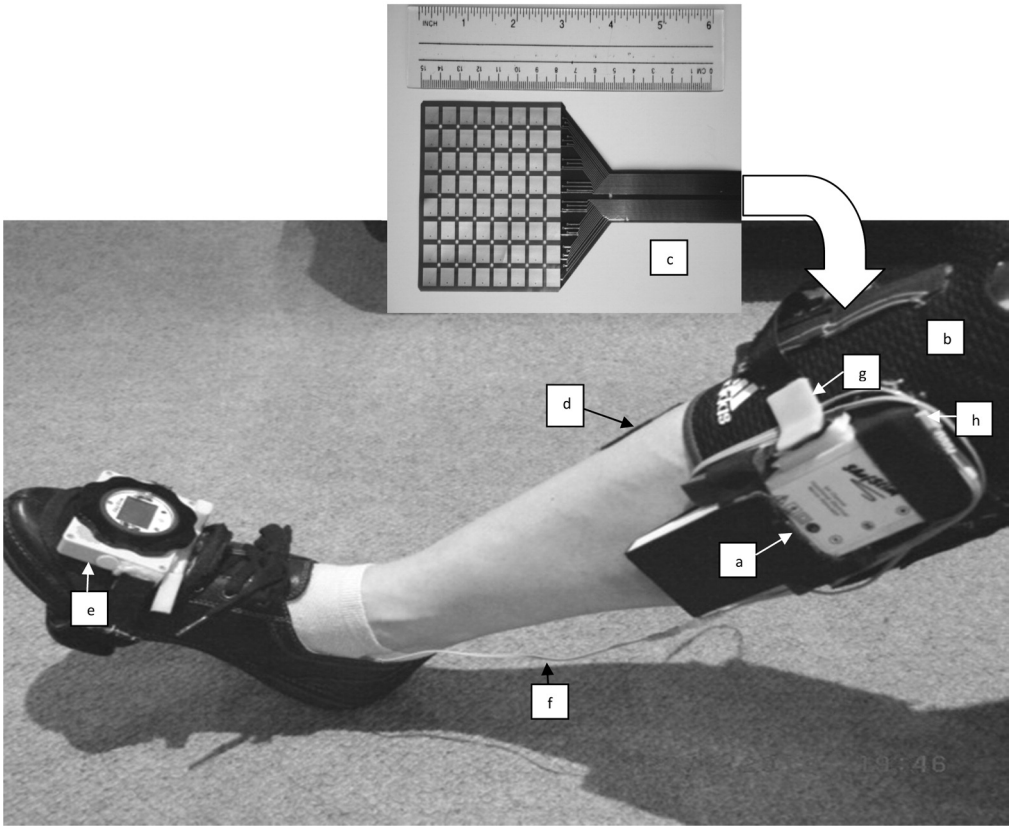

Figure 2.8: ShefStim system (medial view of leg during automated setup). The parts are; a) ShefStim stimulator; b) modified knee sleeve; c) flexible printed circuit board array of 64 electrodes (cathode electrodes); d) conventional anode; e) foot sensor and remote control device housed in a bespoke foot-pod; f) conventional footswitch; g) electrical connector for the array; h) footswitch connector. Image from Prenton et al. (2014).

of the conductive properties occurs around the surface during the embroidery process (Marc, 2009). Similarly, weaving and knitting have been used to fabricate a wide range of wearable electronic applications including sensors, displays, health monitors and power generation. However, these approaches are not suitable for producing a wearable FES array, since they impose constraints on the layout of conductive paths. Additionally, there is a lack of homogeneity in the resistance through the fabric due to imprecise gaps between the conductive yarns, which is an inherent limitation of the fabrication approach.

To address the above limitations, Yang et al. (2014a) screen printed conductive pastes directly onto everyday fabrics to form dry electrodes. Results confirmed user tolerance, as well as increased repeatability of joint movement compared to the commercial standard which uses a traditional "wet" hydrogel interface. This technology is inexpensive to produce due to the wide availability of pastes and fabric. The full system consists of four printed functional layers and allows much more breathability than other methods due to the use of a cotton or polyester textile. The system has had clinical success

after it was able to produce clinically relevant reference postures in the upper body and electrotherapy pain relief (Freeman et al., 2016; Yang et al., 2014a, 2019a,b).

2.3.4 Hybrid Approaches

FES has been shown to overcome the primary limitation of electromechanical approaches (size, cost, and restricted movement). Yet it has its own significant drawbacks including; fatigue, skin irritation, long setup times and is unable to provide effective support to people with severe muscle wastage. These differing limitations are in proportion with the level of support provided by each method and hence might be alleviated by suitably combining FES and mechanical approaches. This is the philosophy behind hybrid strategies. The combination of FES and passive or active mechanical devices was first demonstrated in 1989 when FES was combined with self-fitting modular orthoses (SFMO) using motors and cables (Popovic et al., 1989). The principal benefits of this hybrid approach were reduced energy exertion of the patient compared to separate systems, a greater range of achievable positions and stances, and less muscle fatigue (though this was still present).

Despite this initial work, few further hybrid devices have been developed, and fewer still clinically evaluated. In Lane (2015) FES and elastomeric splinting were combined into a hybrid device, to alleviate difficulties with electrode positioning, specifically to aid children and young people. Results took during 3 concurrently timed 10m walks, using 1 subject with left-hemiplegia, indicated a hybrid combination provided the best solution. These results demonstrate the hybrid system had the longest stride (no intervention - 115cm, splint alone - 118cm, hybrid - 123cm), least cadence steps per min (no intervention - 124.47 steps/min, splint alone - 120.38 steps/min, hybrid - 118.59 steps/min), lowest physiological cost index (no intervention - 0.49, splint alone - 0.35, hybrid - 0.30) and a marginally higher walking speed (no intervention - 1.2 m/s, splint alone - 1.18 m/s, hybrid - 1.21 m/s).

Although research is sparse in the area of hybrid approaches for drop-foot, there have been demonstrations in similar fields linked to the lower limb. A treadmill based gait rehabilitation system in China combined FES and pneumatic actuation (Tu et al., 2016). The system produced full gait motion without any voluntary human motion by using pairs of pneumatic muscle actuators positioned either side of the hip and knee joints, providing flexion and elongation alongside an off-the-shelf multi-channel FES stimulator, Rehastim2. FES has also been combined with a Joint-Coupled Orthosis (JCO) (Farris et al., 2009). The aim was to restore gait to individuals with spinal cord injuries. The motion was achieved with a 2-channel FES stimulator which was subsequently controlled and limited by controllable friction brakes located at the knee and hips. Results indicate that, after 15 minutes, muscle output stabilised at 85% of its initial output, suggesting

continuous walking is possible without significantly degrading performance. However, both systems are large and must be worn over clothing, which limits user uptake.

The above hybrid approaches have mitigated the limitations of individual approaches. In particular, they have resulted in less irritation/fatigue, reduced FES power, improved energy efficiency and have formed systems suitable for more people (as hybrids can also assist balance). This suggests there is potential for further research into combined systems. However, mechanical components of the devices are inherently limited by being either fixed (no degrees of freedom) or large, heavy and difficult to don/doff (due to actuators about each degree of freedom). These hard constraints can only be overcome by seeking a new approach. Therefore, the next section expands the review to cover the potential for soft robotic technologies. This field has only been applied to address drop-foot in a small number of instances.

2.3.5 Soft Robotic Technology for Medical Application

The soft robotic field covers a range of technologies including stacked dielectric elastomer actuators, electro-thermal actuation and soft pneumatic actuators. Their fluidity and compliance mean that soft robotics can potentially address the inherent limitations of existing electromechanical systems. In principle, they can replace large, cumbersome devices with a wearable technology that looks and feels like regular clothing.

The use of shape memory alloy (SMA) wires was investigated in (Stirling et al., 2011), where they exploited their contractual response to applied heat. The SMA wires were placed around the ankle to control motion. Those at the front control dorsiflexion, those at the back plantarflexion, and those at the sides lateral movement. The heat was generated electrically via control of electrical current across a known resistance. Although the overall size of the actuation system was small, the device was complex to put on and wear. Additionally, the actuation cycle time was too long to support a natural walking speed. To address this issue, the addition of a cooling system to shorten the cycle time would be required but was not investigated. Due to high power requirements, the device was unable to provide support throughout the day (battery life - 39 minutes, while the average time spent shopping is 41 minutes, excluding travel (Goodman, 2016)).

Four pneumatic artificial muscles were employed in a device which assisted ankle motion in Park et al. (2014). Artificial muscles contract, or elongate depending on air pressure, which was exploited to control ankle movement. An artificial muscle was responsible for each direction of motion, mimicking biological architecture. The device was very complicated, as can be seen in Figure 2.9, and took up more space than the SMA device, thereby limiting the clothing that could be worn. Furthermore, the device operated at 5.7 Bar, giving rise to safety concerns in the event of failure.

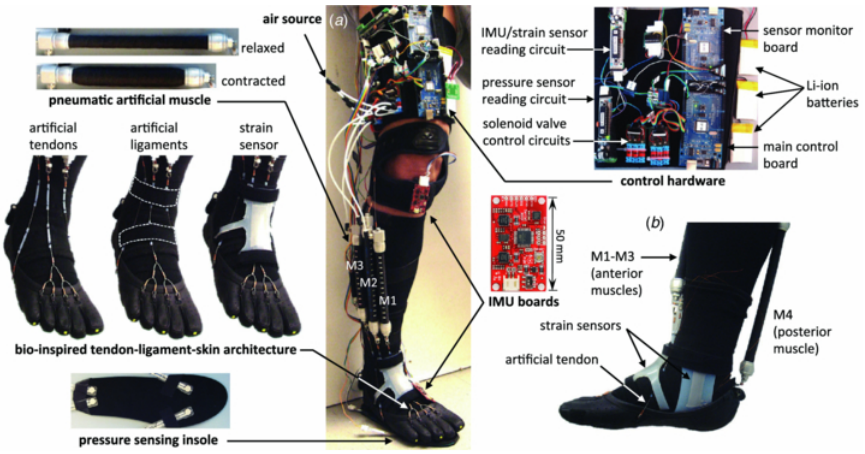

Figure 2.9: Pneumatic artifical muscle ankle assistance technology from Park et al. (2014)

While no other examples have been reported for drop-foot, other soft robotic approaches have been applied to the assistive technology domain. Dielectric elastomer actuators were developed in (Huaming et al., 2015). They achieved snake-like locomotion that behaved similarly to pneumatic muscles including, a rotation of 70-degrees and linear elongation of 8mm. However, current systems are bulky, limiting their wearability. Variable stiffness fibres (Chenal et al., 2014) have been developed to produce a prototype finger brace, only allowing motion when required by controlling the stiffness through heat. This enabled the implementation of a simple hold/release control scheme. However, the system effectiveness was limited by the time required to heat and cool the variable stiffness fibres.

2.4 Summary

A range of assistive technologies approaches have been considered, including mechanical structures, functional electrical stimulation devices and soft robotic systems. This review has highlighted the potential of soft robotic approaches but also the significant limitations and safety concerns.

On the other hand, FES is a prevalent assistive and has a positive effect on activity post-stroke, promoting muscle use and reducing the probability of falls. However, FES devices have several limitations: they do not mimic natural gait movement, electrode pads are challenging/time-consuming to put on, and fatigue can shorten the period of use.

Although there is potential in combining FES with mechanical or soft robotic systems, the primary research need is to address the limitations of FES. This is not only needed to improve the experience of FES users, but to also ensure FES can provide the primary source of actuation in any future hybrid assistive devices. To examine the limitations of

FES in more detail, the next chapter provides additional information about FES, motor function and existing FES controllers.

Chapter 3

Physiology and FES Characteristics

The previous chapter established the potential of FES to address drop-foot, but it also showed limitations in current technology. To explore this in more detail, the chapter begins by defining the physiological principles governing muscle contraction. Specifically, the differences between natural and artificially-evoked muscle activation are detailed. This chapter also sheds light on the challenge of developing a suitable FES control strategy by critically evaluating current FES control strategies for drop-foot.

The physiological principles described during this chapter appear in many medical textbooks. The sources used here include, but are not limited to, Kelso (1982); Wederich et al. (2000); Bullock and Wang (2001); Levine (2012) and Knotkova (2019).

3.1 Physiology - Motor Control and the Lower Limb

Human movement is performed in a complex hierarchical structure containing distinct layers. The Central Nervous System (CNS) consists of the brain and spinal cord and is responsible for the integration, processing and response to sensory information. The rest of the nervous system is known as the Peripheral Nervous System (PSN), of which the peripheral nerve is the main component. Electrical signals, which control voluntary motion, are transmitted through nerves using electrochemical impulses called action potentials.

3.1.1 Action Potentials

Nerves are formed by groups of connected neurons, as shown in Figure 3.1. Each neuron has a long segmented cell body, 'axon', allowing electrical signals (action potentials) to propagate. Action potentials are the control input for muscular tissue. They are generated in the initial segment of the neuron when a stimulus (electrical or chemical) alters the state of the local ion channels. There are two main events, the resting period and the action potential.

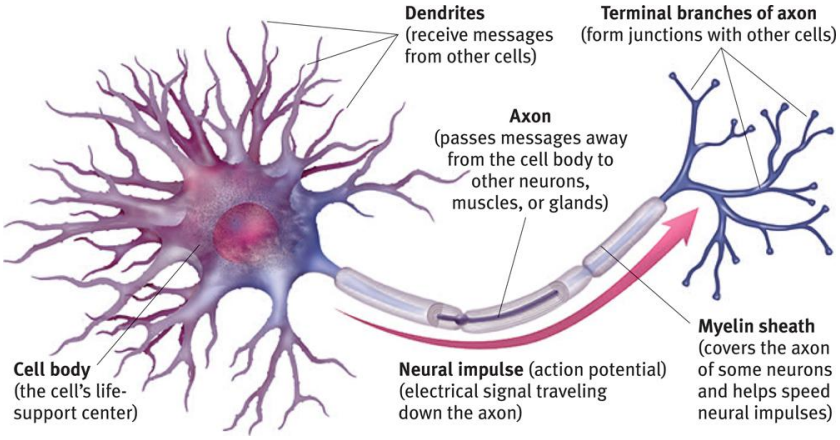

Figure 3.1: Labelled diagram of a typical neuron. Source HumanBodyforEducation (2018).

Chemical gradients across the axon membrane result in a negative resting potential (-70 mV). This is because the membrane permeability for the potassium ions is much higher, allowing the ions to diffuse out of the cell down its electrochemical gradient. Because of this enhanced permeability, the potassium is close to an electrochemical equilibrium. The membrane potential is, therefore, close to the equilibrium potential of -90 mV. The resting potential varies from this because the of the presence of sodium ions, however, they are not at electrochemical equilibrium (due to the lack of active leak channels) thus have a small effect on the resting potential. The slight negative resting-state means the segment is able to quickly become positive under excitation, specifically the low levels of sodium during rest allows for a large amount of sodium to rush in through the activated leak channels which propagate the ATP.

An action potential is propagated along the axon by voltage-activated channels located in the axon membrane. A sodium channel activates at a stimulus of -55mV allowing a large amount of sodium to rush into the axon segment, causing depolarisation (a spike in positive potential charge). This charge spreads, depolarising the next segment of the axon. At 30mV potassium channels activate, re-polarising the segment. Another action potential is only possible after the resting potential is re-established; this is called the refractory period. The action potential continues along the axon, transmitting between neurons by terminal branches (synapses) until it reaches its destination. A specialised synapse connects neurons to muscle tissue.

3.1.2 Muscular Tissue

Three types of muscles have been officially identified in humans with quite different traits. Of these, the skeletal muscles are responsible for controlling the movement of human skeletons. Skeletal muscles are attached to bones by tendons and consist predominantly of active contractile tissue which shortens when stimulated.

Skeletal Muscles are split into 2 different types. Slow-twitch fibres, Type I, use aerobic cellular respiration for Adenosine Triphosphate (ATP) production providing better resistance to fatigue compared to the other skeletal types. The second is fast-twitch fibres (Type II). These use anaerobic glycolysis for ATP production. However, this approach cannot be maintained for long periods, resulting in a faster rate of fatigue in exchange for stronger contractions.

Voluntary muscle contraction recruits the smaller, more fatigue-resistant Type I muscles fibres first, and Type II when a greater force is required. Muscle recruitment is achieved by exciting motor neurons asynchronously between 20 - 25 Hz. At these frequencies, each impulse within the neuron can expire before the stimulus for the next action potential is applied. The result of an action potential is a brief contraction, "twitch", of the motor units it is connected too. Repeated excitation before a twitch fully relaxes (i.e. within 200 ms), leads to the summation of the contractile forces such that a smooth, tetanic, step like muscle contraction is produced. However, it is important to note that there are dynamic delays of approximately $0.2s$ between activating an action potential and achieving a contraction.

3.2 Functional Electrical Stimulation of Excitable Tissue

FES also utilises action potentials to generate movement but has several key differences in how they are activated. FES produces a disturbance to the electrical field surrounding nerve cells, inducing action potentials. This is done using two electrodes, one anode '+' and the other a cathode '-'. When current passes between the poles, positive ions (potassium) are repelled from the tissue close to the anode and are driven by Lorentz force (the electromagnetic force on a point charge) towards the cathode. When the potential difference between the two sides of the nerve reaches the critical threshold for excitation, an action potential will be elicited in the same way as previously discussed. However, action potentials produced by FES have impulses which propagate in both directions. Towards the muscles and the CNS. The impulse towards the muscles causes contractions while the pulse up to the CNS is credited with improving the brain's ability to relearn movement, an effect called the Hebbian theory phenomenon. The Hebbian theory proposes an explanation to how neurons adapt ("synaptic plasticity") in the brain during learning: If point 'A' is attempting to stimulate point 'B', artificial stimulation applied

to 'B' can help rebuild neurological connections between the two points (Young, 2015). This theory forms an important part of the motivation for using precisely controlled FES to assist movement during rehabilitation.

The level of motor neuron excitation is directly influenced by several parameters that can fluctuate from day to day and from person to person. The impedance of surrounding tissue affects the path of the electrical current, as current follows the path of least impedance. Although only a small electrical disturbance is needed to produce an action potential, the high impedance of skin and fat means that a high voltage is required. Typically the stimulation is current-controlled, in which case the size of the electrode pad constituting each pole needs to be considered as it has an inverse relationship with current density (Keller and Kuhn, 2008; Forrester and Petrofsky, 2004). This results in smaller pads being better able to stimulate deeper neurones. Additionally, the closer the anode and cathode electrodes are together; the more current will pass through surface tissue, resulting in less excitation in deeper tissue.

3.2.1 Stimulation Characteristics

FES artificially produces the pulses required to generate action potentials. Typically, muscles are activated using a Pulse Width Modulated (PWM) signal with fixed parameters (commonly amplitude and frequency). This is because the frequency and amplitude of pulses can be easily found to achieve a smooth, comfortable contraction for each participant. However, because Type II muscle fibres lie closer to the surface of the skin and are often larger in diameter, they are recruited first when FES is applied. These fibres have a lower resistance to fatigue. Furthermore, FES recruits the nerves in a continuous synchronous fashion, rather than asynchronously and typically at a higher frequency than natural recruitment. This further compounds the fatiguing effect of FES. Therefore it is crucial to use the lowest levels of stimulation possible. Also, because of this, directly varying amplitude levels increases rates of fatigue (Kesar et al., 2008) as some fibres are over-excited.

There are two types of PWM signals used clinically for the excitation of nerves: monophasic and biphasic. Monophasic waveforms consist of a repeating unidirectional pulse. This only allows the flow of ions in one direction. Alternatively, biphasic waveforms have a second negative pulse which allows ions to flow back. This produces a zero net current flow, reducing electrochemical irritation from any electrically induced Ph imbalances. Both stimulation pulse types have the same three parameters: pulse frequency, amplitude and duration, as illustrated in Figure 3.2.

Pulse frequency is the number of pulses per second. If the frequency is too low, the response will be a set of noticeable twitches. Commercial stimulators use a frequency between $25 - 50Hz$ (Wederich et al., 2000). Increasing the frequency can produce a

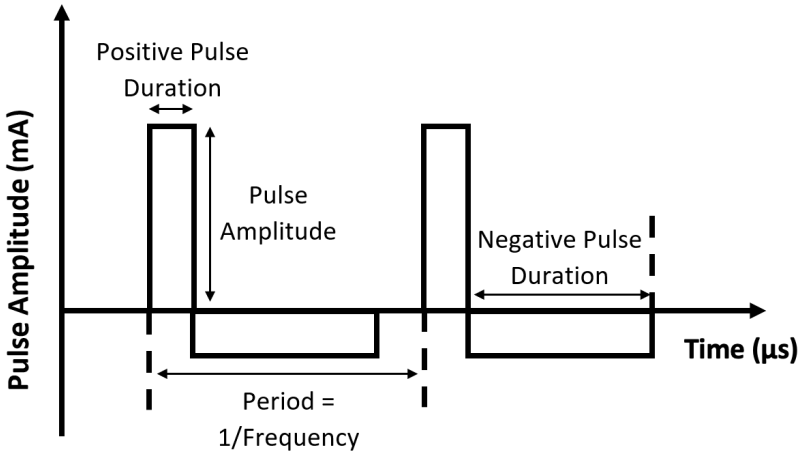

Figure 3.2: The three main parameters of FES PWM signals.

stronger contraction. However, this also increases the rate of fatigue. Due to this, frequency is not normally used for control. Instead, FES devices tend to adjust the strength of muscle contraction by altering the pulse duration.

Low amplitude stimulation is unable to generate muscle force because the threshold excitation needs to be exceeded (dead-zone). By increasing the amplitude or duration of stimulation, nerves will have the stimulus required to produce action potentials. This increases the muscle contraction strength (active region) until all nerves are activated, and the saturation region is entered. The non-linear isometric recruitment response to stimulation is pictured in Figure 3.3.A. Typically, the max current used is 30mA. Figure 3.3.B shows the typical operational band for current amplitude and pulse duration. Usually, commercial devices vary the pulse duration between $200 - 400\mu s$. This provides relatively comfortable experiences for patients and gives a suitable range to control muscle contractions (Wederich et al., 2000).

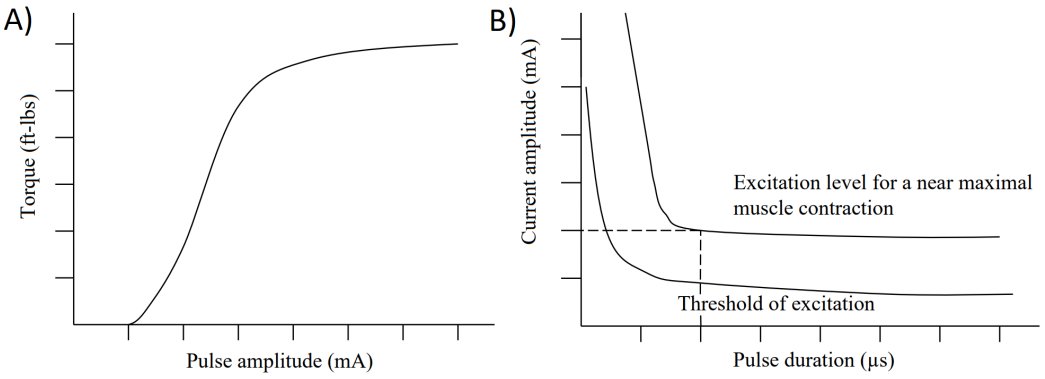

Figure 3.3: Left, muscle force against current amplitude. Right, relationship between pulse duration, current amplitue and stimulation responce. Both graphs are normalised for this manuscript to gain generic conclusions on general muscle relationships with FES. Source - Wederich et al. (2000)

3.3 Control of FES

A variety of commercial FES systems for drop-foot exist, but all employ open-loop control which is usually triggered by a pressure sensor mounted in the heel. This generates effective, but crude, dorsiflexion around the ankle. In the research domain, a range of both open and closed-loop systems have been developed. The first approach to open-loop FES control required manual user input to initiate stimulation pulses (Kostov et al., 1994). Here manual user commands were compared with "hand-crafted" rules. The latter was found to improve walking speed by 7% and reduce the stimulation duration by 38%.

Ferrarin et al. (2001) designed a model-based closed-loop proportional-integral-differential controller (PID) to control the angle of the knee and compared it to a model-based open-loop control and a PID feedback controller. The model was validated by stimulating the quadriceps with a triangular pulse. A comparison between the predicted and experimental results show 14% error for subject 1 and 17% error for subject 2. The study found the PID demonstrated better tracking properties than the open-loop model-based control (angular Root Mean Squared Error (RMSE) open $= 8.2° \pm 2.3°$, feedback $= 4.6° \pm 0.7°$), but this led to a considerable increase in time lag (Time-lag RMSE open 0.13 ± 0.05s, PID 0.24 ± 0.08s). Finally combining the two approaches, reduced the RMSE and time lag, but not below open-loop control (angular RMSE $3.4° \pm 0.3°$, Time-lag RMSE 0.21 ± 0.02s). However, no evidence was provided regarding the controller's robustness to fatigue.

Fuzzy logic and PID controllers have been combined with neural networks in (Chen et al., 2004). Three hemiplegic participants lay on a bed with their ankle elevated. The controller then attempted to track a reference stretched over 13 seconds, consisting of 500 points. The neural network achieved an angular RMSE of $8.11°, 7.81°$ and $5.59°$. The neural network combined with PID performed better, achieving an angular RMSE of $5.57°, 4.83°$ and $5.05°$, but a neural network combined with fuzzy logic performed best with $4.07°, 3.75°$ and $4.19°$. However, the stretched reference/high sampling rate limits the experimental validation.

An adaptive approach based on sliding mode control and non-linear compensation controlled the agonist-antagonist muscles to generate ankle movement (Kobravi and Erfanian, 2009). The study included experimental validation on 3 healthy and 3 paraplegic subjects. The experiment was conducted on a bench, with a hip angle of 90°, knee angle 0°, and the ankle free to move. The references tracked, however, were not natural gait. Instead, a biphasic trapezoidal ($20s$), biphasic raised-cosine ($12s$) and sinewave ($20s$) were used limiting the experimental validation. The mean RMSE for healthy patients was $3.2° \pm 1.2°$ and for paraplegic subjects was $3.4° \pm 0.2°$.

Li et al. (2011) put forward a threshold control approach, which assumes the voluntary movements are produced by shifting the length of appropriate muscles. A clear advantage of this approach is that there is no need to compute the muscle torques required to move the limb across a trajectory. Instead, joint angular acceleration was introduced to calculate the necessary muscle lengths. The satisfactory robustness and error tracking were confirmed in simulations. However, this approach is significantly limited, as time-varying non-linear muscle dynamics have not been considered, and no experimental data has been provided.

For multiple degrees of freedom, centralised control approaches can quickly become very complex. Decentralised modular control can help reduce complexity. A decentralised, modular control framework utilising fuzzy terminal sliding control and fuzzy logic control in each module is reported in (Nekoukar and Erfanian, 2012). The module control adjusts the pulse-amplitude and pulse-width of the applied stimulation. Three paraplegic subjects (T7, T12, T8-T9) took part in experimental tests, looking at the tracking error of the ankle, knee and hip. The experiments were repeated seven times. The average RMSE for the knee tracking task was $2.7°, 2.6°$ and $3.1°$ degrees. However, because of the limited data from the small study, the complexity of crafting suitable "if... then..." rules for the fuzzy logic and a large amount of sensory data required, the deploy-ability of the controller is limited.

Extremum-seeking was found to alleviate the need for initial system parameter identification by tuning the PID controller parameters during operation (Oliveira et al., 2016). However, only a simple high-low (trapezoidal) reference with a 35-second cycle was used. It is unclear how such an approach would deal with much shorter and more complex references, such as gait, which are much more heavily affected by time-varying non-linearities.

The most advanced approaches reported for drop-foot used iterative learning control (ILC) (Negrd, 2009; Seel et al., 2016). ILC uses the idea of learning over repeated attempts at the same task (here each step of the gait cycle). It uses error data from previous attempts to correct the stimulation input and assumes the system properties reset between trials. Seel et al. (2016) employed 6 inertial sensors to provide the ankle angle. The controller activated as the heel was lifted, in a similar way to commercial systems. A study with 6 post-stroke patients validated the approach. Although no data values were explicitly reported, graphs indicate RMSE values in the range $2°$ to $6°$ were achieved within 2 cycles and maintained. However, the first cycle was a model-based approximation of the required input. Although effective, the piecewise application of ILC (which explicitly considers each attempt to be entirely separate from all others) introduces discontinuities in the input signals and the resulting motion, which damages performance. Additionally, the use of ILC requires significant sensor data and an accurate system model.

3.4 Summary

This chapter has introduced the natural mechanisms used by the human body, and FES, to recruit muscle fibres. A review of control approaches illustrated the importance of closed-loop control combined with a system model to address drop-foot. Learning has been found to improve performance further, taking advantage of the inherent cyclic nature of gait. Additionally, the use of a model has been found to be effective at reducing time-lag. However, the ILC method utilising these requires a large amount of data to be stored between tasks. Additionally, it considers each step as a distinct, separate task rather than a continually repeating process. These have degraded the controller's overall performance for this application.

Chapter 4

Repetitive Control Framework

The control review highlighted how model-based controllers are required to address gait successfully. This is due to open-loop and simple structure feedback controllers being unable to compensate for the stimulation dynamics, which are characterised by a significant time delay. The most recent advancements in FES drop-foot control used iterative learning control (Seel et al., 2016) since it takes advantage of learning over repeated attempts (termed 'trials'). However, its performance was limited by the resetting characteristics between trials and the need for large amounts of data.

This chapter introduces a different framework which also employs the idea of learning but crucially does not assume resetting and learns over continuous cycles rather than trials. The framework is called Repetitive Control (RC). RC has not previously been used for drop-foot, although it was previously employed for FES tremor suppression by Copur et al. (2017). Despite a similar use of learning, there is a clear separation between ILC and RC in both theoretical underpinning and application areas, although duality properties do connect the two control approaches (Pipeleers and Moore, 2014). First, the traditional RC framework is introduced, then a substantial generalisation is developed that reduces the data requirement and improves robustness.

4.1 Traditional Repetitive Control Formulation

First put forward by Inoue et al. (1981), repetitive control was designed to enable perfect tracking of periodic signals. RC is based on the internal model principle. The internal model principle states that a model of the reference or external disturbance must be included in the controller to ensure either perfect reference tracking or complete disturbance rejection of the stable feedback system (Francis and Wonham, 1976b,a). For example, to track a unit step with zero steady-state error, the controller must include a model of the unit step function. This explains why a proportional-integral-derivative

(PID) controller requires an integral term to perfectly track a unit step. Despite the popularity of RC in controlling industrial machinery and various other research applications (Ratcliffe et al., 2007; Kurniawan, 2013) in the biomedical domain, it has only previously been used for tremor-related FES rehabilitation (Copur et al., 2017). To describe the traditional RC set-up, the starting point is the plant description, described by operator P

The discrete plant, P, has state-space dynamics (A_P, B_P, C_P, D_P) defined by

$$P:\ u \mapsto y \quad \begin{cases} x_P(i+1) &= A_P x_P(i) + B_P u(i) \\ y(i) &= C_P x_P(i) + D_P u(i) \end{cases} \tag{4.1}$$

where the state matrix $A_P \in \mathbb{R}^{n_P \times n_P}$, the input matrix $B_P \in \mathbb{R}^{n_P \times m}$, the output matrix $C_P \in \mathbb{R}^{\vartheta \times n_P}$, the feed-through matrix $D_P \in \mathbb{R}^{\vartheta \times m}$, m is the number of inputs, ϑ is the number of outputs, n_p is the number of states (order), x_P is the state vector, $u(i)$ is the input and $y(i)$ is the output at sample $i \in N$. The initial state is $x_P(0) = x_0$. Here, without loss of generality, A_P, B_P, C_P and D_P are assumed minimal (i.e. they capture the system dynamics with the minimum number of states (Tangirala, 2018)). This means the plant is controllable and observable. In the present application the plant corresponds to the stimulated ankle, with u the stimulation level and y the ankle angle. The gait profile is captured by a reference r. In RC, the discrete signal r is defined as being N periodic, that is $r(i) = r(i+N)$ for a given $N \in \mathbb{N}$ and all i. The traditional repetitive control tracking problem is to ensure that the plant output asymptotically converges to the reference, that is

$$\lim_{k\to\infty} y(kN+i) = r(i), \quad i = 0, \cdots, N-1 \tag{4.2}$$

while the control input converges to a signal $\hat{u}$, i.e.

$$\lim_{k\to\infty} u(kN+i) = \hat{u}(i), \quad i = 0, \cdots, N-1 \tag{4.3}$$

Here the period number is, $k \in \mathbb{N}$.

Discrete control system design is usually undertaken with the familiar z operator. However, using the one-sample advance operator 'q' enables a more transparent derivation of signal relationships as it can be used without transforming the underlying signal space. The q operator is defined by $q(v(k)) = v(k+1)$ for any discrete signal v. The most common form of RC update algorithm is

$$u(i+N) = Q(q)(u(i) + L(q)e(i)), \qquad u(-i) = 0\ \forall\ i \in \mathbb{N}. \tag{4.4}$$

where $Q(q)$, $L(q)$ are filters and $e(i)$ is the tracking error defined by $e(i) = r(i) - y(i)$. Applying the q operator to the plant dynamics (4.1) gives the expression $y(i) = P(q)u(i)$ with $P(q) = C_P(Iq - A_P)^{-1}B_P + D_P$. Combining this with the common RC update

(4.4) results in the control system shown in Figure 4.1. There are a large number of RC design approaches for the filters Q and L, see Longman (2000) and Longman (2010) for details.

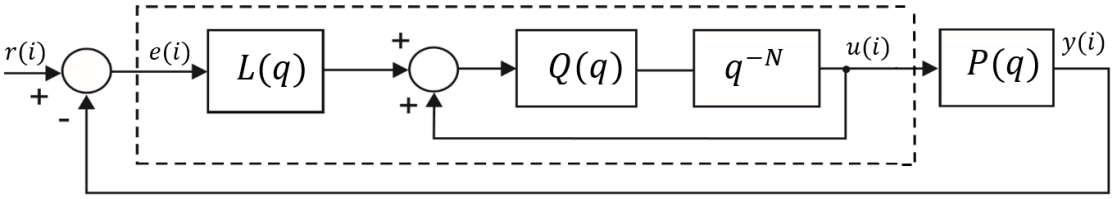

Figure 4.1: Traditional RC block diagram.

By combining all the blocks of the RC control loop shown in Figure 4.1, the closed-loop control dynamics can be written as

$$q^N(u(i)) = u(i+N) = Q(q)(1 - L(q)P(q))u(i) + Q(q)L(q)r(i) \tag{4.5}$$

and grouping the input term gives

$$u(i)(q^N - Q(q)(1 - L(q)P(q))) = Q(q)L(q)r(i). \tag{4.6}$$

By the internal model principle, the closed loop dynamics must be stable. A necessary and sufficient condition for stability is that the roots of the input-output control action relation

$$\frac{u(i)}{r(i)} = q^{-N}Q(q)L(q)\Big(1 - q^{-N}Q(q)(1 - P(q)L(q)\Big)^{-1} \tag{4.7}$$

are all inside the unit circle. This has the characteristic equation

$$1 - q^{-N}Q(q)(1 - P(q)L(q)) = 0. \tag{4.8}$$

It follows that a sufficient condition for stability is given by

$$\|Q(q)(1 - P(q)L(q))\|_\infty < 1, \tag{4.9}$$

or equivalently, in the frequency domain by

$$\sup_{\omega\in[0,\pi]} |Q(e^{jw})(1 - P(e^{jw})L(e^{jw}))| < 1. \tag{4.10}$$

Note, that although $Q(q)$ and $L(q)$ can be non-causal, the overall controller must be causal. This constrains the degree to which $Q(q)$ and $L(q)$ may be non-causal. Additionally, for an arbitrary reference r, the internal model principle requires $Q(q) = I$ in order to converge to zero norm error.

4.2 Lifted Repetitive Control Formulation

Selecting a suitable $L(q)$ to satisfy the sufficient stability conditions, (4.9) or (4.10), will solve the RC tracking objective, but requires access to all error data, as seen in update (4.4). To reduce the data required by RC, an approach will be adopted that has met with considerable success in the ILC field for rehabilitation. The idea is to apply 'point-to-point' tracking to repetitive control, which generalises the framework so that it tracks only a subset ($M < N$) of reference samples. By tracking a subset of isolated points in the reference, the RC design is no longer continuous (i.e. it is not possible to describe the system using transfer-functions). Therefore, the plant dynamics need to be represented in a way that means the repeating isolated points can be considered continuous. To achieve this, it is necessary to adopt the so-called 'lifted' framework, which was first defined rigorously in Pipeleers and Moore (2014); Bristow et al. (2006). Each sample of the 'lifted' system represents a whole period of the original unlifted system. At each sample of the lifted system, the inputs and outputs take the form of super-vectors. From these super-vectors, it is then easy to extract the subset of key points. For example, suppose we are interested in tracking only points $i = \{i_1, i_2 ... i_M\}$ in each period, with corresponding gait positions $r(i) = \{r(i_1), r(i_2) ... r(i_M)\}$. Then the traditional RC reference can be replaced by a vector containing only those points, as shown in Figure 4.2.

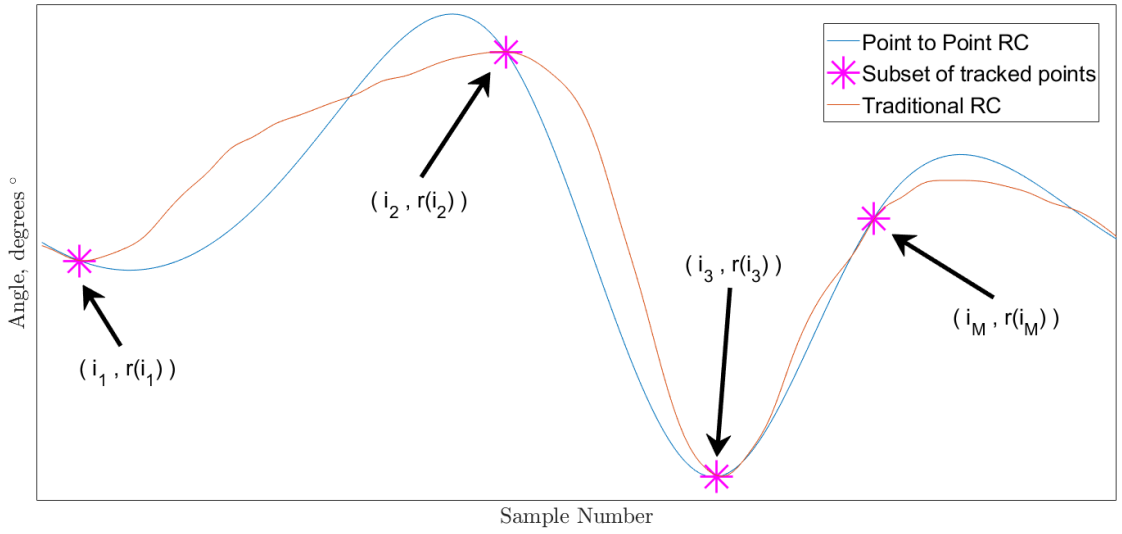

Figure 4.2: A single cycle comparing point-to-point and traditional repetitive control tracking. The x-axis shows the sample number within the cycle.

To extract the desired points, first, the input and output signals need to be redefined as super-vectors. These are respectively

$$\boldsymbol{u}(k) = [u(kN)^\top,\ u(kN+1)^\top, \cdots u((k+1)N-1)^\top]^\top \in \mathbb{R}^{mN}, \tag{4.11}$$

$$\boldsymbol{y}(k) = [y(kN)^\top,\ y(kN+1)^\top, \cdots y((k+1)N-1)^\top]^\top \in \mathbb{R}^{\vartheta N}, \tag{4.12}$$

where $k \in \mathbb{N}$ denotes the cycle number, similarly the reference and error are defined as

$$\boldsymbol{r}(k) = \boldsymbol{r} = [r(0),\ r(1), \cdots r(N-1)]^\top \in \mathbb{R}^{\vartheta N}, \tag{4.13}$$

$$\boldsymbol{e}(k) = \boldsymbol{r} - \boldsymbol{y}(k) \in \mathbb{R}^{oN}. \tag{4.14}$$

The original tracking requirement (4.2) can then be written equivalently as

$$\lim_{k\to\infty} \boldsymbol{y}(k) = \boldsymbol{r} \tag{4.15}$$

Using these signals, the RC update (4.4) can be written equivalently in its lifted form as

$$\boldsymbol{u}(k+1) = \boldsymbol{Q}(\boldsymbol{q})\big(\boldsymbol{u}(k) + \boldsymbol{L}(\boldsymbol{q})\boldsymbol{e}(k)\big) \tag{4.16}$$

where $\boldsymbol{Q}$ and $\boldsymbol{L}$ are lifted representations of the robustness and learning filters respectively.

The plant dynamics must also be expressed in lifted form. This is done by repeated application of the plant dynamics operator P (equation (4.1)). The state equation then becomes

$$x_P(i) = A_P^i x_0 + \sum_{j=0}^{i-1} A_P^{k-j-1} B_P u(j), \tag{4.17}$$

and output signal update (4.1)

$$y(i) = C_p A_P^i x_0 + \big(C_p\big(\sum_{j=0}^{i-1} A_P^{k-j-1} B_P\big) + D_P\big)u(j). \tag{4.18}$$

To redefine the state equation (4.18) and the output signal (4.17) as super-vectors, all cycles need to be stacked in the same way as the previous super-vectors (i.e. equation (4.12)). This gives the following lifted plant dynamics

$$\boldsymbol{P}: \begin{cases} \underbrace{x_P((k+1)N)}_{\boldsymbol{x}_P(k+1)} = \underbrace{A_P^N}_{\boldsymbol{A}_P}\underbrace{x_P(kN)}_{\boldsymbol{x}_P(k)} + \underbrace{[A_P^{N-1}B_P,\ A_P^{N-2}B_P, \cdots B_P]}_{\boldsymbol{B}_P}\boldsymbol{u}(k) \\ \boldsymbol{y}(k) = \underbrace{\begin{bmatrix} C_P \\ C_P A_P \\ \vdots \\ C_P A_P^{N-1} \end{bmatrix}}_{\boldsymbol{C}_P}\underbrace{x_P(kN)}_{\boldsymbol{x}_P(k)} + \underbrace{\begin{bmatrix} D_P & 0 & \cdots & 0 \\ C_P B_P & D_P & \ddots & \vdots \\ \vdots & \ddots & \ddots & 0 \\ C_P A_P^{N-2} B_P & \cdots & C_P B_P & D_P \end{bmatrix}}_{\boldsymbol{D}_P}\boldsymbol{u}(k) \end{cases}, \tag{4.19}$$

where the lifted discrete plant state-space dynamics now have the dimensions $\boldsymbol{A}_P \in \mathbb{R}^{n_P \times n_P}$, $\boldsymbol{B}_P \in \mathbb{R}^{n_P \times mN}$, $\boldsymbol{C}_P \in \mathbb{R}^{\vartheta N \times n_P}$ and $\boldsymbol{D}_P \in \mathbb{R}^{\vartheta N \times mN}$.

We can also define lifted forms of the filters $\boldsymbol{Q}(q)$ and $\boldsymbol{L}(q)$ as

$$\boldsymbol{Q}: \quad \begin{cases} \boldsymbol{x}_Q(k+1) &= \boldsymbol{A}_Q\boldsymbol{x}_Q(k) + \boldsymbol{B}_Q(\boldsymbol{v}+\boldsymbol{u})(k) \\ \boldsymbol{u}(k+1) &= \boldsymbol{C}_Q\boldsymbol{x}_Q(k) + \boldsymbol{D}_Q(\boldsymbol{v}+\boldsymbol{u})(k) \end{cases}, \tag{4.20}$$

where $\boldsymbol{A}_Q \in \mathbb{R}^{n_Q \times n_Q}$, $\boldsymbol{B}_Q \in \mathbb{R}^{n_Q \times mN}$, $\boldsymbol{C}_Q \in \mathbb{R}^{mN \times n_Q}$ and $\boldsymbol{D}_Q \in \mathbb{R}^{mN \times mN}$, and

$$\boldsymbol{L}: \quad \begin{cases} \boldsymbol{x}_L(k+1) &= \boldsymbol{A}_L\boldsymbol{x}_L(k) + \boldsymbol{B}_L\boldsymbol{e}(k) \\ \boldsymbol{v}(k) &= \boldsymbol{C}_L\boldsymbol{x}_L(k) + \boldsymbol{D}_L\boldsymbol{e}(k) \end{cases}, \tag{4.21}$$

where $\boldsymbol{A}_L \in \mathbb{R}^{n_L \times n_L}$, $\boldsymbol{B}_L \in \mathbb{R}^{n_L \times \vartheta N}$, $\boldsymbol{C}_L \in \mathbb{R}^{mN \times n_L}$ and $\boldsymbol{D}_L \in \mathbb{R}^{mN \times \vartheta N}$. More structured forms of (4.20) and (4.21) can be given if $Q(q)$ and $L(q)$ have explicit unlifted state-space forms. For example, when the unlifted filters Q and L take the typical form of a low pass filter, the lifted filters $\boldsymbol{Q}$ and $\boldsymbol{L}$ will have the same structure as the plant dynamics depicted in (4.19), as long as the filters are causal. The full lifted RC block diagram is given by Figure 4.3.

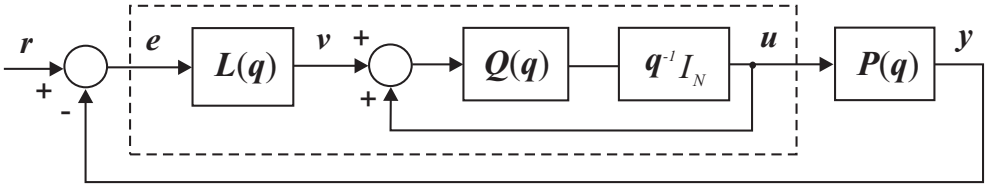

Figure 4.3: RC system lifted description.

Convergence condition (4.9) expressed for the lifted system corresponds to

$$\|\boldsymbol{Q}(\boldsymbol{q})(I - \boldsymbol{P}(\boldsymbol{q})\boldsymbol{L}(\boldsymbol{q}))\|_\infty < 1, \tag{4.22}$$

and it can be shown that the sufficient stability conditions (4.9) and (4.10) directly imply the lifted stability condition (4.22).

This is proven by applying the same derivation as in the unlifted case to ensure the closed-loop dynamics are stable, as seen in (4.9) and exploiting the dimensional freedom available in the lifted convergence analysis. See Pipeleers and Moore (2014).

In summary the lifted plant (4.19), controller (4.16), filters (4.21), (4.20) and condition (4.22) are simply their unlifted equivalents expressed as a high dimensional system where every sample of the lifted system (super-vector) is a whole period of the unlifted system. Similarly, the unlifted (time-domain) and lifted (cycle-domain) plant models are equivalent in the sense that they describe the same identical dynamics (yet in different domains) and feature the same system properties, see Pipeleers and Moore (2014) for further details.

4.3 Point-to-Point Repetitive Control

Having introduced the lifted framework, the following section generalises it to extract and track a reduced number of points. The starting point is to recall that the purpose of the point-to-point control is to extract and track a subset of $M < N$ points of reference r. This will be achieved by defining the indices

$$i = i_1, i_2, \cdots, i_M. \tag{4.23}$$

To express the task in the lifted framework, the indices need to be extracted from the supervector $\boldsymbol{r}$ by introducing a projection operator $\boldsymbol{\Phi} : \mathcal{L}^{mN} \to \mathcal{L}^{mM}$. For any lifted signal $\boldsymbol{s} \in \mathcal{L}^{mN}$, this operator is defined by

$$\boldsymbol{\Phi} : \mathcal{L}^{mN} \to \mathcal{L}^{mM} : \boldsymbol{s} \mapsto \boldsymbol{s}^{\Phi} : \boldsymbol{s}^{\Phi}(i) = \begin{bmatrix} s(iN + i_1) \\ s(iN + i_2) \\ \vdots \\ s(iN + i_M)) \end{bmatrix} = \boldsymbol{\Phi}_{j,i}\boldsymbol{s}(i), \tag{4.24}$$

where the $m \times N$ matrix

$$\bar{\boldsymbol{\Phi}}_{j,i} = \begin{cases} I, & \text{if} \quad i = i_j \\ 0, & \text{otherwise} \end{cases}. \tag{4.25}$$

The projection operator $\boldsymbol{\Phi}$ is therefore suitably defined to extract the values from the signal which correspond to the indices within i. The values of i_j that are not defined in i are rejected. In this case, the set of desired point-to-point output positions are extracted from the reference vector by

$$\boldsymbol{\Phi r} = \boldsymbol{r}^{\Phi} = \begin{bmatrix} r(i_1) \\ r(i_2) \\ \vdots \\ r(i_M) \end{bmatrix}. \tag{4.26}$$

We use this to replace $\boldsymbol{r}$ by $\boldsymbol{\Phi r} = \boldsymbol{r}^{\Phi}$ and $\boldsymbol{e}$ by $\boldsymbol{\Phi e} = \boldsymbol{e}^{\Phi}$ in the previous lifted framework. This means that $\boldsymbol{Q}(\boldsymbol{q})$ and $\boldsymbol{L}(\boldsymbol{q})$ must later be redesigned to be compatible for this lower dimensioned system.

The tracking objective (4.15) is replaced by

$$\lim_{k \to \infty} \boldsymbol{y}^{\Phi}(k) = \boldsymbol{r}^{\Phi}, \tag{4.27}$$

and the lifted form of the control input (4.3) must converge to a lifted signal, i.e.

$$\lim_{k \to \infty} \boldsymbol{u}(k) = \hat{\boldsymbol{u}}. \tag{4.28}$$

Substituting the redefined reference and error back into the RC update structure leads to the system shown in Figure 4.4.

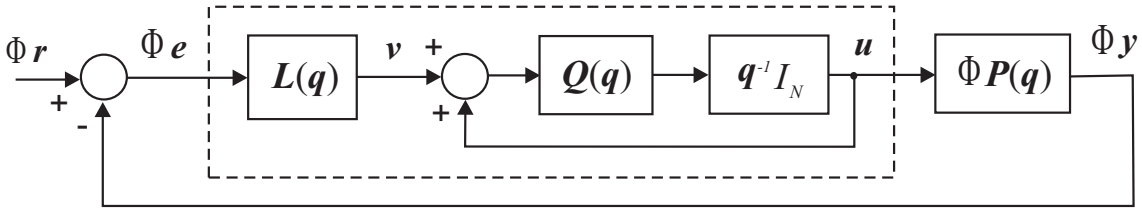

Figure 4.4: Point-to-point RC system lifted description.

A new form of the RC update and corresponding condition to solve the point-to-point problem can now be introduced.

Theorem 4.1. *The general lifted RC update*

$$\boldsymbol{u}(k+1) = \boldsymbol{Q}(q)(\boldsymbol{u}(k) + \boldsymbol{L}(\boldsymbol{q})\boldsymbol{e}^{\Phi}(k)) \tag{4.29}$$

where $\boldsymbol{e}^{\Phi}(k) = \boldsymbol{r}^{\Phi} - \boldsymbol{\Phi}\boldsymbol{y}(k)$*, and* $\boldsymbol{L}(\boldsymbol{q}) : \mathcal{L}^{mM} \to \mathcal{L}^{mN}$ *is selected to satisfy*

$$\|\boldsymbol{Q}(q)(I - \boldsymbol{\Phi}\boldsymbol{P}(\boldsymbol{q})\boldsymbol{L}(\boldsymbol{q}))\|_{\infty} < 1 \tag{4.30}$$

solves the point-to-point RC problem (4.27) and (4.28).

Proof. The lifted closed loop control dynamics are given by

$$\boldsymbol{u}(i) = \boldsymbol{Q}(q)\boldsymbol{L}(q)(\boldsymbol{I} - q^{-1}\boldsymbol{Q}(q)(I - \boldsymbol{\Phi}\boldsymbol{P}(q)\boldsymbol{L}(q))^{-1}\boldsymbol{r}(i) \tag{4.31}$$

and from the internal model principle, the convergence of the lifted tracking objective (4.27), and lifted control input (4.28) holds true if the poles of the lifted closed-loop control dynamics are all inside the unit circle. A sufficient condition for this is (4.30). □

The new point-to-point RC update (4.29) is similar to the traditional form (4.16), however now only the point-to-point error is needed and the operator $\boldsymbol{L}(q)$ must be completely redesigned. The selection of a suitable $\boldsymbol{L}(q)$ can be achieved by starting with an RC operator that satisfies the traditional unlifted problem as shown in the next theorem.

Theorem 4.2. *Let unlifted operator* $\bar{L}(q)$ *satisfy the traditional RC convergence criterion*

$$\|I - P(q)\bar{L}(q)\|_{\infty} < 1 \tag{4.32}$$

or equivalently

$$\sup_{\omega \in [0,\pi]} |I - P(e^{jw})\bar{L}(e^{jw})| < 1 \tag{4.33}$$

then the lifted operator

$$\boldsymbol{L}(\boldsymbol{q}) = \bar{\boldsymbol{L}}(\boldsymbol{q})\boldsymbol{\Phi}^* \tag{4.34}$$

satisfies condition (4.30) where $(\cdot)^*$ *denotes the adjoint operator.*

Proof. Inserting the lifted solution to the traditional RC problem (4.34) into the lifted RC update (4.30) gives

$$\|I - \boldsymbol{\Phi}\boldsymbol{P}(\boldsymbol{q})\bar{\boldsymbol{L}}(\boldsymbol{q})\boldsymbol{\Phi}^*\|_\infty = \|\boldsymbol{\Phi}\big(I - \boldsymbol{P}(\boldsymbol{q})\bar{\boldsymbol{L}}(\boldsymbol{q})\big)\boldsymbol{\Phi}^*\|_\infty \tag{4.35}$$

and since the unlifted (4.9) and lifted (4.33) stability conditions imply

$$\|I - \boldsymbol{P}(\boldsymbol{q})\bar{\boldsymbol{L}}(\boldsymbol{q})\|_\infty < 1 \tag{4.36}$$

we have the required relation

$$\|I - \boldsymbol{\Phi}\boldsymbol{P}(\boldsymbol{q})\bar{\boldsymbol{L}}(\boldsymbol{q})\boldsymbol{\Phi}^*\|_\infty \leq \|I - \boldsymbol{P}(\boldsymbol{q})\boldsymbol{L}(\boldsymbol{q})\|_\infty < 1. \tag{4.37}$$

□

This result means that any $L(q)$ operator used for traditional RC can be used to generate a suitable operator for a lifted point-to-point RC algorithm, $\boldsymbol{L}(q)$. An example of an RC update that can be used in Theorem 4.2 is the so-called gradient RC update, proposed in Hätönen et al. (2006, 2004). The gradient algorithm has a track record of experimental effectiveness, attractive robustness properties, and ease of implementation. These characteristics were illustrated in Copur et al. (2017) where gradient RC was used to control FES tremor suppression. It can be summarised as follows:

Lemma 4.3. *The gradient algorithm is defined by the unlifted RC operator*

$$\bar{L}(q) = \beta P^*(q) \tag{4.38}$$

where β *is a scalar chosen such that*

$$0 < \beta < \frac{2}{\sup_{\omega\in[0,\pi]} |P(e^{j\omega})|^2}. \tag{4.39}$$

The gradient algorithm satisfies the traditional RC convergence condition (4.32). Note that, to apply the controller experimentally, it is necessary that the plant satisfies the condition

$$C_P A_P^i B_P = 0 \quad \forall \quad i \geq N. \tag{4.40}$$

This ensures that the overal update ((4.4) with $L(q)$ *replaced by* $\bar{L}(q)$*) is causal.*

Proof. First, from the unlifted plant dynamics (4.19) the plant Finite Impulse Response (FIR) can be written as

$$h(i) = \begin{cases} h(0) &= D_p \\ h(i) &= C_p A^{i-1}{}_p B_p \end{cases}, \qquad i \geq 1. \tag{4.41}$$

The plant dynamics therefore has discrete time FIR filter form

$$P(q) : v \mapsto W, \qquad w(s) = \big(\big(\sum_{i=0}^{N} h(i)v(s-i)\big) + h(0)v(0)\big), \tag{4.42}$$

which can be seen to be causal. The plant adjoint operator is given in the state-space form by

$$\big(P(q)\big)^* : \; w \mapsto v \quad \begin{cases} x_P^*(s) &= A_P x_P^*(s+1) + C_P w(s+1) \\ v(s+1) &= B_P x_P^*(s+1) + D_P w(s+1) \end{cases} \qquad k \in \mathbb{N}. \tag{4.43}$$

By repeated application of the plant adjoint (4.43), and substitution of the finite impulse response (4.41), the noncausal discrete-time FIR form of $P(q)*$ is given by

$$(P(q))* : w \mapsto v, \qquad v(i) = \big(\big(\sum_{i=0}^{\infty} h(i)w(i+1)\big) + h(0)w(0)\big). \tag{4.44}$$

When $i \geq N$, knowledge of the next period is required, which is not available. To ensure this does not occur, the impulse response needs to be constrained by the condition (4.40). □

The point-to-point RC update comes from applying Table 4.1.

Point-to-Point RC Formulation
1: choose a β that staisfies Lemma 4.3
2: ensure the convergence condition, (4.30) is met
3: use Theorem 4.2 to give the required lifted filter $\boldsymbol{L}(q)$ (4.34)
4: then apply to Theorem 4.1, (4.29), to give the overall point-to-point RC update, which has the form 4.45

Table 4.1: Formulation of point-to-point RC.

The point-to-point RC has the form,

$$\begin{aligned} \boldsymbol{u}(k+1) &= \boldsymbol{u}(k) + \beta \boldsymbol{P}^*(\boldsymbol{q}) \boldsymbol{\Phi}^* \boldsymbol{e}^{\Phi}(k) \\ &= \boldsymbol{u}(k) + \beta \big(\boldsymbol{\Phi} \boldsymbol{P}(\boldsymbol{q})\big)^* \boldsymbol{e}^{\Phi}(k). \end{aligned} \tag{4.45}$$

However, implementation requires conversion of (4.45) back to its unlifted form. This is because the experimental implementation is in the time domain, which results in the

lifted controller becoming non-casual because data from the entire current full cycle, which does not exsist, would be required. However, by converting back to the unlifted form, only data prior to the sample being applied is required.

Note: All physical systems are proper (i.e. have more poles than zeros) and so $D_p = 0$. This will be assumed in the following derivations.

Proposition 4.4. *The lifted point-to-point update (4.45) has, for a single sample i, the following equivalent unlifted form*

$$\begin{aligned} u((k+1)N+i) =& u(kN+i) + \beta\Big(\sum_{j=1}^{\bar{i}} C_p A_p^{N-i+i_j} B_p e((k+1)N+i_j) \\ &+ \sum_{j=\bar{i}+1}^{M} C_p A_p^{i_j-i} B_p e(kN+i_j) \Big) \end{aligned} \tag{4.46}$$

where $\bar{i} = \max_j i_j \leq i$ is the most recent point-to-point sample index.

Proof. Consider the required structure of $\boldsymbol{v} = \big(\boldsymbol{\Phi P}(\boldsymbol{q})\big)^* \boldsymbol{w}$ in (4.45), i.e.

$$\big(\boldsymbol{\Phi P}(\boldsymbol{q})\big)^* : \quad \begin{cases} \boldsymbol{x}_P^*(k) &= \boldsymbol{A}_P^\top \boldsymbol{x}_P^*(k+1) + \boldsymbol{C}_P^\top \bar{\boldsymbol{\Phi}}^\top \boldsymbol{w}(k+1) \\ &= \boldsymbol{A}_P^\top \boldsymbol{x}_P^*(k+1) + (\bar{\boldsymbol{\Phi}} \boldsymbol{C}_P)^\top \boldsymbol{w}(k+1) \\ \boldsymbol{v}(k+1) &= \boldsymbol{B}_P^\top \boldsymbol{x}_P^*(k+1) + \boldsymbol{D}_P^\top \bar{\boldsymbol{\Phi}}^\top \boldsymbol{w}(k+1) \\ &= \boldsymbol{B}_P^\top \boldsymbol{x}_P^*(k+1) + (\bar{\boldsymbol{\Phi}} \boldsymbol{D}_P)^\top \boldsymbol{w}(k+1) \end{cases} \qquad k \in \mathbb{N} \tag{4.47}$$

Within this we have the lifted point-to-point structures

$$(\bar{\boldsymbol{\Phi}} \boldsymbol{C}_P)^\top = \begin{bmatrix} C_P A_P^{i_1} \\ C_P A_P^{i_2} \\ \vdots \\ C_P A_P^{i_M} \end{bmatrix}^\top, \text{ and} \tag{4.48}$$

$$(\bar{\boldsymbol{\Phi}} \boldsymbol{D}_P)^\top = \begin{bmatrix} C_P A_P^{i_1} B_P & \cdots & C_P B_P & 0 & \cdots & \cdots & 0 \\ \vdots & \cdots & \ddots & \ddots & & & \vdots \\ C_P A_P^{i_M} B_P & \cdots & \cdots & \cdots & C_P B_P & \underbrace{0 \quad \cdots \quad 0}_{N-i_M-1} & \end{bmatrix}^\top. \tag{4.49}$$

By repeated application of the lifted plant adjoint (4.47) and subsituting $\boldsymbol{w} = \boldsymbol{e}(k)$, $\boldsymbol{v} = \big(\boldsymbol{\Phi P}(\boldsymbol{q})\big)^* \boldsymbol{e}(k)$ is given by

$$\begin{aligned}
\boldsymbol{v}(k) &= (\bar{\boldsymbol{\Phi}}\boldsymbol{D}_P)^\top \bar{\boldsymbol{\Phi}}\boldsymbol{e}(k) + \boldsymbol{B}_P^\top \Big(\sum_{i=1}^{\infty} \big(\boldsymbol{A}_P^\top\big)^{i-1} (\bar{\boldsymbol{\Phi}}\boldsymbol{C}_P)^\top \bar{\boldsymbol{\Phi}}\boldsymbol{e}(k+i) \Big) \\
&= (\bar{\boldsymbol{\Phi}}\boldsymbol{D}_P)^\top \bar{\boldsymbol{\Phi}}\boldsymbol{e}(k) + \boldsymbol{B}_P^\top \Big(\sum_{i=1}^{\infty} \big(\boldsymbol{A}_P^\top\big)^{i-1} \boldsymbol{C}_P^\top \bar{\boldsymbol{\Phi}}^\top \bar{\boldsymbol{\Phi}}\boldsymbol{e}(k+i) \Big) \\
&= (\bar{\boldsymbol{\Phi}}\boldsymbol{D}_P)^\top \bar{\boldsymbol{\Phi}}\boldsymbol{e}(k) + \sum_{i=1}^{\infty} \Big\{ \Big(\boldsymbol{C}_P \big(\boldsymbol{A}_P\big)^{i-1} \boldsymbol{B}_P \Big)^\top \bar{\boldsymbol{\Phi}}^\top \bar{\boldsymbol{\Phi}}\boldsymbol{e}(k+i) \Big\}. \qquad (4.50)
\end{aligned}$$

The sufficient stability condition (4.40) to ensure the unlifted update is causal still holds, and it follows that for the lifted system, this requires

$$\boldsymbol{C}_P \boldsymbol{A}_P^i \boldsymbol{B}_P = \boldsymbol{0} \quad \forall \quad i \geq 1 \qquad (4.51)$$

The same proof for (4.40), which used the finite impulse responses of the unlifted system plant adjoint to show non-causal behaviour above a boundary condition, can be applied to prove this. Note, the constraint change on i is due to the transformation between the unlifted (time-domain) and the lifted (trial-domain) form. This constrains $\boldsymbol{v} = \big(\boldsymbol{\Phi P}(\boldsymbol{q})\big)^* \boldsymbol{e}(k)$ (4.50) to give

$$\boldsymbol{v}(k) = (\bar{\boldsymbol{\Phi}}\boldsymbol{D}_P)^\top \bar{\boldsymbol{\Phi}}\boldsymbol{e}(k) + \boldsymbol{B}_P^\top (\bar{\boldsymbol{\Phi}}\boldsymbol{C}_P)^\top \bar{\boldsymbol{\Phi}}\boldsymbol{e}(k+1). \qquad (4.52)$$

The unlifted state-space dynamics are given by

$$\boldsymbol{C}_P\boldsymbol{B}_P = \begin{bmatrix} C_P A_P^{N-1} B_P & C_P A_P^{N-2} B_P & \cdots & C_P B_P \\ \vdots & \ddots & & \vdots \\ \vdots & & \ddots & \vdots \\ C_P A_P^{2N-2} B_P & C_P A_P^{2N-3} B_P & \cdots & C_P A_P^{N-1} B_P \end{bmatrix},$$

and by applying the necessary stability condition for causality (4.40), ($\boldsymbol{C}_P \boldsymbol{A}_P^i \boldsymbol{B}_P = \boldsymbol{0} \quad \forall \quad i \geq 1$) the unlifted form has an upper triangular form

$$\boldsymbol{C}_P\boldsymbol{B}_P = \begin{bmatrix} C_P A_P^{N-1} B_P & C_P A_P^{N-2} B_P & \cdots & \cdots & C_P B_P \\ 0 & \ddots & & & \vdots \\ \vdots & \ddots & \ddots & & \vdots \\ \vdots & & \ddots & \ddots & \vdots \\ 0 & \cdots & \cdots & 0 & C_P A_P^{N-1} B_P \end{bmatrix}. \qquad (4.53)$$

It follows directly that

$$(\bar{\boldsymbol{\Phi}}\boldsymbol{C}_P\boldsymbol{B}_P)^\top = \begin{bmatrix} \overbrace{0 \cdots 0}^{i_1} & C_P A_P^{N-1} B_P & \cdots & \cdots & C_P A_P^{i_1} B_P \\ & \ddots & & \ddots & \vdots \\ \underbrace{0 \qquad \cdots \qquad \cdots \quad 0}_{i_M} & & C_P A_P^{N-1} B_P & \cdots & C_P A_P^{i_M} B_P \end{bmatrix}^\top . \tag{4.54}$$

Substituting the unlifted forms of the lifted state-space plant dynamics (4.48) and (4.54) into the point-to-point RC update (4.45) gives the unlifted point-to-point RC update

$$\begin{aligned} \boldsymbol{u}(k+1) = \boldsymbol{u}(k) + \beta \times & \begin{bmatrix} \begin{bmatrix} C_P A_P^{i_1} B_P & \cdots & C_P B_P & 0 & \cdots & \cdots & 0 \\ \vdots & & \ddots & \ddots & & & \vdots \\ C_P A_P^{i_M} B_P & \cdots & \cdots & \cdots & C_P B_P & \underbrace{0 \cdots 0}_{N-i_M-1} & \end{bmatrix}^\top \begin{bmatrix} \overbrace{0 \cdots 0}^{i_1} & C_P A_P^{N-1} B_P & \cdots & C_P A_P^{i_1} B_P \\ & \ddots & \ddots & \vdots \\ \underbrace{0 \qquad \cdots \quad 0}_{i_M} & C_P A_P^{N-1} B_P & \cdots & C_P A_P^{i_M} B_P \end{bmatrix}^\top \end{bmatrix} \\ & \times \begin{bmatrix} \underbrace{\begin{bmatrix} e(kN+i_1) \\ e(kN+i_2) \\ \vdots \\ e(kN+i_M) \end{bmatrix}}_{\bar{\boldsymbol{\Phi}}\boldsymbol{e}(k)} \\ \underbrace{\begin{bmatrix} e((k+1)N+i_1) \\ e((k+1)N+i_2) \\ \vdots \\ e((k+2)N+i_M) \end{bmatrix}}_{\bar{\boldsymbol{\Phi}}\boldsymbol{e}(k+1)} \end{bmatrix}, \end{aligned} \tag{4.55}$$

which simplifies to give the final matrix form

$$\boldsymbol{u}(k+1) = \boldsymbol{u}(k) + \beta \begin{bmatrix} C_P A_P^{i_1} B_P & \cdots & C_P A_P^{i_M} B_P & 0 & \cdots & 0 \\ \vdots & & \vdots & \vdots & & \vdots \\ C_P B_P & \ddots & \vdots & \vdots & & \vdots \\ 0 & \ddots & \vdots & C_P A_P^{N-1} B_P & & 0 \\ \vdots & & C_P B_P & \vdots & \ddots & 0 \\ & & 0 & \vdots & & C_P A_P^{N-1} B_P \\ \vdots & & \vdots & \vdots & & \vdots \\ 0 & & 0 & C_P A_P^{N-i} B_P & & C_P A_P^{N-i} B_P \end{bmatrix} \begin{bmatrix} e(kN+i_1) \\ e(kN+i_2) \\ \vdots \\ e(kN+i_M) \\ e((k+1)N+i_1) \\ e((k+1)N+i_2) \\ \vdots \\ e((k+1)N+i_M) \end{bmatrix} \tag{4.56}$$

This is causal and is the lifted form of the unlifted point-to-point update (4.46). □

The form of the lifted point-to-point update (4.56) may appear complex, but can be transparently interpreted as follows. First, note that the two sum terms within the single sample unlifted point-to-point RC update (4.46) correspond to the left and right halves of the non-zero diagonal band matrix (tridiagonal form) within the stacked unlifted point-to-point update (4.56). The first summation term corresponds to the right half of the matrix and represents the points within the $(k+1)^{th}$ cycle that intersects with the moving convolution. Similarly, the second sum, and equivalently the left side of the matrix, represent the points in the k^{th} cycle that intersect with the moving convolution.

As the sample position moves forward, new points are added to the convolution in the $(k+1)^{th}$ cycle. However, because the cycle length is N and the impulse response has length $\leq N$ the same point in the previous cycle (k^{th}) is no longer included in the convolution. Eventually, all the points will be within the $(k+1)^{th}$ cycle, then when the sample enters the next cycle, the points will again effectively all be in the k^{th} cycle, leading the process to then repeat. The tridiagonal form is, therefore, purely a result of indexing. Note, that the size of the upper and lower triangular of the tridiagonal matrix are not dependent upon the number of extracted points (the size of M), but instead directly result from stacking iterations that are shifting with the sample position.

This can also be expressed graphically: Figure 4.5 shows 3 cycles, including the error, extracted points and impulse response, N samples behind the current sample position. Only points that intersect with the impulse (marked in green) are part of the convolution and effect the update at the active sample i (marked in green). The equivalent position in the previous cycles are also shown (marked in red).

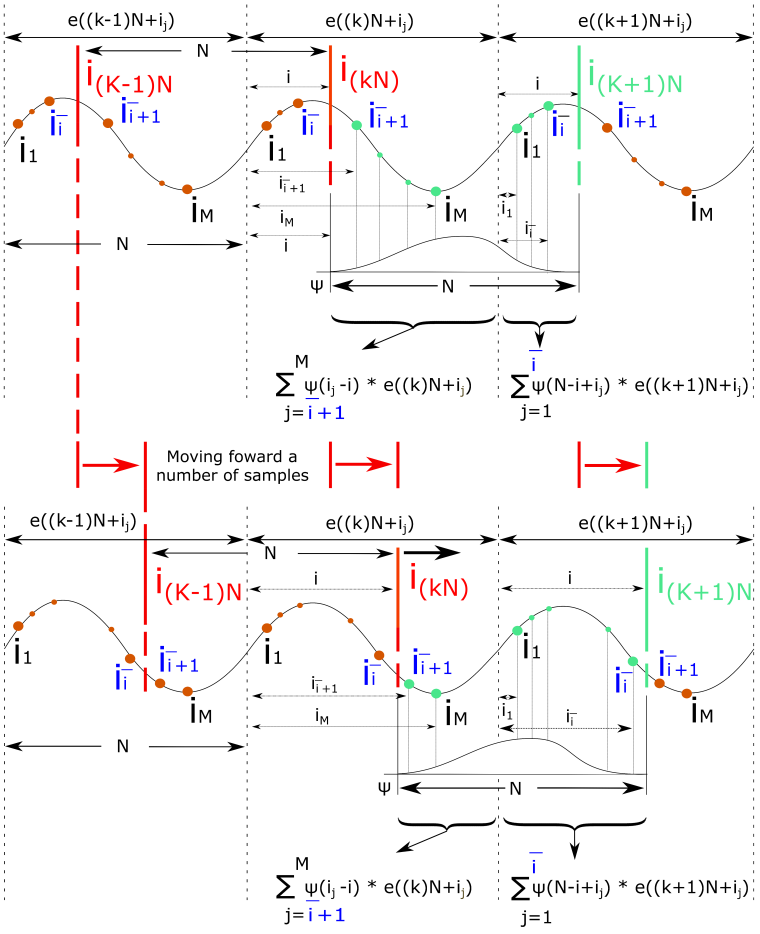

Figure 4.5: Graphical depiction of update (4.46) and its equivalent unlifted form (4.56).

Figure 4.5 provides additional detail by showing points with positional importance as larger dots. These dots are labelled as follows: labels in black are static; for example, the first point i_1 and last point i_M in the cycle. Labels in blue are dependent upon the sample position which means they change with time, such as the point previous to the current sample, $i_{\bar{i}}$, and point following the current sample, $i_{\bar{i}+1}$. The difference between the upper and lower image of Figure 4.5 demonstrates i moving forward a number of samples. The impulse response follows the active sample position, resulting in new points entering the convolution (within the $(k+1)^{th}$ cycle). Consequently, the same points within the previous k^{th} cycle are no longer part of the convolution. This is due to the conditions on the length of the impulse response, which ensures causality. This produces the tridiagonal non-zero form discussed above.

Theorem 4.1 showed that the lifted point-to-point RC update, given by (4.45), and the unlifted form in (4.46), converges to a fixed signal $\hat{\boldsymbol{u}}$. The next result takes this further by showing that $\hat{\boldsymbol{u}}$ is the minimum control effort solution.

Theorem 4.5. *The converged control signal (4.28) resulting from applying the point-to-point update (4.45) is the minimum control effort signal satisfying*

$$\hat{\boldsymbol{u}} := \min_{\hat{\boldsymbol{u}}} \|\boldsymbol{u}\|^2 \quad \textit{such that} \quad \boldsymbol{r}^{\Phi} = \boldsymbol{\Phi}\boldsymbol{P}\hat{\boldsymbol{u}} \tag{4.57}$$

Proof. From the repeated application of the state-space plant dynamics (4.19) we have

$$\boldsymbol{y}(k+1) = \boldsymbol{D}_P\boldsymbol{u}(k+1) + \boldsymbol{C}_P\boldsymbol{B}_P\boldsymbol{u}(k) + \boldsymbol{C}_P\boldsymbol{A}_P\boldsymbol{B}_P\boldsymbol{u}(k-1)\cdots \tag{4.58}$$

where convergence implies $\boldsymbol{u}(k) = \hat{\boldsymbol{u}} \;\; \forall k$. Hence from applying the causality condition (4.40),

$$\boldsymbol{y}(k) = \big(\boldsymbol{D}_P + \boldsymbol{C}_P\boldsymbol{B}_P\big)\hat{\boldsymbol{u}} \quad \forall k, \tag{4.59}$$

and

$$\bar{\boldsymbol{\Phi}}\boldsymbol{y}(k) = \bar{\boldsymbol{\Phi}}\big(\boldsymbol{D}_P + \boldsymbol{C}_P\boldsymbol{B}_P\big)\hat{\boldsymbol{u}} \quad \forall k. \tag{4.60}$$

As convergence also implies $\Phi\boldsymbol{y}(k) = \boldsymbol{r}^{\Phi} \;\; \forall k$, applying the pseudo-inverse of the plant gives the solution to the optimisation (4.57), resulting in

$$\hat{\boldsymbol{u}} = \big(\bar{\boldsymbol{\Phi}}\big(\boldsymbol{D}_P + \boldsymbol{C}_P\boldsymbol{B}_P\big)\big)^{\dagger}\boldsymbol{r}^{\Phi} \tag{4.61}$$

where the matrix pseudo-inverse is defined by $A^{\dagger} := A^{\top}\big(AA^{\top}\big)^{-1}$.

This can be confirmed by finding the limiting solution to the repeated application of the lifted point-to-point gradient implementation (4.56) (infinite series solution). This is given by

$$\boldsymbol{u}(k+1) = \boldsymbol{u}(k) + \beta(\bar{\boldsymbol{\Phi}}\boldsymbol{D}_P)^{\top}\bar{\boldsymbol{\Phi}}\boldsymbol{e}(k) + \beta(\bar{\boldsymbol{\Phi}}\boldsymbol{C}_P\boldsymbol{B}_P)^{\top}\bar{\boldsymbol{\Phi}}\boldsymbol{e}(k+1). \tag{4.62}$$

By substituting $\bar{\boldsymbol{\Phi}}\mathbf{e}(k) = \mathbf{r}^{\Phi} - \bar{\boldsymbol{\Phi}}\mathbf{y}(k)$ and $\boldsymbol{y}(k) = \big(\boldsymbol{D}_P + \boldsymbol{C}_P\boldsymbol{B}_P\big)\hat{\boldsymbol{u}}$ into (4.62), the error terms are removed, giving the infinite series for point-to-point RC implementation in terms of $\boldsymbol{u}$, $\boldsymbol{r}$ and the plant dynamics. This gives

$$\begin{aligned}\boldsymbol{u}(k+1) =& \boldsymbol{u}(k) + \beta\big(\bar{\boldsymbol{\Phi}}\big(\boldsymbol{D}_P + \boldsymbol{C}_P\boldsymbol{B}_P\big)\big)^{\top}\boldsymbol{r}^{\Phi} - \beta\big((\bar{\boldsymbol{\Phi}}\boldsymbol{D}_P)^{\top}\bar{\boldsymbol{\Phi}}\boldsymbol{D}_P + (\bar{\boldsymbol{\Phi}}\boldsymbol{C}_P\boldsymbol{B}_P)^{\top}\bar{\boldsymbol{\Phi}}\boldsymbol{C}_P\boldsymbol{B}_P\big)\boldsymbol{u}(k) \\ & - \beta(\bar{\boldsymbol{\Phi}}\boldsymbol{D}_P)^{\top}\bar{\boldsymbol{\Phi}}\boldsymbol{C}_P\boldsymbol{B}_P\boldsymbol{u}(k-1) - \beta(\bar{\boldsymbol{\Phi}}\boldsymbol{C}_P\boldsymbol{B}_P)^{\top}\bar{\boldsymbol{\Phi}}\boldsymbol{D}_P\boldsymbol{u}(k+1).\end{aligned}$$

and by gathering terms

$$\begin{aligned}\boldsymbol{u}(k+1) =& \Big[I + \beta(\bar{\boldsymbol{\Phi}}\boldsymbol{C}_P\boldsymbol{B}_P)^{\top}\bar{\boldsymbol{\Phi}}\boldsymbol{D}_P\Big]^{-1}\Big\{\beta\big(\bar{\boldsymbol{\Phi}}\big(\boldsymbol{D}_P + \boldsymbol{C}_P\boldsymbol{B}_P\big)\big)^{\top}\boldsymbol{r}^{\Phi} \\ & - \beta(\bar{\boldsymbol{\Phi}}\boldsymbol{D}_P)^{\top}\bar{\boldsymbol{\Phi}}\boldsymbol{C}_P\boldsymbol{B}_P\boldsymbol{u}(k-1) \\ & + \Big[I - \beta\big((\bar{\boldsymbol{\Phi}}\boldsymbol{D}_P)^{\top}\bar{\boldsymbol{\Phi}}\boldsymbol{D}_P + (\bar{\boldsymbol{\Phi}}\boldsymbol{C}_P\boldsymbol{B}_P)^{\top}\bar{\boldsymbol{\Phi}}\boldsymbol{C}_P\boldsymbol{B}_P\big)\Big]\boldsymbol{u}(k)\Big\}\end{aligned} \tag{4.63}$$

the infinite series can now be considered. The general form is,

$$\boldsymbol{u}(k+1) = a\boldsymbol{u}(k) + b\boldsymbol{u}(k-1) + c. \tag{4.64}$$

Through the repeated application of the general input update (4.64), the underlying matrix equation can be given in block matrix form

$$\begin{bmatrix} \boldsymbol{u}(k+1) \\ \boldsymbol{u}(k+2) \end{bmatrix} = \underbrace{\begin{bmatrix} b & a \\ ab & a^2+b \end{bmatrix}}_{\Xi}\begin{bmatrix} \boldsymbol{u}(k-1) \\ \boldsymbol{u}(k) \end{bmatrix} + \underbrace{\begin{bmatrix} c \\ ac+c \end{bmatrix}}_{\Theta}.$$

Assuming $\rho(\Xi) < 1$ (the series converges), then block matrix inverse relations, see, e.g. Lu and Shiou (2002), can be used to find the converged solution $\boldsymbol{u}(\infty)$. The general

series form is given by

$$
\begin{aligned}
&\begin{bmatrix}\boldsymbol{u}(\infty)\\ \boldsymbol{u}(\infty)\end{bmatrix} = \sum_{i=1}^{\infty}\Xi^i\Theta = (I-\Xi)^{-1}\Theta\\
&= \begin{bmatrix} I-b & -a \\ -ab & I-a^2-b\end{bmatrix}^{-1}\begin{bmatrix} c \\ ac+c\end{bmatrix}\\
&= \left[\begin{bmatrix} \big((I-b)-a(I-a^2-b)^{-1}ab\big)^{-1}, & \big((I-b)-a(I-a^2-b)^{-1}ab\big)^{-1}a(I-a^2-b)^{-1}\\ \big((I-a^2-b)-ab(I-b)^{-1}a\big)^{-1}ab(I-b)^{-1}, & \big((I-a^2-b)-ab(I-b)^{-1}a\big)^{-1}\end{bmatrix}\right.\\
&\left.\times\begin{bmatrix} c\\ (a+I)c\end{bmatrix}\right]\\
&= \begin{bmatrix} \big((I-b)-a(I-a^2-b)^{-1}ab\big)^{-1}\big(I+a(I-a^2-b)^{-1}(a+I)\big)c\\ \big((I-a^2-b)-a(I-b)^{-1}a+a^2\big)^{-1}(a+I-b)(I-b)^{-1}c\end{bmatrix}\\
&= \begin{bmatrix} \big(\big(I+a((I-b)-a^2)^{-1}(a+I)\big)((I-b)-a)\big)^{-1}\big(I+a(I-a^2-b)^{-1}(a+I)\big)c\\ \big((a+(I-b))(I-b)^{-1}(I-b-a)^{-1}\big)^{-1}(a+I-b)(I-b)^{-1}c\end{bmatrix}\\
&= \begin{bmatrix} (I-b-a)^{-1}c\\ (I-b-a)^{-1}c\end{bmatrix}
\end{aligned}
\tag{4.65}
$$

Now, comparing the state-space series (4.63) and the general form of the solution (4.64), the solution to the infinite series can be found. First,

$$
\begin{aligned}
(I-a-b) =&\Big[I+\beta(\bar{\boldsymbol{\Phi}}\boldsymbol{C}_P\boldsymbol{B}_P)^\top\bar{\boldsymbol{\Phi}}\boldsymbol{D}_P\Big]^{-1}\beta\Big\{(\bar{\boldsymbol{\Phi}}\boldsymbol{D}_P)^\top\bar{\boldsymbol{\Phi}}\boldsymbol{D}_P+(\bar{\boldsymbol{\Phi}}\boldsymbol{C}_P\boldsymbol{B}_P)^\top\bar{\boldsymbol{\Phi}}\boldsymbol{C}_P\boldsymbol{B}_P\\
&+(\bar{\boldsymbol{\Phi}}\boldsymbol{D}_P)^\top\bar{\boldsymbol{\Phi}}\boldsymbol{C}_P\boldsymbol{B}_P+(\bar{\boldsymbol{\Phi}}\boldsymbol{C}_P\boldsymbol{B}_P)^\top\bar{\boldsymbol{\Phi}}\boldsymbol{D}_P\Big\}
\end{aligned}
$$

now, consider the state-space form equivalent to $(I-a-b)^{-1}c$, which is the solution of $\boldsymbol{u}(k)$ as k tends to infinity. This is found by applying matrix pseudo-inverse relations which, with simplification follows

$$
\begin{aligned}
&\Big\{(\bar{\boldsymbol{\Phi}}\boldsymbol{D}_P)^\top\bar{\boldsymbol{\Phi}}\boldsymbol{D}_P+(\bar{\boldsymbol{\Phi}}\boldsymbol{C}_P\boldsymbol{B}_P)^\top\bar{\boldsymbol{\Phi}}\boldsymbol{C}_P\boldsymbol{B}_P\\
&\qquad+(\bar{\boldsymbol{\Phi}}\boldsymbol{D}_P)^\top\bar{\boldsymbol{\Phi}}\boldsymbol{C}_P\boldsymbol{B}_P+(\bar{\boldsymbol{\Phi}}\boldsymbol{C}_P\boldsymbol{B}_P)^\top\bar{\boldsymbol{\Phi}}\boldsymbol{D}_P\Big\}^{-1}\big(\bar{\boldsymbol{\Phi}}\big(\boldsymbol{D}_P+\boldsymbol{C}_P\boldsymbol{B}_P\big)\big)^\top\boldsymbol{r}^\Phi\\
&=\Big\{\big(\bar{\boldsymbol{\Phi}}\big(\boldsymbol{D}_P+\boldsymbol{C}_P\boldsymbol{B}_P\big)\big)^\top\bar{\boldsymbol{\Phi}}\big(\boldsymbol{D}_P+\boldsymbol{C}_P\boldsymbol{B}_P\big)\Big\}^{-1}\big(\bar{\boldsymbol{\Phi}}\big(\boldsymbol{D}_P+\boldsymbol{C}_P\boldsymbol{B}_P\big)\big)^\top\boldsymbol{r}^\Phi\\
&=\big(\bar{\boldsymbol{\Phi}}\big(\boldsymbol{D}_P+\boldsymbol{C}_P\boldsymbol{B}_P\big)\big)^\dagger\boldsymbol{r}^\Phi
\end{aligned}
\tag{4.66}
$$

as required. □

Theorem 4.5 shows the lifted point-to-point RC update (4.45) and equivalent unlifted point-to-point RC update (4.46) converge to the minimum effort solution (i.e. smallest amount of FES that solves the tracking problem). However, research has established human movement is a minimum jerk movement rather than simply a minimum energy one (Morasso, 1981; Krebs et al., 1998; Flash and Hogan, 1985). This was illustrated

by Tack et al. (2007) where it was found that the walking speed at a minimum jerk cost function coincidences with the preferred walking speed for an individual. Therefore the update is now generalised such that an operator can be designed to converge to any minimum norm solution, such as the minimisation of velocity, acceleration, energy and jerk norms.

4.4 Generalizing the Minimum Control Effort

The aim is now to generalise Theorem 4.5 by altering the gradient algorithm to include a filter $\boldsymbol{F}$. This will be seen to change the control signal input solution to solve a different minimisation problem.

Theorem 4.6. *Let the lifted point-to-point gradient RC update (4.45) be modified to assume the form*

$$\boldsymbol{u}(k+1) = \boldsymbol{u}(k) + \beta \boldsymbol{F}\boldsymbol{F}^{*}\big(\boldsymbol{\Phi}\boldsymbol{P}(\boldsymbol{q})\big)^{*}\boldsymbol{e}^{\Phi}(k) \tag{4.67}$$

where $\boldsymbol{F}$ is an operator with unlifted state-space matrices $\{A_F, B_F, C_F, D_F\}$ satisfying

$$C_F A_F^i B_F = 0 \quad \forall \quad i \geq n_F, \tag{4.68}$$

with $n_F \leq N$, and β is a scalar satisfying the unlifted condition

$$0 < \beta < \frac{2}{\sup_{\omega\in[0,\pi]} |P(e^{j\omega})|^2 |F(e^{j\omega})|^2}. \tag{4.69}$$

Then the converged control signal (4.28) satisfies the weighted minimum control effort condition

$$\hat{\boldsymbol{u}} := \min_{\hat{\boldsymbol{u}}} \|\boldsymbol{H}\boldsymbol{u}\|^2 \quad \textit{such that} \quad \boldsymbol{r}^{\Phi} = \boldsymbol{\Phi}\boldsymbol{P}\boldsymbol{u} \tag{4.70}$$

where operator $\boldsymbol{H}$ has a steady-state equal to the inverse of that of $\boldsymbol{F}$.

Proof. As before, the steady-state solution satisfies $\boldsymbol{u}(k) = \hat{\boldsymbol{u}} \ \forall k$, because Theorem 4.1 is satisfied. Therefore the operators can now be replaced by

$$\boldsymbol{P} = \big(\boldsymbol{D}_P + \boldsymbol{C}_P\boldsymbol{B}_P\big). \tag{4.71}$$

Similarly for the minimum control effort weighting H, with lifted state-space matrices $\{\boldsymbol{A}_H, \boldsymbol{B}_H, \boldsymbol{C}_H, \boldsymbol{D}_H\}$ analogous to (4.19), we have

$$\boldsymbol{H} = \big(\boldsymbol{D}_H + \boldsymbol{C}_H\boldsymbol{B}_H\big). \tag{4.72}$$

The method of Lagrangian multipliers, λ, is then applied to find the minimum solution, $\hat{\boldsymbol{u}}$, with respect to constraints (4.70). The Lagrangian expression is defined by

$$\text{argmin}\{J(\boldsymbol{u})\}, \ J(\boldsymbol{u}) = \frac{1}{2}\big(\boldsymbol{H}\boldsymbol{u}\big)^{\top}\boldsymbol{H}\boldsymbol{u} + \lambda^{\top}\big(\boldsymbol{\Phi}\boldsymbol{P}\boldsymbol{u} - \boldsymbol{r}^{\Phi}\big) \tag{4.73}$$

Therefore, since the dynamics of the inverse filter (4.72) are full rank (i.e. all columns and rows and linearly independent) the solution satisfies

$$
\begin{aligned}
(\boldsymbol{H})^\top(\boldsymbol{H})\hat{\boldsymbol{u}} + (\boldsymbol{\Phi}P)^\top\lambda &= 0 \\
\Rightarrow \hat{\boldsymbol{u}} &= -\big((\boldsymbol{H})^\top(\boldsymbol{H})\big)^{-1}\big(\Phi(\boldsymbol{P})\big)^\top\lambda \\
\Rightarrow \boldsymbol{\Phi}(\boldsymbol{P})\hat{\boldsymbol{u}} &= -\boldsymbol{\Phi}(\boldsymbol{P})\big((\boldsymbol{H})^\top(\boldsymbol{H})\big)^{-1}\big(\boldsymbol{\Phi}(\boldsymbol{P})\big)^\top\lambda
\end{aligned}
\tag{4.74}
$$

and since $M \leq N$, by post-multiplying (4.73) by $(\boldsymbol{P})$ and substituting $\boldsymbol{\Phi}(\boldsymbol{P})\boldsymbol{u}^* = \boldsymbol{r}^\Phi$ and (4.73) back in to remove the Lagrangian multiplier, λ, the minimum energy solution in state space form is given

$$
\begin{aligned}
\lambda &= -\Big(\boldsymbol{\Phi}(\boldsymbol{P})\big((\boldsymbol{H})^\top(\boldsymbol{H})\big)^{-1}\big(\boldsymbol{\Phi}(\boldsymbol{P})\big)^\top\Big)^{-1}\boldsymbol{r}^\Phi \\
\Rightarrow \hat{\boldsymbol{u}} &= \Big(\boldsymbol{\Phi}(\boldsymbol{P})\big((\boldsymbol{H})^\top(\boldsymbol{H})\big)^{-1}\big(\boldsymbol{\Phi}(\boldsymbol{P})\big)^\top\Big)^{-1}\boldsymbol{r}^\Phi \times \big((\boldsymbol{H})^\top(\boldsymbol{H})\big)^{-1}\big(\boldsymbol{\Phi}(\boldsymbol{P})\big)^\top
\end{aligned}
\tag{4.75}
$$

To write the solution $\hat{\boldsymbol{u}}$ in a form similar to the minimum control effort given by (4.61), the weighted pseudo-inverse form $A^\dagger := XA^\top\big(AXA^\top\big)^{-1}$ is required where $X = \big((\boldsymbol{D}_H + \boldsymbol{C}_H\boldsymbol{B}_H)^\top(\boldsymbol{D}_H + \boldsymbol{C}_H\boldsymbol{B}_H)\big)^{-1}$. By now focusing on the input control solution to the filtered update minimisation problem (4.67), it can be shown to have an equivilant value to the state-space minimum energy solution (4.75). By partitioning (4.67) consider $\boldsymbol{v}(k+1) = (\boldsymbol{\Phi}\boldsymbol{P}\boldsymbol{F})\boldsymbol{u}(k+1)$;

$$
\boldsymbol{v}(k+1) = \boldsymbol{\Phi}\boldsymbol{D}_P\boldsymbol{D}_F\boldsymbol{u}(k+1) + \boldsymbol{\Phi}\big(\boldsymbol{D}_P\boldsymbol{C}_F\boldsymbol{B}_F + \boldsymbol{C}_P\boldsymbol{B}_P\boldsymbol{D}_F\big)\boldsymbol{u}(k) + \boldsymbol{\Phi}\underbrace{\boldsymbol{C}_P\boldsymbol{B}_P\boldsymbol{C}_F\boldsymbol{B}_F}_{=0}\boldsymbol{u}(k-1) \tag{4.76}
$$

where the constraint $n_F + n_P \leq N$ is applied to the impulse response length of $\boldsymbol{F}$ and $\boldsymbol{P}$ to ensure $\boldsymbol{C}_P\boldsymbol{B}_P\boldsymbol{C}_F\boldsymbol{B}_F = 0$. Therefore the adjoint, $\boldsymbol{v} = (\boldsymbol{\Phi}(\boldsymbol{P}\boldsymbol{F})^*\boldsymbol{u}$ is given by

$$
\boldsymbol{v}(k) = \big(\boldsymbol{\Phi}\boldsymbol{D}_P\boldsymbol{D}_F\big)^\top\boldsymbol{u}(k) + \big(\boldsymbol{\Phi}\boldsymbol{D}_P\boldsymbol{C}_F\boldsymbol{B}_F + \boldsymbol{\Phi}\boldsymbol{C}_P\boldsymbol{B}_P\boldsymbol{D}_F\big)^\top\boldsymbol{u}(k+1)
$$

and then

$$
\begin{aligned}
\boldsymbol{v}(k) &= \boldsymbol{F}(\boldsymbol{\Phi}\boldsymbol{P}\boldsymbol{F})^*\boldsymbol{\Phi}\boldsymbol{e}(k) \\
&= \boldsymbol{D}_F\big(\boldsymbol{\Phi}\boldsymbol{D}_P\boldsymbol{D}_F\big)^\top\boldsymbol{\Phi}\boldsymbol{e}(k) + \boldsymbol{D}_F\big(\boldsymbol{\Phi}\boldsymbol{D}_P\boldsymbol{C}_F\boldsymbol{B}_F + \boldsymbol{\Phi}\boldsymbol{C}_P\boldsymbol{B}_P\boldsymbol{D}_F\big)^\top\boldsymbol{e}(k+1) \\
&+ \boldsymbol{C}_F\boldsymbol{B}_F\big(\boldsymbol{\Phi}\boldsymbol{D}_P\boldsymbol{D}_F\big)^\top\boldsymbol{e}(k-1) + \boldsymbol{C}_F\boldsymbol{B}_F\big(\boldsymbol{\Phi}\boldsymbol{D}_P\boldsymbol{C}_F\boldsymbol{B}_F + \boldsymbol{\Phi}\boldsymbol{C}_P\boldsymbol{B}_P\boldsymbol{D}_F\big)^\top\boldsymbol{e}(k) \\
&= \underbrace{\boldsymbol{D}_F\big(\boldsymbol{\Phi}\boldsymbol{D}_P\boldsymbol{C}_F\boldsymbol{B}_F + \boldsymbol{\Phi}\boldsymbol{C}_P\boldsymbol{B}_P\boldsymbol{D}_F\big)^\top}_{\alpha_2}\boldsymbol{e}(k+1) + \underbrace{\boldsymbol{C}_F\boldsymbol{B}_F\big(\boldsymbol{\Phi}\boldsymbol{D}_P\boldsymbol{D}_F\big)^\top}_{\alpha_3}\boldsymbol{e}(k-1) \\
&+ \underbrace{\Big(\boldsymbol{D}_F\big(\boldsymbol{\Phi}\boldsymbol{D}_P\boldsymbol{D}_F\big)^\top + \boldsymbol{C}_F\boldsymbol{B}_F\big(\boldsymbol{\Phi}\boldsymbol{D}_P\boldsymbol{C}_F\boldsymbol{B}_F + \boldsymbol{\Phi}\boldsymbol{C}_P\boldsymbol{B}_P\boldsymbol{D}_F\big)^\top\Big)}_{\alpha_1}\boldsymbol{e}(k)
\end{aligned}
$$

so that, following additional simplifications, this leads to

$$
\begin{aligned}
\boldsymbol{v}(k) =& (\alpha_1 + \alpha_2 + \alpha_3)\boldsymbol{r} - \boldsymbol{\Phi}\boldsymbol{D}_P\alpha_1\boldsymbol{u}(k) - \boldsymbol{\Phi}\boldsymbol{D}_P\alpha_2\boldsymbol{u}(k+1) - \boldsymbol{\Phi}\boldsymbol{D}_P\alpha_3\boldsymbol{u}(k-1) \\
&- \boldsymbol{\Phi}\boldsymbol{C}_P\boldsymbol{B}_P\alpha_1\boldsymbol{u}(k-1) - \boldsymbol{\Phi}\boldsymbol{C}_P\boldsymbol{B}_P\alpha_2\boldsymbol{u}(k) - \underbrace{\boldsymbol{\Phi}\boldsymbol{C}_P\boldsymbol{B}_P\alpha_3}_{=0}\boldsymbol{u}(k-2).
\end{aligned}
$$

By subsituting (4.77) into the filtered lifted point-to-point RC update (4.67), we obtain

$$\begin{aligned}\boldsymbol{u}(k+1) =& \boldsymbol{u}(k) + \beta \boldsymbol{v}(k) \\ =& \Big(I + \beta \boldsymbol{\Phi} \boldsymbol{D}_P \alpha_2\Big)^{-1} \Big\{ (\alpha_1 + \alpha_2 + \alpha_3)\boldsymbol{r} + \big(I - \beta \boldsymbol{\Phi} \boldsymbol{D}_P \alpha_1 - \beta \boldsymbol{\Phi} \boldsymbol{C}_P \boldsymbol{B}_P \alpha_2\big)\boldsymbol{u}(k) \\ & - \beta \big(\boldsymbol{\Phi} \boldsymbol{D}_P \alpha_3 + \boldsymbol{\Phi} \boldsymbol{C}_P \boldsymbol{B}_P \alpha_1\big)\boldsymbol{u}(k-1) \Big\} \end{aligned} \tag{4.77}$$

and a solution is provided by comparing (4.64) and (4.65) with (4.77) to give

$$\begin{aligned}\boldsymbol{u}_\infty =& \Big[I - \Big(I + \beta \boldsymbol{\Phi} \boldsymbol{D}_P \alpha_2\Big)^{-1} \big(I - \boldsymbol{\Phi} \beta \boldsymbol{D}_P \alpha_1 - \beta \boldsymbol{\Phi} \boldsymbol{C}_P \boldsymbol{B}_P \alpha_2\big) \\ & - \Big(I + \beta \boldsymbol{\Phi} \boldsymbol{D}_P \alpha_2\Big)^{-1} \beta \big(\boldsymbol{\Phi} D_P \alpha_3 + \boldsymbol{\Phi} \boldsymbol{C}_P \boldsymbol{B}_P \alpha_1\big) \Big]^{-1} \\ & \times \Big(I + \beta \boldsymbol{\Phi} D_P \alpha_2\Big)^{-1} (\alpha_1 + \alpha_2 + \alpha_3)\boldsymbol{r}. \end{aligned}$$

from which simplifying gives

$$\begin{aligned}\boldsymbol{u}_\infty =& \Big[\Big(I + \beta \boldsymbol{\Phi} \boldsymbol{D}_P \alpha_2\Big)^{-1} \beta \big(\boldsymbol{\Phi} \boldsymbol{D}_P \alpha_2 + \boldsymbol{\Phi} \boldsymbol{D}_P \alpha_1 + \boldsymbol{\Phi} \boldsymbol{C}_P \boldsymbol{B}_P \alpha_2 + \boldsymbol{\Phi} \boldsymbol{D}_P \alpha_3 + \boldsymbol{\Phi} \boldsymbol{C}_P \boldsymbol{B}_P \alpha_1\big) \Big]^{-1} \\ & \times \Big(I + \beta \boldsymbol{\Phi} \boldsymbol{D}_P \alpha_2\Big)^{-1} (\alpha_1 + \alpha_2 + \alpha_3)\boldsymbol{r}. \end{aligned} \tag{4.78}$$

Expanding the elements within the square brackets of (4.78) gives

$$\begin{aligned}\boldsymbol{\Phi} \boldsymbol{D}_P \alpha_1 + \boldsymbol{\Phi} \boldsymbol{C}_P \boldsymbol{B}_P \alpha_2 =& \big(\boldsymbol{\Phi} \boldsymbol{D}_P \boldsymbol{C}_F \boldsymbol{B}_F + \boldsymbol{\Phi} \boldsymbol{C}_P \boldsymbol{B}_P \boldsymbol{D}_F\big)\big(\boldsymbol{\Phi} \boldsymbol{D}_P \boldsymbol{C}_F \boldsymbol{B}_F + \boldsymbol{\Phi} \boldsymbol{C}_P \boldsymbol{B}_P \boldsymbol{D}_F\big)^\top \\ & + \boldsymbol{\Phi} \boldsymbol{D}_P \boldsymbol{D}_F \big(\boldsymbol{\Phi} \boldsymbol{D}_P \boldsymbol{D}_F\big)^\top \end{aligned} \tag{4.79}$$

$$\boldsymbol{\Phi} \boldsymbol{D}_P \alpha_3 + \boldsymbol{\Phi} \boldsymbol{C}_P \boldsymbol{B}_P \alpha_1 = \big(\boldsymbol{\Phi} \boldsymbol{D}_P \boldsymbol{C}_F \boldsymbol{B}_F + \boldsymbol{\Phi} \boldsymbol{C}_P \boldsymbol{B}_P \boldsymbol{D}_F\big)\big(\boldsymbol{\Phi} \boldsymbol{D}_P \boldsymbol{D}_F\big)^\top \boldsymbol{\Phi} \tag{4.80}$$

$$\boldsymbol{\Phi} \boldsymbol{D}_P \alpha_2 = \boldsymbol{\Phi} \boldsymbol{D}_P \boldsymbol{D}_F \big(\boldsymbol{\Phi} \boldsymbol{D}_P \boldsymbol{C}_F \boldsymbol{B}_F + \boldsymbol{\Phi} \boldsymbol{C}_P \boldsymbol{B}_P \boldsymbol{D}_F\big)^\top \tag{4.81}$$

and substituting them back into (4.78) gives

$$\begin{aligned}& \big(\boldsymbol{\Phi} \boldsymbol{D}_P \boldsymbol{D}_F + \big(\boldsymbol{\Phi} \boldsymbol{D}_P \boldsymbol{C}_F \boldsymbol{B}_F + \boldsymbol{\Phi} \boldsymbol{C}_P \boldsymbol{B}_P \boldsymbol{D}_F\big)\big)\big(\boldsymbol{\Phi} \boldsymbol{D}_P \boldsymbol{D}_F + \big(\boldsymbol{\Phi} \boldsymbol{D}_P \boldsymbol{C}_F \boldsymbol{B}_F + \boldsymbol{\Phi} \boldsymbol{C}_P \boldsymbol{B}_P \boldsymbol{D}_F\big)\big)^\top \\ & = \boldsymbol{\Phi} \big(\boldsymbol{D}_P + \boldsymbol{C}_P \boldsymbol{B}_P\big)\big(\boldsymbol{D}_F + \boldsymbol{C}_F \boldsymbol{B}_F\big)\Big(\boldsymbol{\Phi} \big(\boldsymbol{D}_P + \boldsymbol{C}_P \boldsymbol{B}_P\big)\big(\boldsymbol{D}_F + \boldsymbol{C}_F \boldsymbol{B}_F\big)\Big)^\top \\ & = \boldsymbol{\Phi} \big(\boldsymbol{D}_P + \boldsymbol{C}_P \boldsymbol{B}_P\big)\big(\boldsymbol{D}_F + \boldsymbol{C}_F \boldsymbol{B}_F\big)\big(\boldsymbol{D}_F + \boldsymbol{C}_F \boldsymbol{B}_F\big)^\top \big(\boldsymbol{\Phi} (\boldsymbol{D}_P + \boldsymbol{C}_P \boldsymbol{B}_P)\big)^\top \end{aligned} \tag{4.82}$$

Similarly, by expanding and gathering terms, $\alpha_1 + \alpha_2 + \alpha_3$ are equal to

$$\alpha_1 + \alpha_2 + \alpha_3 = \big(\boldsymbol{D}_F + \boldsymbol{C}_F \boldsymbol{B}_F\big)\big(\boldsymbol{D}_F + \boldsymbol{C}_F \boldsymbol{B}_F\big)^\top \big(\boldsymbol{\Phi} (\boldsymbol{D}_P + \boldsymbol{C}_P \boldsymbol{B}_P)\big)^\top. \tag{4.83}$$

Substituting the previous expansions (4.82) and (4.83) into the infinite series input solution (4.78) gives

$$\begin{aligned}\boldsymbol{u}_\infty =&\Big[\boldsymbol{\Phi}\big(\boldsymbol{D}_P+\boldsymbol{C}_P\boldsymbol{B}_P\big)\big(\boldsymbol{D}_F+\boldsymbol{C}_F\boldsymbol{B}_F\big)\big(\boldsymbol{D}_F+\boldsymbol{C}_F\boldsymbol{B}_F\big)^\top\big(\boldsymbol{\Phi}(\boldsymbol{D}_P+\boldsymbol{C}_P\boldsymbol{B}_P)\big)^\top\Big]^{-1}\\ &\times\big(\boldsymbol{D}_F+\boldsymbol{C}_F\boldsymbol{B}_F\big)\big(\boldsymbol{D}_F+\boldsymbol{C}_F\boldsymbol{B}_F\big)^\top\big(\boldsymbol{\Phi}(\boldsymbol{D}_P+\boldsymbol{C}_P\boldsymbol{B}_P)\big)^\top\boldsymbol{r}^\Phi\end{aligned} \tag{4.84}$$

Now note that for any full rank square matrix A, $(A^\top A)^{-1}=A^{-1}(A^{-1})^\top$. Also note that $\big(\boldsymbol{D}_F+\boldsymbol{C}_F\boldsymbol{B}_F\big)=\big(\boldsymbol{D}_H+\boldsymbol{C}_H\boldsymbol{B}_H\big)^{-1}$ to give

$$\begin{aligned}\boldsymbol{u}_\infty =&\Big[\boldsymbol{\Phi}\big(\boldsymbol{D}_P+\boldsymbol{C}_P\boldsymbol{B}_P\big)\big(\big(\boldsymbol{D}_H+\boldsymbol{C}_H\boldsymbol{B}_H\big)^\top\big(\boldsymbol{D}_H+\boldsymbol{C}_H\boldsymbol{B}_H\big)\big)^{-1}\big(\boldsymbol{\Phi}(\boldsymbol{D}_P+\boldsymbol{C}_P\boldsymbol{B}_P)\big)^\top\Big]^{-1}\\ &\times\big(\big(\boldsymbol{D}_H+\boldsymbol{C}_H\boldsymbol{B}_H\big)^\top\big(\boldsymbol{D}_H+\boldsymbol{C}_H\boldsymbol{B}_H\big)\big)^{-1}\big(\boldsymbol{\Phi}(\boldsymbol{D}_P+\boldsymbol{C}_P\boldsymbol{B}_P)\big)^\top\boldsymbol{r}^\Phi\end{aligned} \tag{4.85}$$

which matches the solution to the Lagrangian expression (4.75) as required. □

To implement the new filtered lifted point-to-point RC update (4.67) in practice again requires conversion to an unlifted form, as was done previously in Proposition 4.4. This is derived next.

Proposition 4.7. *The filtered lifted point-to-point RC update (4.67) has equivalent unlifted form*

$$\begin{aligned}u((K+1)N+i) =&u(kN+i)+\beta\Big(\sum_{j=\underline{i}_f}^{M}\psi(n_f-i+i_j-N)e((k-1)N+i_j)\\ &+\sum_{j=\bar{i}_f}^{M}\psi(n_f+i_j-i)e(kN+i_j)\\ &+\sum_{j=1}^{\bar{i}}\psi(n_f+N+i_j-i)e((k+1)N+i_j)\Big)\end{aligned} \tag{4.86}$$

where $\bar{i}=\max_{j\geq 0}\{i_j|i_j\leq i, i_0=0\}$*, is the most recent point-to-point index,* $\bar{i}_f=\min_{j\geq 1}\{i_j|i_j\geq i-n_F\}$ *defines the first point appearing within the* $(k-1)^{th}$ *cycle, that is in the convolution window and* $\underline{i}_f=\min_{j\geq 1}\{i_j|i_j\geq i-n_F+N, i_{m+1}=2N\}$ *describes the first point within the* k *cycle that is in the convolution window. Function* $\psi(i):=\sum_{a=-n_F}^{n_F}\sum_{j=0}^{n_F}f(j)f(a+j)p(i+a)$ *where* $f(i)=C_FA_F^iB_F$*,* $p(i)=C_PA_P^iB_P$*, are the impulse responses of* $F(q)$ *and* $P(q)$ *respectively.*

Proof. Note we require impulse response lengths n_f, n_p of $F(q)$ and $P(q)$ respectively to satisfy $n_f+n_p\leq N$ for the system to be causal. First, writing $F(q)$ in the causal FIR form $v(q)=F(q)w(q)$, gives

$$v(i)=\sum_{j=0}^{n_f}f(j)w(i-j). \tag{4.87}$$

and by definition, its adjoint $F(q)^*$ has FIR form $w(q) = F(q)^* x(q)$, i.e.

$$w(i) = \sum_{j=0}^{n_f} f(j)x(i+j), \tag{4.88}$$

then $\boldsymbol{v} = \boldsymbol{F}\boldsymbol{F}^\top \boldsymbol{x}$ corresponds to the unlifted update

$$\begin{aligned} v(i) &= \sum_{j=0}^{n_f} f(j) \sum_{p=0}^{n_f} f(p)x(i-j+p) \\ &= \sum_{j=0}^{n_f} \sum_{a=-j}^{n_f-j} f(j)f(a+j)x(i-a) \\ &= \sum_{a=-n_f}^{n_f} \underbrace{\left\{ \sum_{j=-n_f}^{n_f} f(j)f(a+j) \right\}}_{h(a)} x(i-a) \end{aligned} \tag{4.89}$$

where by definition $h(a)$ is defined over $a \in [-n_f, n_f]$. Next, recall the lifted operator $\boldsymbol{x} = \big(\boldsymbol{\Phi}\boldsymbol{P}(\boldsymbol{q})\big)^* \boldsymbol{e}^\Phi(k)$ from equation (4.50) given by

$$\boldsymbol{x}(k) = (\bar{\boldsymbol{\Phi}}\boldsymbol{D}_P)^\top \bar{\boldsymbol{\Phi}}\boldsymbol{e}(k) + \sum_{i=1}^{\infty} \Big\{ \Big(\boldsymbol{C}_P \big(\boldsymbol{A}_P\big)^{i-1} \boldsymbol{B}_P \Big)^\top \bar{\boldsymbol{\Phi}}^\top \bar{\boldsymbol{\Phi}}\boldsymbol{e}(k+i) \Big\}, \tag{4.90}$$

and since the unlifted causality condition (4.40) for the update implies the unlifted causality condition for the filter (4.68), the lifted operator (4.90) simplifies to

$$\boldsymbol{x}(k) = (\bar{\boldsymbol{\Phi}}\boldsymbol{D}_P)^\top \bar{\boldsymbol{\Phi}}\boldsymbol{e}(k) + \boldsymbol{B}_P^\top (\bar{\boldsymbol{\Phi}}\boldsymbol{C}_P)^\top \bar{\boldsymbol{\Phi}}\boldsymbol{e}(k+1) \tag{4.91}$$

which has the unlifted form

$$\begin{aligned} x(kN+i) = &\sum_{j=1}^{\bar{i}-n_f} p(N+i_j-i)e((k+1)N+i_j) \\ &+ \sum_{j=\bar{i}+1}^{M} p(i_j-i)e(kN+i_j), \end{aligned} \tag{4.92}$$

where $\bar{i} = \max_j i_j \leq i$ is the most recent point-to-point index. Substituting the unlifted state-space form of $\boldsymbol{x} = \big(\boldsymbol{\Phi}\boldsymbol{P}(\boldsymbol{q})\big)^* \boldsymbol{e}^\Phi(k)$ given by (4.92) into the unlifted update (4.89) and then into the minimum control effort update (4.67) (i.e. $\boldsymbol{u}(k+1) =$

$\boldsymbol{u}(k) + \beta \boldsymbol{F}\boldsymbol{F}^*\big(\boldsymbol{\Phi}\boldsymbol{P}(\boldsymbol{q})\big)^* \boldsymbol{e}^{\Phi}(k))$ yields the unlifted filtered point-to-point RC update

$$\begin{aligned} u((k+1)N+i) &= u(kN+i) \\ &+ \beta\Big(\sum_{j=1}^{\bar{i}-n_f} \sum_{a=-n_f}^{n_f} h(a)p(N+i-i_j+a)e((k+1)N+i_j) \\ &+ \sum_{j=\bar{i}+1}^{M} \sum_{a=-n_f}^{n_f} h(a)p(i_j-i+a)e(kN+i_j)\Big), \end{aligned} \tag{4.93}$$

where, $p(i) = C_P A_P^i B_P$ is the impulse response of the unlifted plant $P(q)$, $h(a) = \sum_{j=-n_f}^{n_f} f(j)f(i+j)$ in which $f(i)$ is the impulse response of $F(q)$. Partitioning the sum into separate cycles, $k-1$, k and $k+1$, yields the form (4.86). This is achieved by noticing that if, $i < n_f$ ($i - n_f < 0$), then points in the previous cycle exist in the convolution. To include the overflow from $e(kN+i_j)$, an additional term, $e((k-1)N+i_j)$, emerges. □

Remark 4.8. The new point-to-point RC update (4.86), or (4.67), requires a suitable filter $f(q) = \frac{1}{h(q)}$ to be chosen. Perhaps the most important set of examples for assistance of human motor function is: $h(q) = \frac{1}{q^n}$, $n \geq 1$ (i.e. minimisation of velocity, acceleration, jerk norms etc.). These correspond to $f(q) = q^n$ where $n \geq 1$. However, their impulse responses are infinite and hence clearly cannot satisfy the requirement $n_f + n_p \leq N$. It is, therefore, necessary to replace them with suitable approximations, or to cut off the update when it becomes non-causal.

Remark 4.9. Selecting $F = I$ in Proposition 4.7 reduces the filtered unlifted update form (4.86) to the unlifted update (4.46).

A graphical description can also be given to interpret the generalised filtered point-to-point RC (4.86). Figure 4.6 shows the full update in operation. Previously, the point-to-point update was shown in Figure 4.5 to have a tridiagonal form; the filtered point-to-point RC update also has a tridiagonal form. However, due to the filter envelope, the total size of the convolution has increased (with an additional tail of length n_f) to include points before the previous sample i. Because of this, additional points in both the k^{th} and $(k-1)^{th}$ cycle are now included in the convolution.

An additional term not previously required in the point-to-point update is now required for points in the $(k-1)^{th}$ cycle. It is important to note that terms in the $(k-1)^{th}$ cycle may only exist in the convolution when $i - n_f < 0$, as this is the only time the impulse envelope enters the $(k-1)^{th}$ cycle. If this condition is not met the first summation term (within update (4.86)) returns zero. Additional points from the k^{th} cycle are also now included, assuming they exist and coincide within the envelope tail. The dependent $\bar{i}$ variable accounts for this, by changing the number of terms in the summation. It is important to note that, unlike previously, as points are no longer included in the convolution they are not replaced by the equivalent point in the k^{th} or $(k+1)^{th}$ cycles. Additionally, as points enter the $(k+1)^{th}$ convolution, their corresponding point in

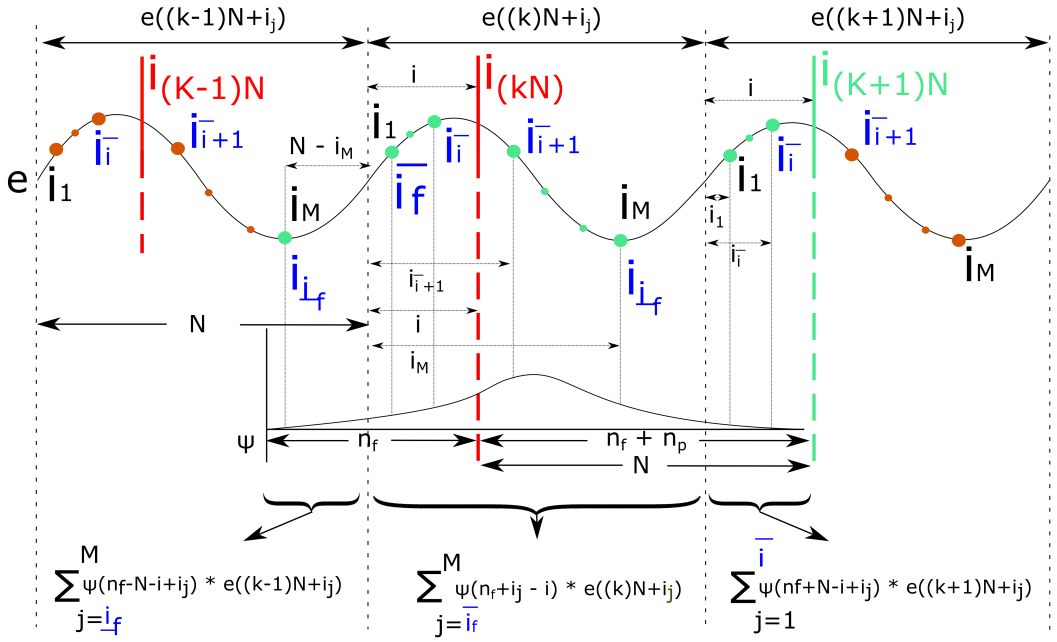

Figure 4.6: Graphical depiction of the filtered point-to-point RC update (4.86)

the k^{th} cycle is not removed due to the filter envelope tail, meaning they leave the convolution n_f samples later.

Figure 4.6 can be broken down into several segments, corresponding to how each part of the filtered point-to-point update (4.86) is calculated. Figure 4.7 shows this partition and how each segment relates to the terms within (4.86). The first segment convolves the error of any extracted points $(e((k-1)N+i_j))$ within the reference for the points after i in the $(k-1)^{th}$ cycle, with the corresponding value of the impulse response envelope $(\psi(n_f - N - i + i_j))$. Similarly, the second segment convolves the error of the points $(e((k)N+i_j))$ in the k^{th} cycle before i with the impulse response $(\psi(n_f - i + i_j))$. The number of points included in the first and second segments depends upon the length of the filter n_f. For example, in the case where $F = I$ (no filter), the first and second segments do not include any points and so do not exist at all. The third segment convolves the errors $(e((k)N+i_j))$ and impulse $(\psi(n_f - i + i_j))$ for the points in the k^{th} cycle after i. Finally, the fourth segment convolves the errors $(e((k+1)N+i_j))$ of the extracted points that coincide with the impulse $(\psi(n_f + N - i + i_j))$ for the points in the $(k+1)^{th}$ cycle before i.

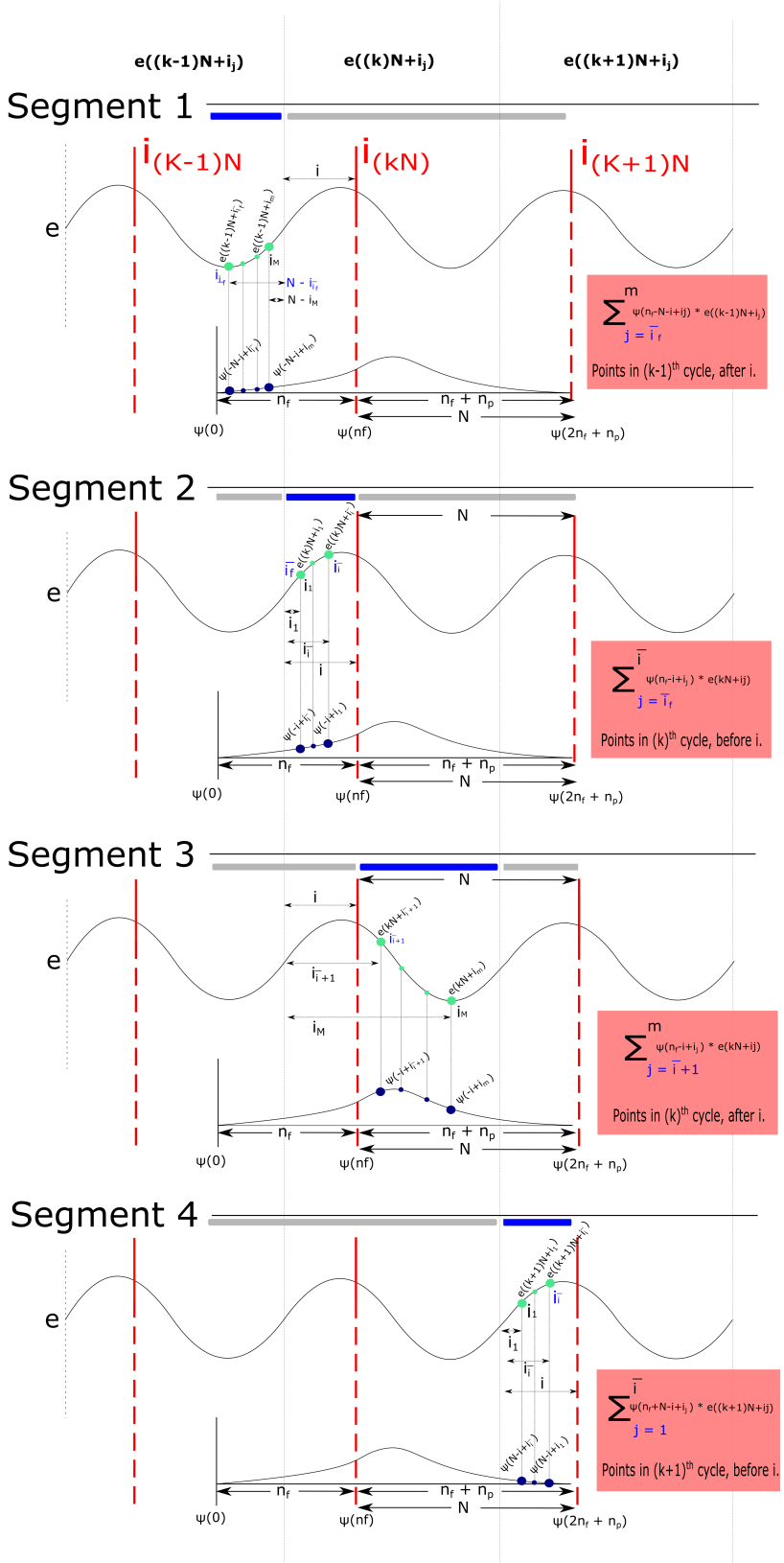

Figure 4.7: A segmented graphical depiction of the filtered point-to-point RC update

4.5 Weighted Point-to-Point Repetitive Control

A comprehensive framework has been derived in the previous sections to allow key points of a reference to be extracted and tracked, reducing the amount of data passed between cycles. Additionally, an operator has been designed to enable the control signal to converge to any minimum energy norm solution. A further simple modification to the framework can allow a greater control of robustness, convergence evolution and speed. This is achieved by influencing the learning rate of individual points. To alter the convergence of specific points, the learning filter $\boldsymbol{L}(q)$ can be modified to include a weighting operator for each point in the subset M. For this, a weighting matrix is defined as

$$\boldsymbol{W} = \text{diag}\Big\{ W_1,\ W_2,\ \cdots\ W_M \Big\}^\top. \tag{4.94}$$

To embed the weighting, the lifted operator $\boldsymbol{L}(q)$ (4.34) can be simply modified to,

$$\boldsymbol{L(q)} = \bar{\boldsymbol{L}}(\boldsymbol{q})\boldsymbol{W}\boldsymbol{\Phi}^*. \tag{4.95}$$

Applying the modified filter to the point-to-point RC update of (4.45), gives the weighted point-to-point RC update

$$\boldsymbol{u}(k+1) = \boldsymbol{u}(k) + \beta\big(\boldsymbol{\Phi P(q)}\big)^*\boldsymbol{W e}^{\Phi}(k). \tag{4.96}$$

A sufficient convergence condition is obtained for each point by replacing the unlifted learning rate condition (4.39) by

$$0 < \beta_j < \frac{1}{\sup_{\omega\in[0,\pi]}(|P(e^{j\omega})|^2)\max_j\,(W_j^2)}. \tag{4.97}$$

As with the previous updates, implementation requires the weighted point-to-point RC update (4.96) to be expressed in the equivalent unlifted form. This is simply

$$\begin{aligned} u((K+1)N+i) =& u(kN+i)+ \\ & \beta\Big(\sum_{j=1}^{\bar{i}} C_P A_P^{i-i_j} B_P W_j e((k+1)N+i_j)+ \\ & \qquad \sum_{j=\bar{i}+1}^{M} C_P A_P^{N+i_j-i} B_P W_j e(kN+i_j)\Big). \end{aligned} \tag{4.98}$$

With only a minor alteration to the point-to-point RC update (4.45), the learning rate of each point is now easily modified by the weighting operator, $\boldsymbol{W}$. This allows a designer to prioritise the convergence speed of specific points while decreasing the convergence speed of others to improve the local robustness. This could prove highly useful in dealing with disturbances that intermittently reoccur in some regions of a reference, such as during

the swing phase of gait. Additionally, although each weighting is depicted as a static value, they could be replaced by a dynamic function resulting in the weightings changing depending upon other parameters, e.g. error.

4.6 Summary

This chapter has presented the concept of point-to-point RC, as well as deriving implementable updates. To do this, derivations began with traditional RC, before 'lifted' systems were introduced. Section 3.3 highlighted the limitations of current control strategies for lower limb FES. Because of this, point-to-point RC has been designed to reduce the data being passed between cycles, improve accuracy by using an underlying model of the system (internal model principle) and utilise learning over each cycle to deal with time-varying disturbances (such as fatigue). It was also proven that all of the currently available learning algorithms used for traditional RC could be used with point-to-point RC, with minimal modification. This chapter has also presented two generalisations to the derived point-to-point repetitive controller. Filtered point-to-point RC substantially generalises the update to allow the designer to converge to any minimum norm solution (minimum velocity, acceleration, energy, jerk etc. norms) by adding a filter. Additionally, a simple modification to the learning filter resulted in weighted point-to-point RC. This enables a designer to have greater control over the convergence speed and robustness of individual points.

Chapter 5

Simulation

To validate the control framework of Chapter 4, it is now applied in simulation to the control of functional electrical stimulation for drop-foot. First, the electrically-stimulated dynamics need to be identified. The most recent model-based control approach (Seel et al., 2016) identified the dynamics as a third-order linear discrete transfer function via black box least-squares fitting. However, to produce a more general, transparent, model structure applicable to a broader range of users, a parametrised model is now developed to enable model-based design and simulation.

5.1 Model Parameters

The ankle has a complex structure, and a wide range of models have been proposed to capture underlying kinematic and kinetic properties. Depending on the application, complexity is reduced by grouping or omitting ligaments, and assuming isotropic, homogenous properties to muscle and cartilage (Ramlee et al., 2013). Similarly, tendons are typically modelled as tension-only elastic strings, bones are treated as rigid bodies, and effects caused by soft tissues are ignored (Fenfang et al., 2014). Accordingly, here we assume rigid body dorsiflexion/plantarflexion dynamics (L. Q. Zhang, 2000) with stiffness, damping and twitch response parameters extracted from data gathered through experimental motion and Electromyography (EMG) in Munih et al. (2000); Mesin et al. (2010); Ficanha et al. (2017); Rouse et al. (2013) using linear regression. This is combined with a Hill-type model of muscle dynamics (Sun et al., 2015), which has been shown to characterise both voluntary and artificial muscle activation accurately. The input is cascaded with the corresponding isometric recruitment curve (IRC) mapping the stimulation input to a static angular position, the linear activation dynamic (LAD), embedding the muscle delay response, and finally a function representing the rigid body dynamics (RBD) of the ankle. (Assalone et al., 2015) (Hammerstein structure). The

full model is shown in Figure 5.1. The dynamics of the resulting muscle model have been validated in Le et al. (2008).

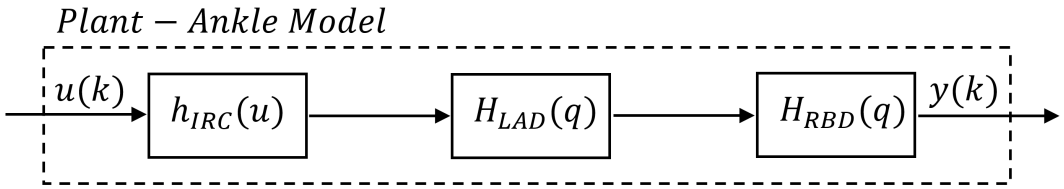

Figure 5.1: Model of artificially stimulated ankle dynamics.

5.2 Results

Although walking speed varies due to age, health and leg length, the average comfortable gait cycle is assumed to be 2 seconds. This is therefore used as the gait cycle period. The controller sampling and update time are set at 100 Hz as this is over 10 times the system bandwidth. The traditional repetitive control update of (4.4) is first simulated for the case of the gradient algorithm (4.38). For this set-up, it is necessary that the reference r is set to the full gait profile. Figure 5.2 shows the full gait cycle. The traditional

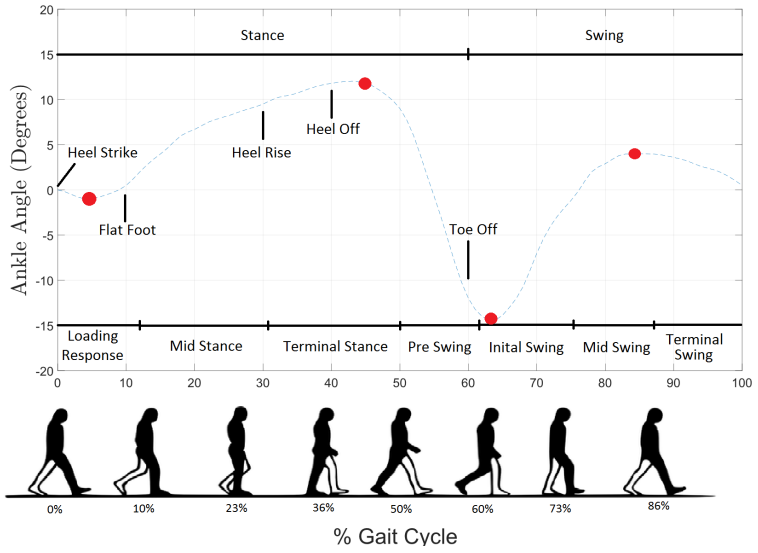

Figure 5.2: Standardised gait cycle, with gait events/phases labelled. The red dots correspond to the point-to-point tracking positions.

repetitive update is applied using $M = N = 200$, $i_1 = 1, i_2 = 2, \cdots, i_M = 200$. A range of β values are applied to establish maximum convergence, as can be seen in Figure 5.3. Whilst using the most successful gain value ($\beta = 7$), the error norm $||e||$ is slow, requiring 52 cycles (steps, 104 seconds of walking) to reduce the error norm convergence below 1% of its initial value. Faster convergence is not possible since divergence occurs with larger β, as illustrated with $\beta = 8$.

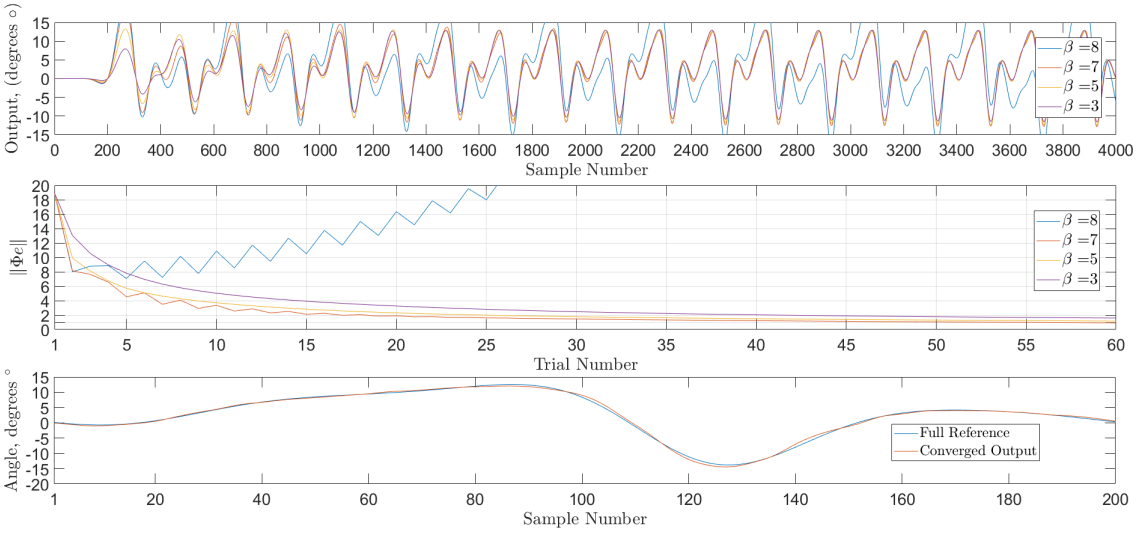

Figure 5.3: Traditional RC. Top: output evolution, middle: error norm convergence, bottom: solution converged to in 60 cycles.

Next the point-to-point RC (update (4.46) using the gradient algorithm (4.38)) is applied using $M = 4$. The set of point-to-point indices $\{i_j\}$ are defined using critical gait events, (sample i , angle $r(i_j)$) as: flat foot $(9, 0°)$, heel off $(44, 12°)$, toe off $(127, -14.5°)$ and start of mid-swing $(156, 1.629°)$. See Figure 5.2 for a graphical illustration of the selected point-to-point sample locations. Using the optimum β value ($\beta = 200$), which was found using the sufficient stability condition (4.39), the error norm $||\Phi e||$ falls below 1% of its initial value after 6 cycles. Increasing β further slows down convergence until divergence occurs, which can be observed in Figure 5.4. Additionally, the output behaviour between points is smooth, as expected by the minimum control effort property of Theorem 4.5.

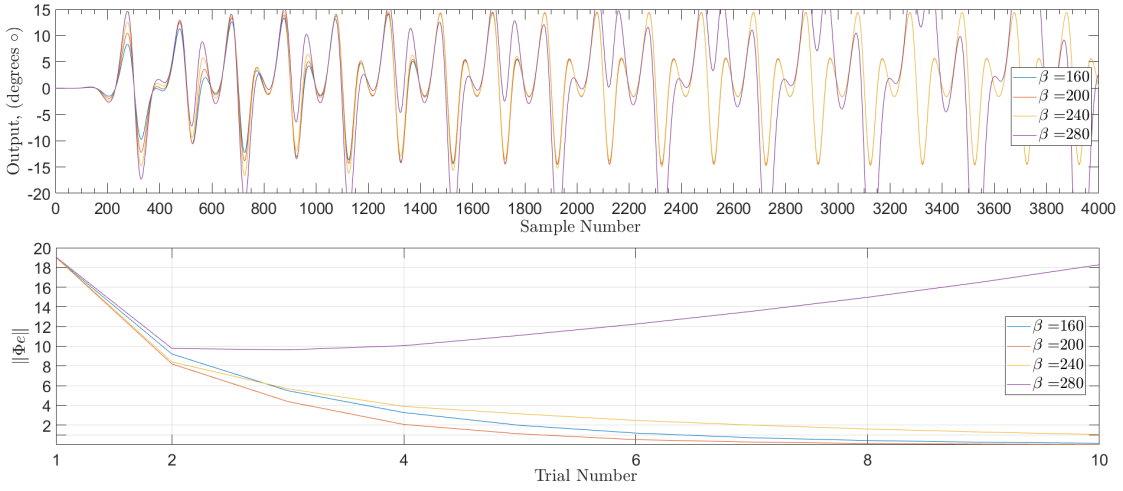

Figure 5.4: Point-to-point RC. Top: output evolution, bottom: error norm convergence.

Unlike the traditional repetitive control, point-to-point repetitive control will likely have a discrepancy between the reference and the points not extracted as part of the point-to-point reference. Figure 5.5.A) shows both the reference and the point-to-point RC output solution after 6 cycles. Figure 5.5.B.1) shows the difference in degrees and Figure 5.5.B.2) shows it as a percentage. When the reference tends to zero, the percentage error increases dramatically, resulting in the difference being a better way to establish the controller's performance. Figure 5.5.B.1) shows that the difference is reasonable across the entire signal, with a specific note of the small difference between sample 120 and 200, which corresponds to the swing phase of the reference. Figure 5.5.C.1-2) zooms onto the swing phase. Through the entire swing phase, there is only a difference of ± 2 degrees, resulting in a $+20\% - 40\%$ error. This is acceptable as the level of accuracy for a joint sensor across its operational range is typically ± 2 degrees. The similarity between output y and the full natural gait reference r also reflects that natural motion can be posed as a minimum control effort problem. This indicates that point-to-point RC can naturally assist motion.

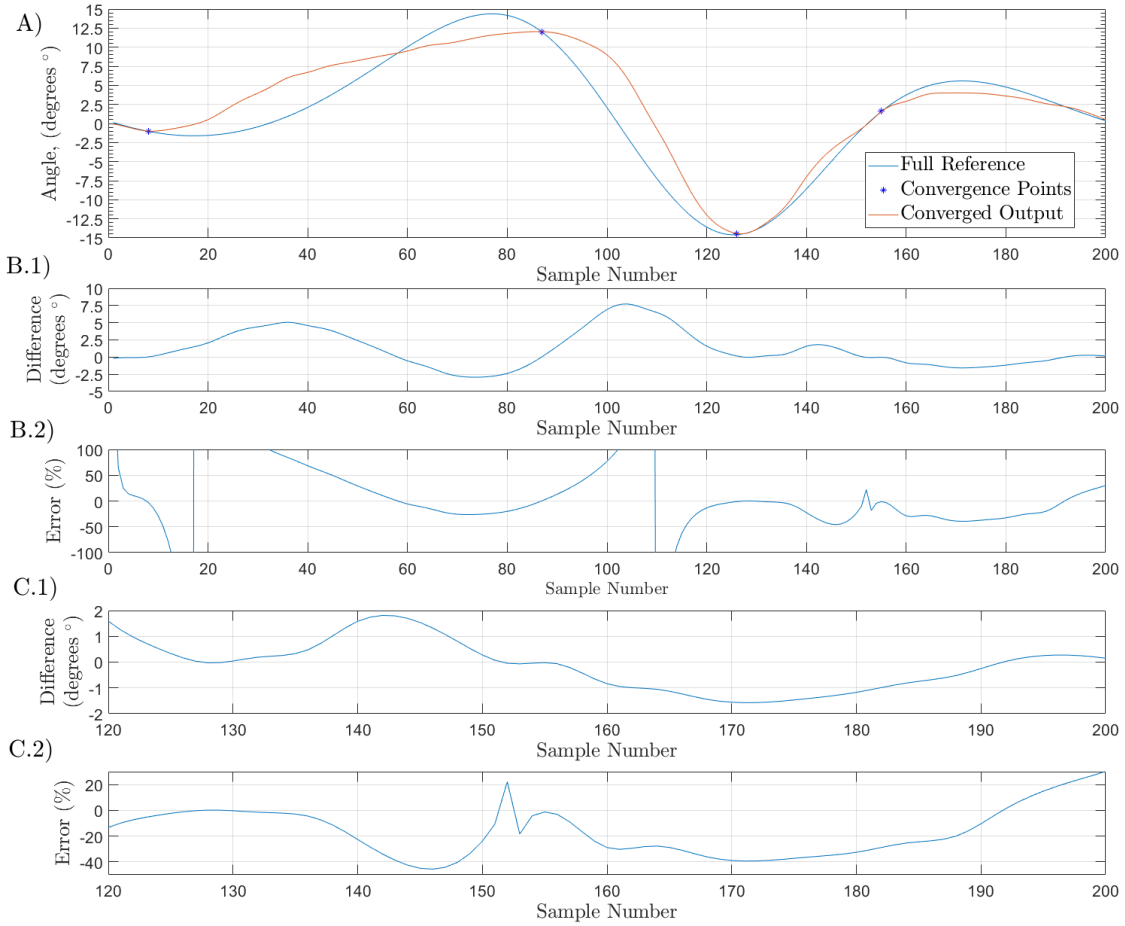

Figure 5.5: Point-to-point RC compared to the full reference signal.

Figure 5.6 shows what happens when the number of points is increased. Point-to-point RC is implemented with $M = 9$, sample indices $i = \{9, 34, 60, 83, 101, 127, 148, 172, 191\}$ and $\beta = 160$. The error norm $||\Phi e||$ falls below 1% within 33 cycles. The difference between the converged signal and the full reference is also shown to lie within ± 2 degrees for the entire signal, and almost always within ± 1 degree. Therefore, by increasing the number of tracked points (M), the output signal is better able to represent the entire reference. However, doing so will decrease the convergence speed and robustness.

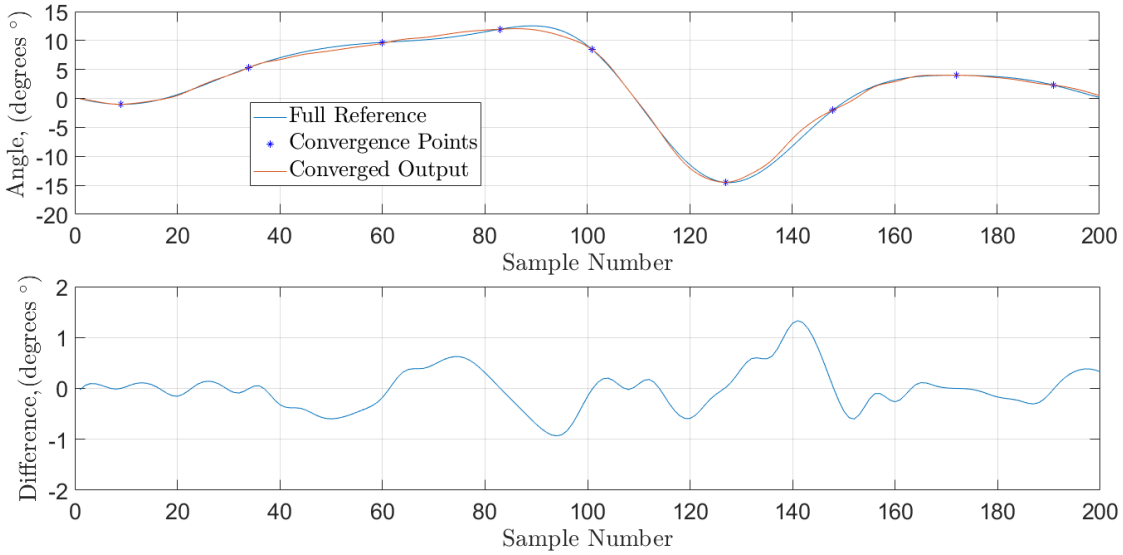

Figure 5.6: Point-to-point $M = 9$ implementation.

Table 5.1 summarises the key performance criteria between traditional and point-to-point repetitive control when applied to a gait reference. Point-to-point RC can converge faster and achieve perfect tracking for key gait positions. In contrast, traditional repetitive control takes longer to converge and is unable to achieve zero error norm for all the points it tracks. This is likely to be due to a discrepancy in the non-linear cancellation, resulting in oscillation being forced by the adjacent points. When comparing the point-to-point signal output to the full reference, point-to-point is less accurate when tracking small subsets (M), but can be improved by adding more points to the subset of the reference, using a different algorithm or applying a filter. It is also noted that for the swing phase, the output signal matches the reference well (point-to-point error norm 7.48, traditional error norm 4.34) for the minimum number of points ($M = 4$) needed to describe the reference.

Table 5.1: Error measures for traditional and point-to-point RC.

	Convergence (1%)	Difference Norm Across Full Gait	Difference Norm Across Swing Phase
Traditional Repetitive Control	52	6.06	4.3476
Point-to-Point (M=4) Repetitive Control	6	39.7837	7.4788
Point-to-Point (M=9) Repetitive Control	33	6.3349	5.1599

Having compared the controller's convergence speed and the accuracy of the output signals, the robustness of the control approaches are now considered. To aid comparison, a performance index (PI) is used, as first proposed by Ratcliffe et al. (2006). This is defined as

$$PI = \sum_{k=1}^{J} \|\boldsymbol{e}^{\Phi}(k)\| \tag{5.1}$$

with $J = 100$. The size of the performance index represents the total error accumulated during convergence. The smaller the value of PI, the quicker the convergence. To improve transparency in the comparison between traditional and point-to-point RC, only the error of the M points are used for error calculation in both, as extracted by the projection operator Φ.

The controllers have been designed based on the true model. To inspect robustness a percentage uncertainty has been applied to the orginal stiffness and damping coefficients used by the model. This ranges from 0% to 250% of those typical values. The values are based off the ones identified in Munih et al. (2000); Mesin et al. (2010); Ficanha et al. (2017); Rouse et al. (2013). The learning rates, β, are reduced to 80% of their original values. Results are shown in Figure 5.7. The results highlight that point-to-point has a smaller PI value for larger damping/lower stiffness values and a larger value for lower damping/higher stiffness values. This also results in a smaller PI value around the designed operating parameters (denoted by the pink dot on the 100% stiffness and damping value intersection) showing improved robustness characteristics. Additionally, the average PI across the $\pm 50\%$ region (pink box) is found, traditional $PI = 415.4794$ and point-to-point $PI = 97.8757$, indicating point-to-point also converges faster across the entire region. By adding more tracked points, the robustness of the controller can be seen to reduce. For $M = 9$ the controller is less robust compared to $M = 4$, see Figure 5.7. Although the colour plot is slightly misleading, the robustness for $M = 9$ is still better than traditional RC as the $\pm 50\%$ region has a value of $PI = 262.8966$.

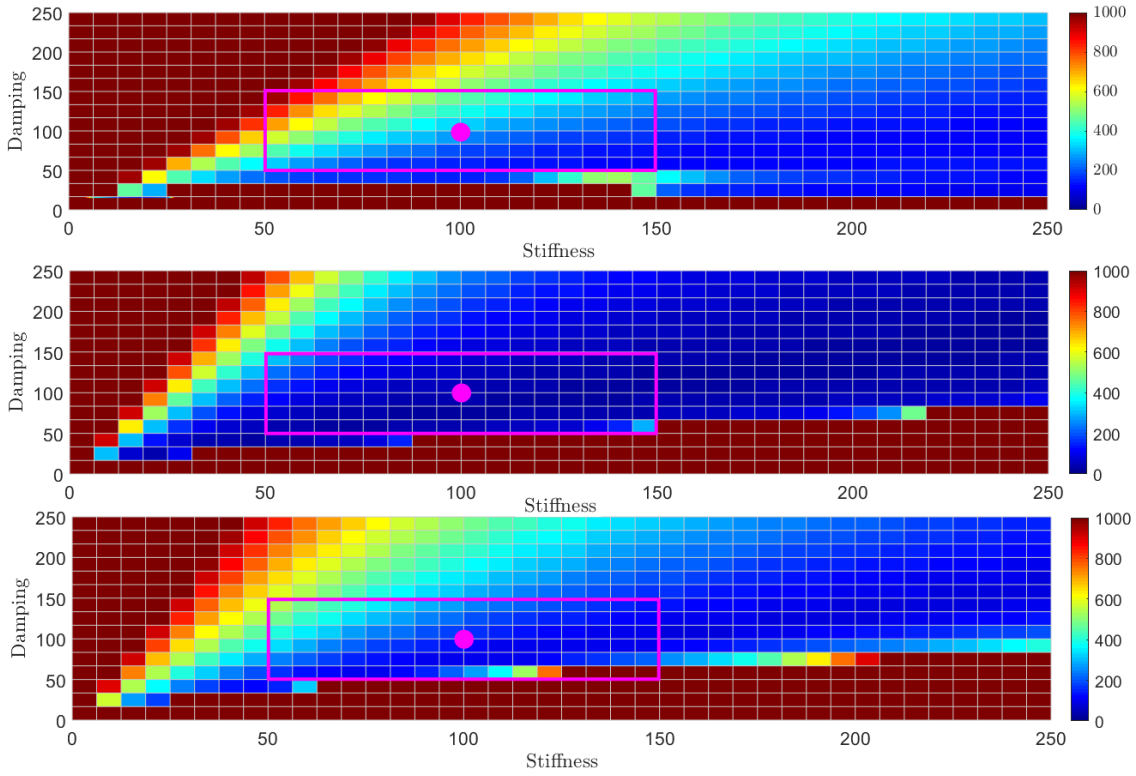

Figure 5.7: Robustness: traditional, point-to-point ($M = 4$), point-to-point ($M = 9$).

5.2.1 Minimum Energy Filter

To change the converged input solution, a filter F is next applied using the framework in Section 4.4 and RC update form (4.86). A 6th order low pass butter-worth filter was designed with a 15 Hz frequency cut-off and a filter length of $n_f = 40$ to satisfy the causality condition (4.68) and the filtered minimum control effort condition (4.70).

To confirm that the minimum control energy solution u^* has been achieved, the filtered update can be compared to the minimum Euclidean norm solution (given by (4.75)). By applying the designed filter, the minimum control energy solution to the problem can be observed to have been achieved (Figure 5.8).

Although the output converges to the minimum jerk solution, the minimum energy and minimum jerk solutions are very similar. This is due to the large space between points. To better observe the effect of the filter, a more constrained reference is required. By increasing the tracked subset to $M = 8$ (using the same positions as the previous $M = 9$ without i_3) the filter (n_f) can be applied again, but now needs to be redesigned for the new system. A 2^{nd} order low pass butter-worth filter is designed with a 40hz frequency cut off, filter length of $n_f = 10$, producing Figure 5.9. In this case, the filtered signal difference norms improve when compared to point-to-point RC, specifically between

sample 40 and 90. Although the filtered point-to-point RC produces a better error norm for the full reference (no filter, 9.9531 filter, 8.9244), the error norm increases slightly for the swing phase of the gait cycle (sample 120 - 200, no filter, 5.4450 filter, 6.2904). This limits the usefulness of the filter as this is the key region of operation.

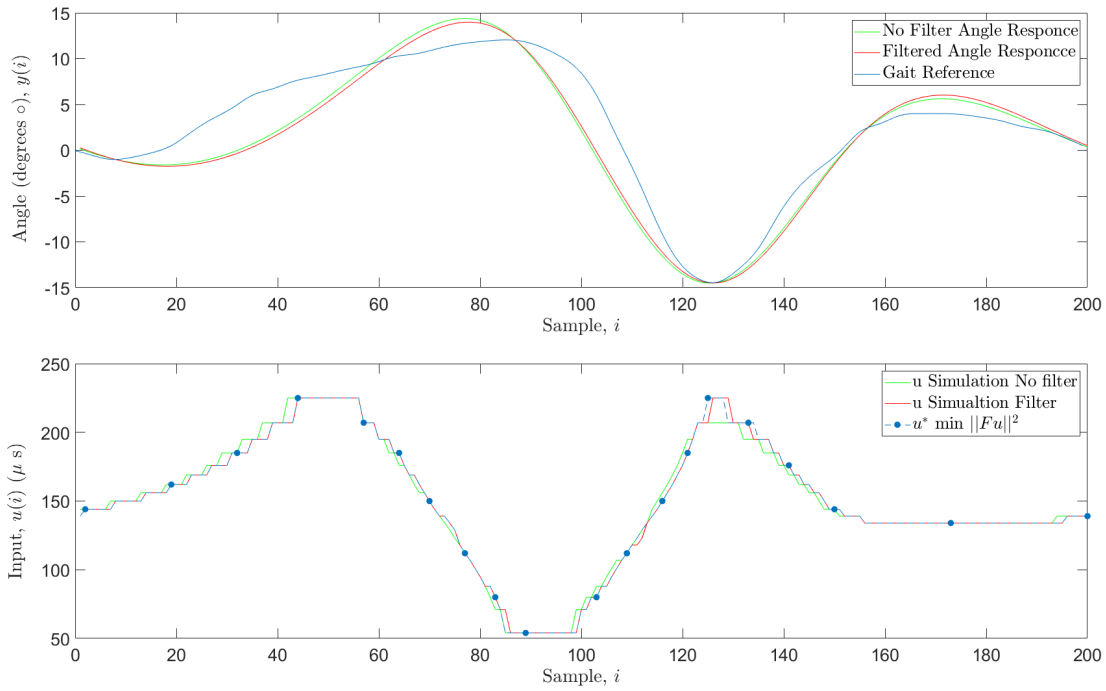

Figure 5.8: Minimum jerk filter, input, output signal.

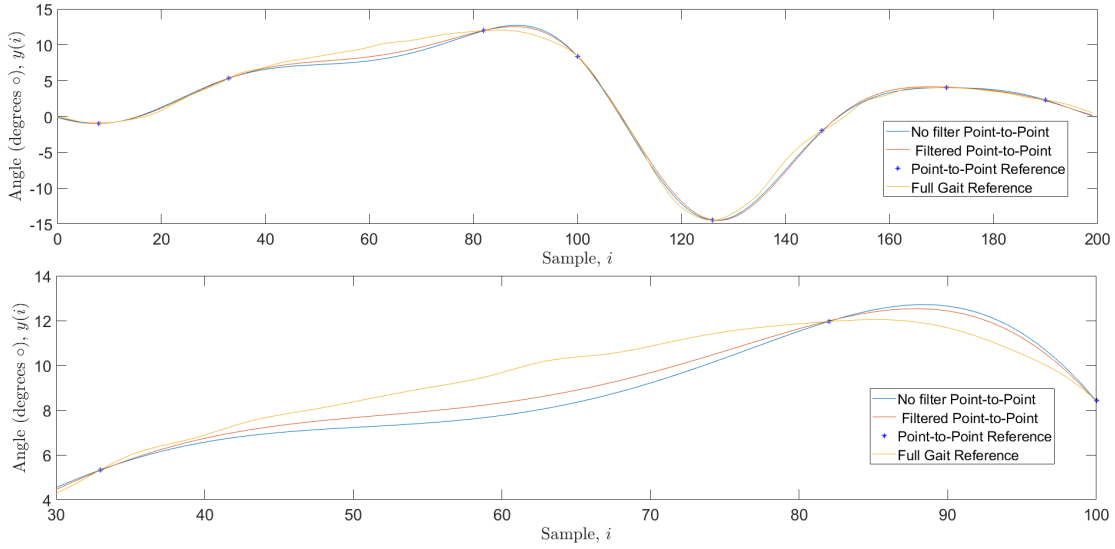

Figure 5.9: Effect of filter. Top: full signal, bottom: samples 40 to 90.

5.2.2 Weighted Point-to-Point Repetitive Control

Next, the weighting approach described in Section 4.5 is implemented. This modification to the point-to-point control framework allows the designer to allocate different levels of priority to each point effectively. This is achieved by altering the learning rate, β, with a weighting, W for each point within the extracted point-to-point reference.

Figure 5.10 shows that altering the weight given to a single point can allow a divergent system to converge. However, the further the point is away from the unstable point, the less effect it has. This is shown in Figure 5.10.A.2), A.3) and A.4), and the corresponding convergence of all the points is shown in B.1).

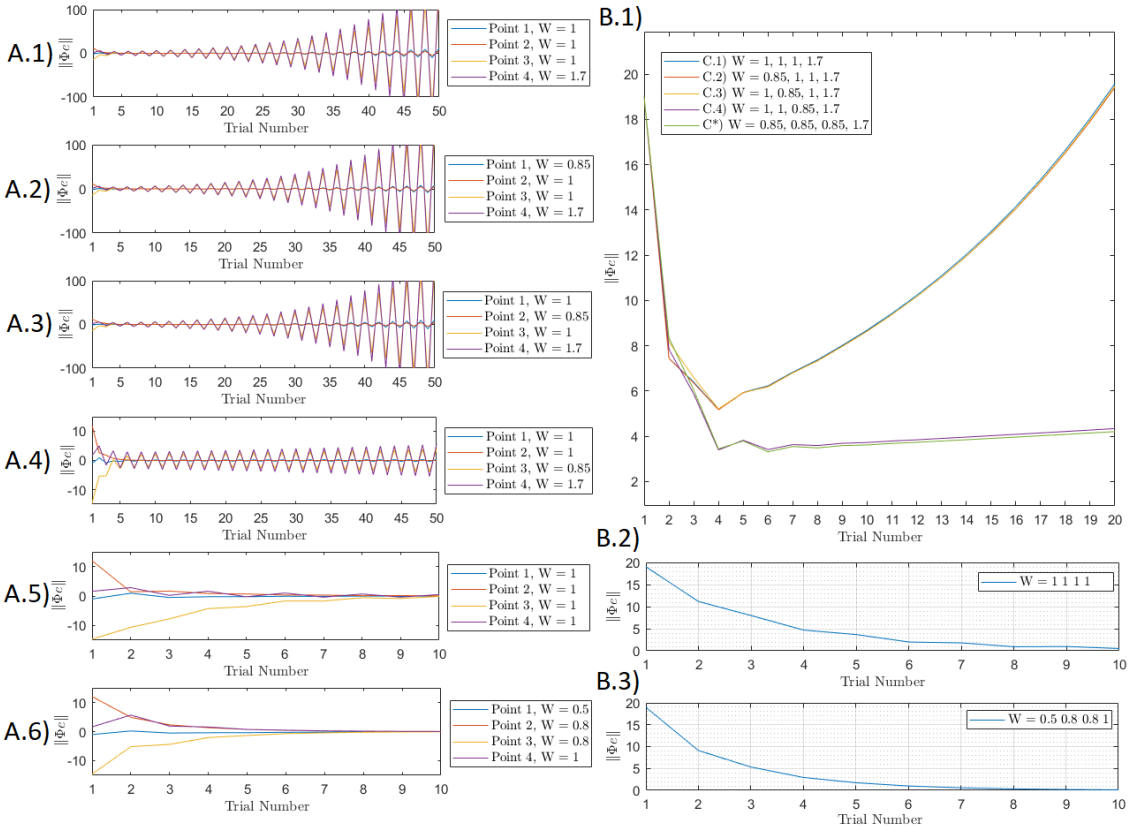

Figure 5.10: Weighted point-to-point; effect of relaxing priority on convergence.

This enables the designer to specify the error evolution of each point from cycle to cycle. Because the norm of a signal considers all points, its convergence is limited by the slowest converging point. By suitable design, the error evolution of each point can be modified such that they all converge at the same time. Observing Figure 5.10.A.5), point 3 takes much longer to converge than the other points, and point 1 converges much quicker. By altering the weightings, all points can be made to converge based on the slowest points convergence speed, see Figure 5.10.A.6). Figure 5.10.B.2) and B.3) show that even with the lower weightings, $W = \{0.5, 0.8, 0.8, 1\}$, they both achieve the 1% error norm within

6 cycles. Therefore, convergence speed has been reduced on specific points to increase robustness with negligible effect to the overall convergence.

By applying the PI factor, the robustness of point-to-point to a weighted point-to-point can be compared. Figure 5.11 shows a larger robust region for the weighted framework. The $\pm 50\%$ PI region average is slightly larger (at $PI = 115$) for weighted point-to-point RC. This is because of the increased robustness results in slower convergence around the ideal model. In this case, relaxing the weightings is not needed, as it already has a large stability region. However, it may be required for cases in which the stability region was small or an increase in robustness at the expense of convergence speed is desirable.

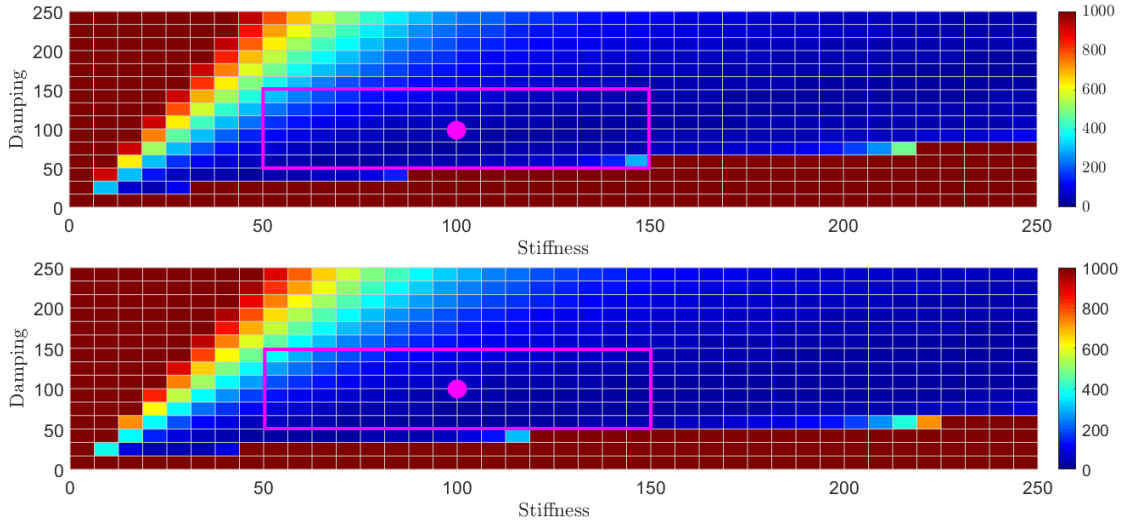

Figure 5.11: Robustness: point-to-point vs weighted point-to-point.

This can be extended further by considering dynamic weights. This can be easily achieved through a range of different algorithms. Here a dynamic weighting is based on the error of each point and then normalised with the maximum error and constrained by a minimum value,

$$W_i = \|(e(i) + 0.2 \times e(i)/\max(e(i))\|, \tag{5.2}$$

$$\textbf{if } (W_i > 1) \textbf{ then } W_i = 1, \tag{5.3}$$

$$\textbf{if } (W_i < 0.3) \textbf{ then } W_i = 0.3.$$

where W_i is the weighting being applied to the i^{th} point.

Figure 5.12.A.1) shows the convergence of point-to-point (unity weight) and 5.12.A.2) shows the dynamic weighted point-to-point, which achieved a very similar convergence, again 1% error norm with 6 cycles. However, the main reason for making the weighting dynamic would be to help deal with disturbances that occur. A step disturbance of 10 degrees is applied across all points during the 15^{th} cycle. The 15^{th} cycle has been selected to first allow steady-state conditions to occur. Comparing Figure 5.12.B.1

(point-to-point) and Figure 5.12.B.2) (dynamic weighted point-to-point), the dynamic solution is shown to limit the max error and reduce the error norm quicker than the un-weighted approach.

Figure 5.13 shows the effect of a dynamic weighting on robustness. Specifically, the dynamic weighted point-to-point is found to be less robust to model uncertainty overall due to the occurrence of divergent clusters. An investigation into other dynamic weights could resolve this issue.

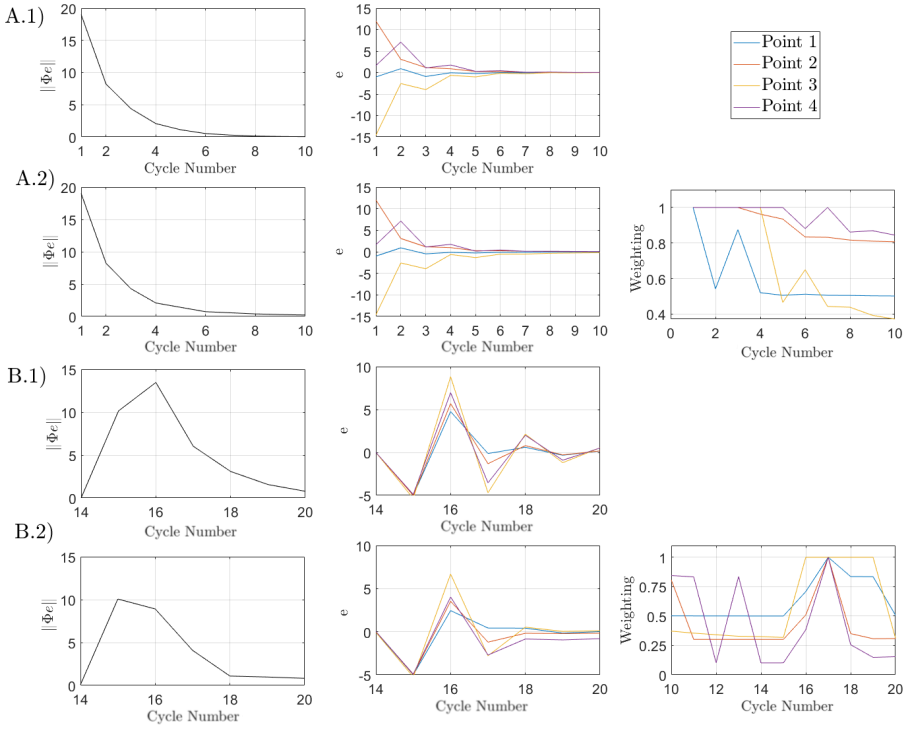

Figure 5.12: Comparing point-to-point RC to dynamic weighted point-to-point RC, convergence and response to disturbance.

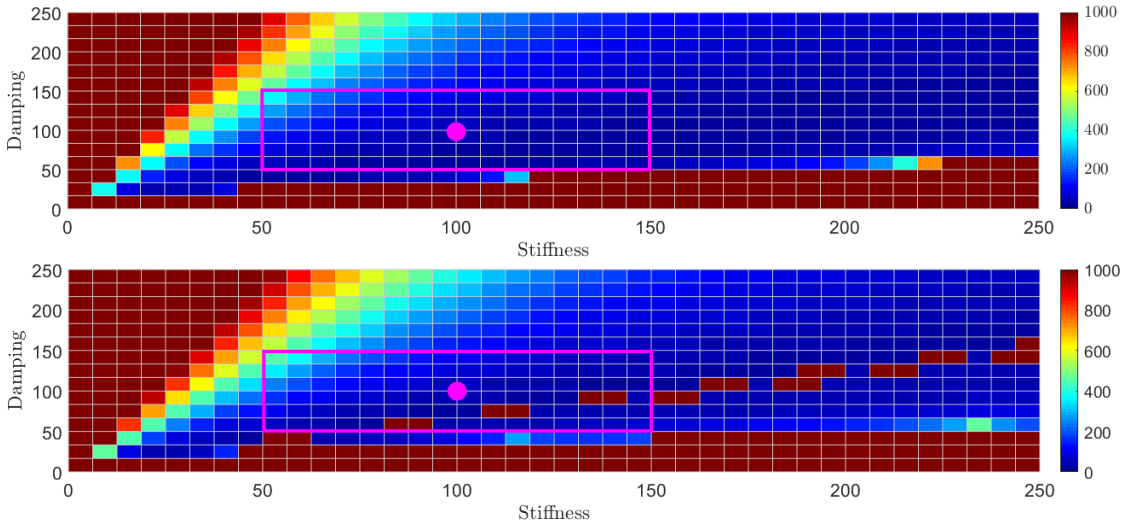

Figure 5.13: Robustness, weighted vs dynamic weighting.

5.3 Summary

Comparing simulations of the point-to-point and traditional RC updates show that point-to-point RC achieves faster convergence (point-to-point 6 cycles, traditional 52 cycles) and an improved robustness region (point-to-point $PI = 97.88$, traditional $PI = 415.48$). This was achieved while only tracking the swing phase slightly worse than traditional RC (point-to-point error norm 7.48, traditional error norm 4.35). However, point-to-point RC achieved all the above with only $\frac{1}{50}$ of the data points traditional RC used, stored and passed between cycles. Further simulations have explored the minimum control effort generalisation and weighting modification. The generalisation of the minimum control effort has shown that the minimum jerk solution can be converged to rather than the minimum energy solution. In this particular application, the minimum energy and minimum jerk are very similar, and so this had a limited effect. Additionally, the simple modification to allow each point to have a weighting gave the designer greater control, specifically allowing them to increase robustness for a specific model without reducing convergence speed.

Table 5.2: Simulation comparison table showing the performance of tradtional and point-to-point RC

	Convergence (1%) *only key points	Robustness Region Value (50%) [Average] *after 75 trials	Difference Norm Full Gait *at 1% norm	Difference Norm Swing Phase *at 1% Norm
Traditional RC	52	2.6175×10^4 [415.4794]	6.06	4.3476
Point-to-Point RC ($M = 4$)	6	6.1662×10^3 [97.8757]	39.7837	7.4788
Point-to-Point RC ($M = 9$)	33	1.6825×10^4 [262.8966]	6.3349	5.1599
Filtered Point-to-Point RC ($M = 4$)	6	6.402×10^3 [101.6324]	39.1043	9.3987
Point-to-Point RC ($M = 8$)	30	1.6154×10^4 [252.4080]	9.9531	5.4450
Filtered Point-to-Point RC ($M = 8$)	48	2.0751×10^4 [324.2353]	8.9244	6.2904
Weighted Point-to- Point RC ($M = 4$)	6	7.3065×10^3 [115]	39.7837	7.4788
Dynamic Weighted Point-to-Point RC ($M = 4$)	6	8.7136×10^6 [1.3831×10^5] *six divergent cells	38.5806	6.7853

Chapter 6

Experimental Evaluation

The performance of the traditional and point-to-point RC updates derived in Chapter 4 are now investigated in human feasibility trials to evaluate their effectiveness. This builds upon the initial simulation validations performed in Chapter 5 by including the full complexity of stimulated muscle dynamics, model uncertainty and the presence of involuntary motion. The chapter begins by motivating the type of electrode technology used and its associated hardware. It then considers the identification procedure required to generate a suitable model before presenting the experimental findings.

6.1 System Structure

Subsection 2.3.2 found that the majority of current FES systems employ non-invasive transcutaneous electrode pads. This resulted in the principal reason for patients discontinuing FES being due to challenging pad placement (Taylor et al., 1999). It also concluded that commercial FES systems commonly use a small number of large surface pads. These reduce selectivity and fine movement control and lead to increased rates of fatigue (Li-Wei and Binder-Macleod, 2007). Subsection 2.3.3 found that the emergence of surface electrode array technology enabled a higher degree of muscle selectivity (Lyons et al., 2004) and also helped to address the pad placement problem.

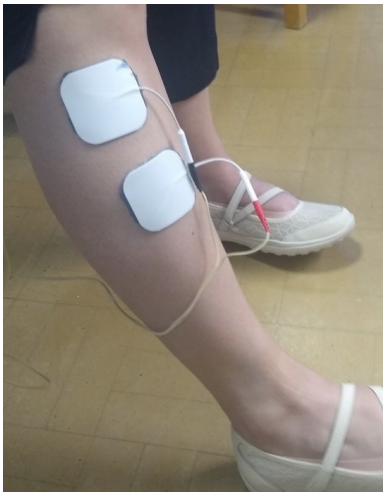

Figure 6.1: Example of transcutaneous pad placement.

Electrode arrays embed a number of electrode pads in a predefined layout. Each electrode pad can be individually activated to find the best stimulation location without

removing and re-applying pads. There are two types of designs: the first has pads which are shaped to correspond to muscle positions, e.g. HandNMES (Snoek et al., 2000) and H200 Bioness. However, a mismatch between the muscle and pads can limit their effectiveness (Crema et al., 2018) or require a bespoke layout for every user. The second type employs a grid layout which allows a broader application to different limbs and users, e.g. INTFES (Velik et al., 2011) and ShefStim (Kenney et al., 2016).

The above summary motivates using an electrode array with pads arranged in a grid layout for experimental controller testing. This requires a corresponding plant model. Previously Figure 5.1 provided a block model diagram of the ankle system stimulated with a single pad. It is now necessary to expand the model to match the use of an array. This is done schematically in Figure 6.2, which now includes the various pads within an electrode array. Now, the stimulation input $u(k)$ can be switched between numerous electrode pads and so activate different muscles. The input is again cascaded with the corresponding isometric recruitment curve (IRC), linear activation dynamic (LAD) of the activated muscles, and the rigid body dynamics (RBD) of the ankle.

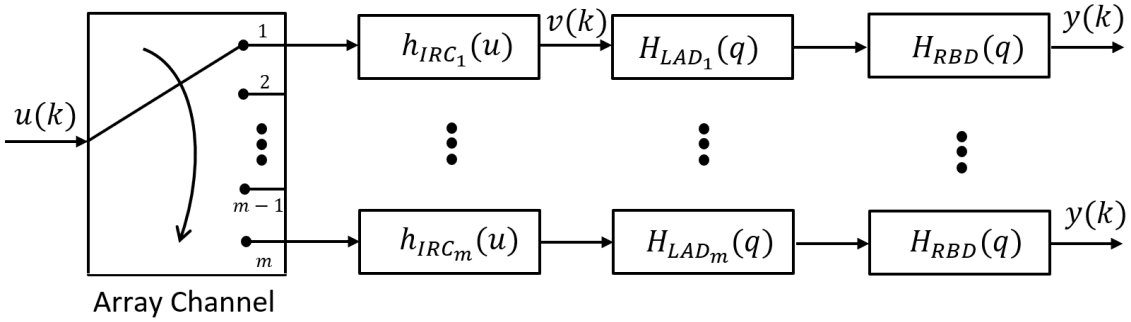

Figure 6.2: Model block structure of array-based FES using a single stimulation site.

The experimental hardware needed for the first human application of RC to drop-foot is now introduced.

6.1.1 Hardware

Figure 6.3 shows the hardware block diagram for the stimulator, including connections and the flow of information. The stimulator has been designed to support the chosen 24 pad array, as 24 pads have been shown by Yang et al. (2014b) and Yang et al. (2018) to be sufficient in covering a region so that input pads which support accurate limb gestures can be found. To implement the control scheme, a myRIO (Model 1900, National Instruments, USA) microprocessor is selected because of its field-programmable gate array (FPGA) capabilities. The FPGA allows for 24 input/output pins to be configured as PWM outputs. This allows the intensity of each stimulation channel to be independently controllable in real-time while having sufficient resolution to enable precise

movements to be achieved. Although a single channel could supply all 24 pads, later in Chapter 7 multiple pads with varying levels will be required for multi-pad patterns. The PWM takes the form of a general monophasic waveform to simplify the hardware system. The pulse rate (frequency) is fixed to the commonly used rate of 40Hz (Wederich et al., 2000). The PWM is amplified by a DC-to-DC converter, which has a current limit of 140mA. The converter increases the voltage from 5 volts to between 50V and 120V volts to excite muscle contraction. The exact level depends on user comfort. The circuitry has been designed based on the work reported in Ilic et al. (1994). Each PWM signal supplies a single electrode pad.

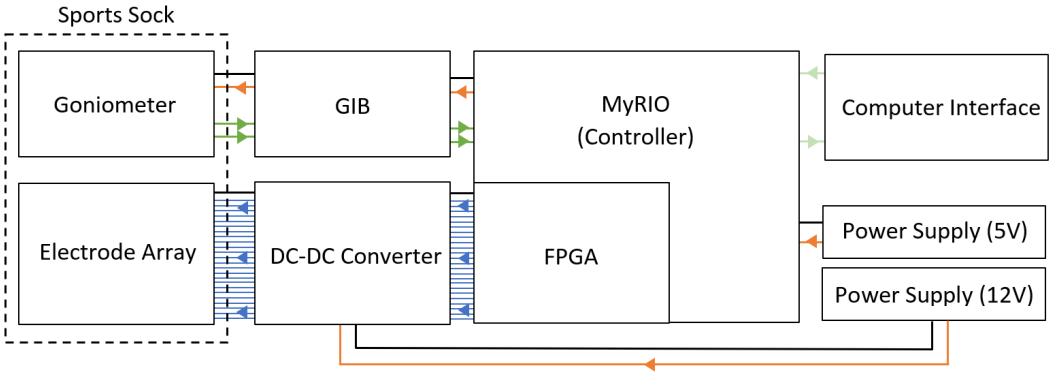

Figure 6.3: Experimental hardware configuration displayed as a block diagram.

To keep the electrode-tissue interface within a safe electrochemical region and thereby ensure user comfort, the stimulator implements a constant current output for each electrode of approximately 20mA (Kesar et al., 2008). For safe use during experiments, additional protection has been added to the stimulator. In particular: (1) the power supplies are electrically isolated from the remaining circuity, preventing any unwanted return path from the array elements, (2) minimum, and maximum constraints ($0 \leq u \leq 300$) are imposed on the duty cycle within the software and (3) the researcher and participant both have emergency switches to turn off the stimulator power supplies instantly, for any reason.

As described, an array with a grid-based layout will be used. However, most such arrays like ShefStim, use conventional polycarbonate electrode pads which are not breathable or comfortable (Neuman, 2000). To negate these issues, a 24 channel fabric-based printed electrode array, validated in (Yang et al., 2014a, 2018), was selected for this research. The electrode array was placed freely on the shank so that the peroneal nerve was covered. The aforementioned electrode array uses dry electrodes rather than the usual wet hydrogel electrode. This makes it ideal for integrating into clothing as the electrode does not stick during donning and doffing. A goniometer (Biometrics Ltd.) was used to measure the angular rotation (roll and pitch) around the ankle joint. Both the electrode array and goniometer are embedded into a sports sock, pictured in Figure 6.4, ensuring contact and flexibility around the joint. The output signal from the goniometer is interpreted by a goniometer interface box (GIB). The GIB then produces two-variable

voltages (one for each degree of freedom) which can be read by the analogue read pins of the myRIO. The controller then uses the dorsiflexion value to update the next cycle. The goniometer has an accuracy of $\pm 2°$ and repeatability of $1°$; both are validated across a range of $90°$.

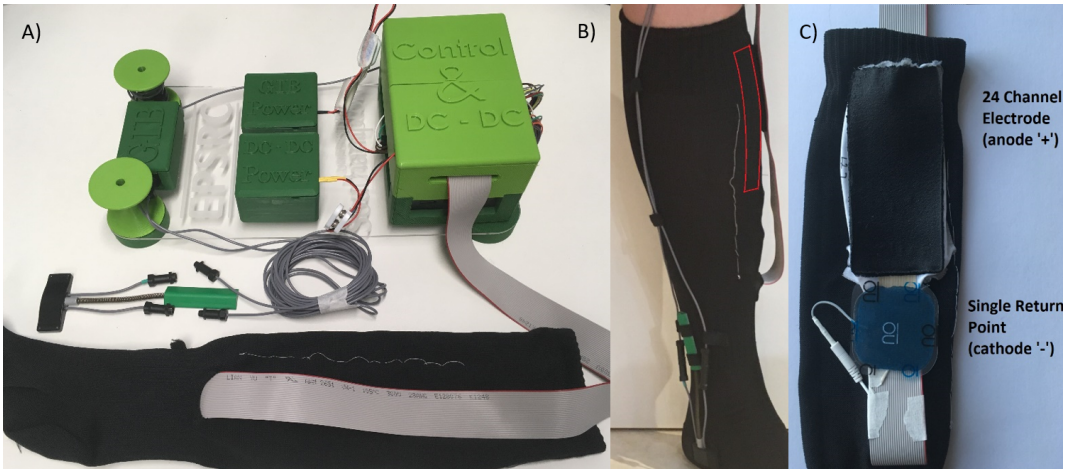

Figure 6.4: Images of hardware, A) full system, B) FES sock being worn, C) FES sock inside out, revealing the electrode array.

To select a suitable pad, the same general approach, to those reviewed in Section 2.3.3 will be adopted. This involves selecting a single stimulation site at the beginning of the experiment and using it throughout the experiments. The chosen procedure is described in the next section.

6.2 Model Identification

The conventional approach to electrode array pad selection first introduced in Section 2.3.3 is undertaken (e.g. (Schill et al., 2009; O'Dwyer et al., 2006; Micera et al., 2010; Popović-Bijeli et al., 2005; Prenton et al., 2014)). This conventional approach searches for a single stimulation pad by stimulating each pad within the electrode array individually with a predefined stimulation signal $u(k)$. The pad which provides the most desirable response is then chosen. A more detailed review of the criteria used to select a pad location will be undertaken in Chapter 7 when multiple pad patterns are considered.

Here, the active pad is controlled by the switching action of the array channel, as depicted in Figure 6.2. The angular responses $y(k)$ are recorded. The pad with the most desirable output, maximising dorsiflexion and minimising roll, is selected as the input using the same cost function as in Prenton et al. (2014).

Once an input pad is located, the corresponding dynamics for that input needs to be identified. For example, if channel i is selected the model is $y(k) = H_{RBD}(q)H_{LAD_i}(q)h_{IRC_i}(u(k))$. There are a variety of approaches to identify this Hammerstein form. However, few are

suitable for use with patients. The approach with the most success at identifying the IRC is termed the ramp deconvolution method. It has been shown to have high accuracy with relatively short computation time when compared to other identification methods (Durfee and MacLean, 1989; Durfee and Palmer, 1994). This approach depends on the assumption that the linear activation dynamic can be approximated by a pure time delay, allowing the non-linear and linear dynamics to be deconvolved easily by time-shifting. This is done by applying a slowly ascending and descending input signal, as described in Le et al. (2010). An example of the slow triangular input, $u(k)$, is shown in Figure 6.5.A). The slow input approximates steady-state dynamics, so as to not excite the LAD and RBD components. Next, the input and output peaks are lined up by cross-correlating.

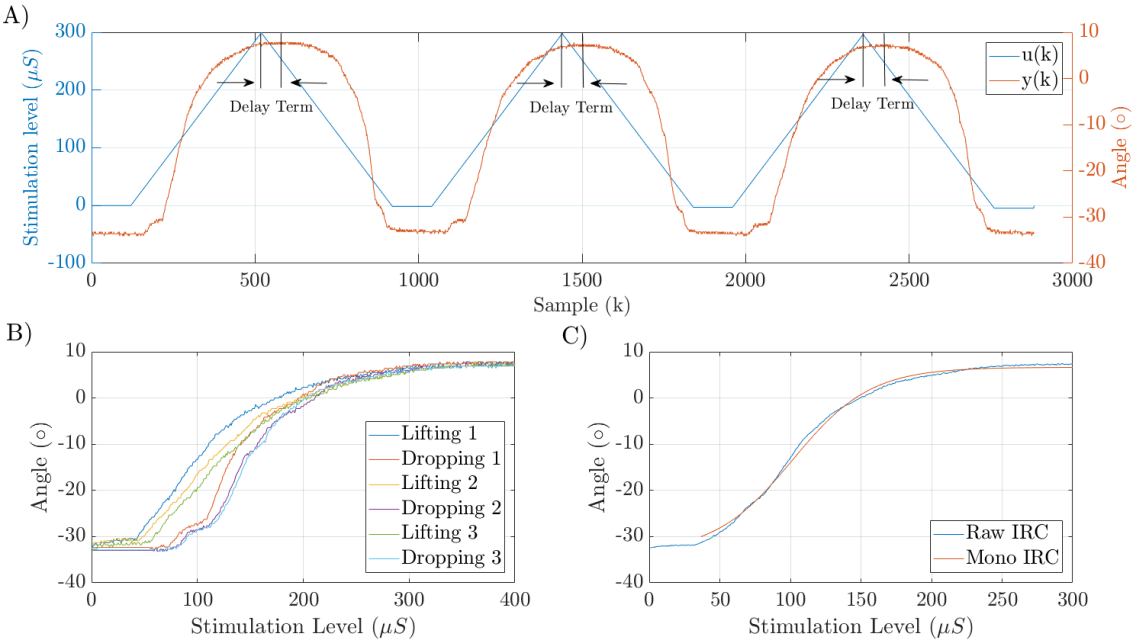

Figure 6.5: Representative IRC identification graphs.

The value of the time shift is found by considering the turning points, $\frac{dy}{dt} = 0$, of the input and output signals. By plotting the output against the input, the shape of the isometric recruitment curve is obtained. Since the input signal is triangular, when the output is plotted against the input, two similar plots corresponding to the lifting and dropping of the foot emerge, forming a loop. These will overlap perfectly for a pure time delay. An example using experimental data is shown in Figure 6.5.B) for several triangular inputs. These are averaged to give a single plot describing muscle recruitment (raw IRC). Finally, to ensure a suitable IRC, a parameterised form is used. This is done by fitting the parameters to the raw data, giving a suitable approximation of the isometric recruitment curve, h_{IRC}. Figure 6.5.C) shows the raw and parameterised (monotonic) IRC signals. The isometric recruitment curve previously used in Freeman et al. (2009)

has been chosen and has the form

$$h_{IRC}(u) = \alpha_1 \frac{e^{\alpha_2 u} - 1}{e^{\alpha_2 u} + \alpha_3}, \quad u_0 \leq u \leq u_{max} \tag{6.1}$$

with unknown parameters α_1, α_2 and α_3. The lower and upper limits (u_0 and u_{max}, respectively) on the pulse-width input, u, are used to prevent over-stimulation and ensure comfortable usage. The values selected in this research are $u_0 = 0$ and $u_{max} = 300$. The parameterised form is also monotonic. This allows it to be inverted and used to cancel the non-linearity, as shown in Figure 6.6. This, therefore, makes the system linear and also means the linear dynamics can be better approximated. This is described next.

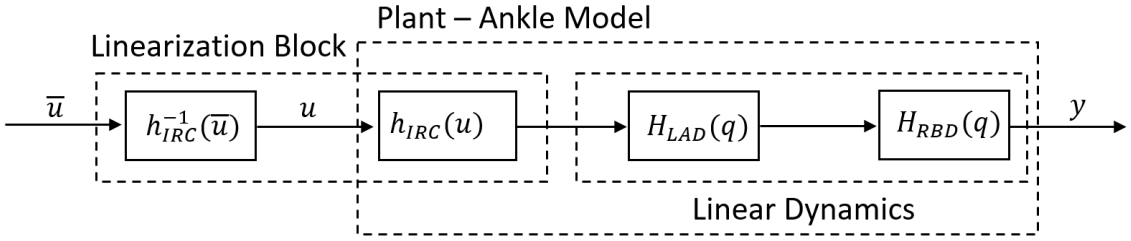

Figure 6.6: Model block diagram of linearised dynamics .

Now the non-linear form h_{IRC} has been identified, the pure delay assumption for the linear dynamics can be revised. For FES systems, the linear activation dynamics, h_{LAD}, are generally assumed to take the form of a critically-damped second-order system (Durfee and MacLean, 1989). However, because the angle is the controlled parameter, this form does not include rigid body dynamics, h_{RBD}. Instead, a 4th order black-box identification approach is used. A suitably exciting reference, $\bar{u}$, has been shown to be a set of steady-state angular step inputs (degrees) (Le et al., 2009, 2010). This is transformed into a stimulation signal, u, using the inversed isometric recruitment curve, i.e. $\bar{u} = h_{IRC}^{-1}(u)$, cancelling the non-linearity. Black-box identification then fits a model of the dynamics between the input, $\bar{u}$, and output, y. The linear dynamics are estimated using the Matlab 'SSEST' function, which uses prediction error minimisation algorithms and expresses the resultant model with state-space parameters.

Figure 6.7.A) shows a representative input $\bar{u}$, output $y(k)$ and the model-based predicted output, which achieved a model fit of 69.5%. Here, the same data used for the model was used for fitting. Figure 6.7.B) and C) show the model's step and impulse responses, respectively. In this representative example, the step response has a rise time of 1.03 seconds, while the impulse response has a settling time of 1.69 seconds. Both values are within the gait cycle time (2 seconds), and consequently, the internal model of the system captures the full dynamic response to an applied stimulus within the convolution window. This also means the causality condition given by equation (4.40) does not result in a loss of model accuracy as the model has settled. To maximise model accuracy, the model is identified at the beginning of each new experiment session.

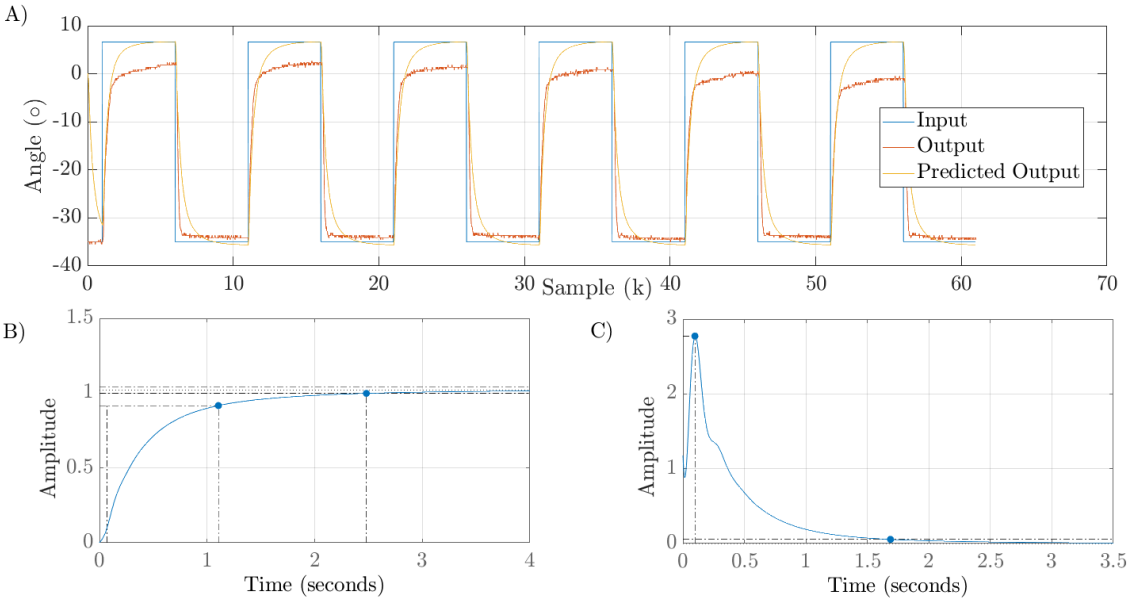

Figure 6.7: A) input/output data and model-predicted response, B) model step response, C) model impulse response.

6.3 Experimental Validation and Evaluation

Before the experimental results are presented, the tracked reference is re-introduced.

6.3.1 Gait Cycle

Section 2.2 first introduced the gait cycle. It was shown that the gait cycle is commonly split into stance (0% - 60% of motion) and swing (60% - 100% of motion) and can then be further partitioned into 8 distinct sections (Zhang et al., 2012). By amalgamating experimental results from Postans and Granat (2005) and Neptune and Sasaki (2005), a full human gait cycle was produced and used as the reference, r, for the simulations in Section 5.2. The same full reference is used here. A gait cycle is assumed to last 2 seconds, a sampling rate of 40Hz, results in $N = 80$ points. Section 5.2 focused on the point-to-point RC implementation using $M = 4$. The following experiments add an additional point ($M = 5$). The additional point was added close to heel rise, as the real system was found to droop. The $M = 5$ tracked points are shown in Figure 6.8 and are

$$i_1 = 5\%N, i_2 = 25\%N, i_3 = 45\%N, i_4 = 63\%N, i_5 = 84\%N. \tag{6.2}$$

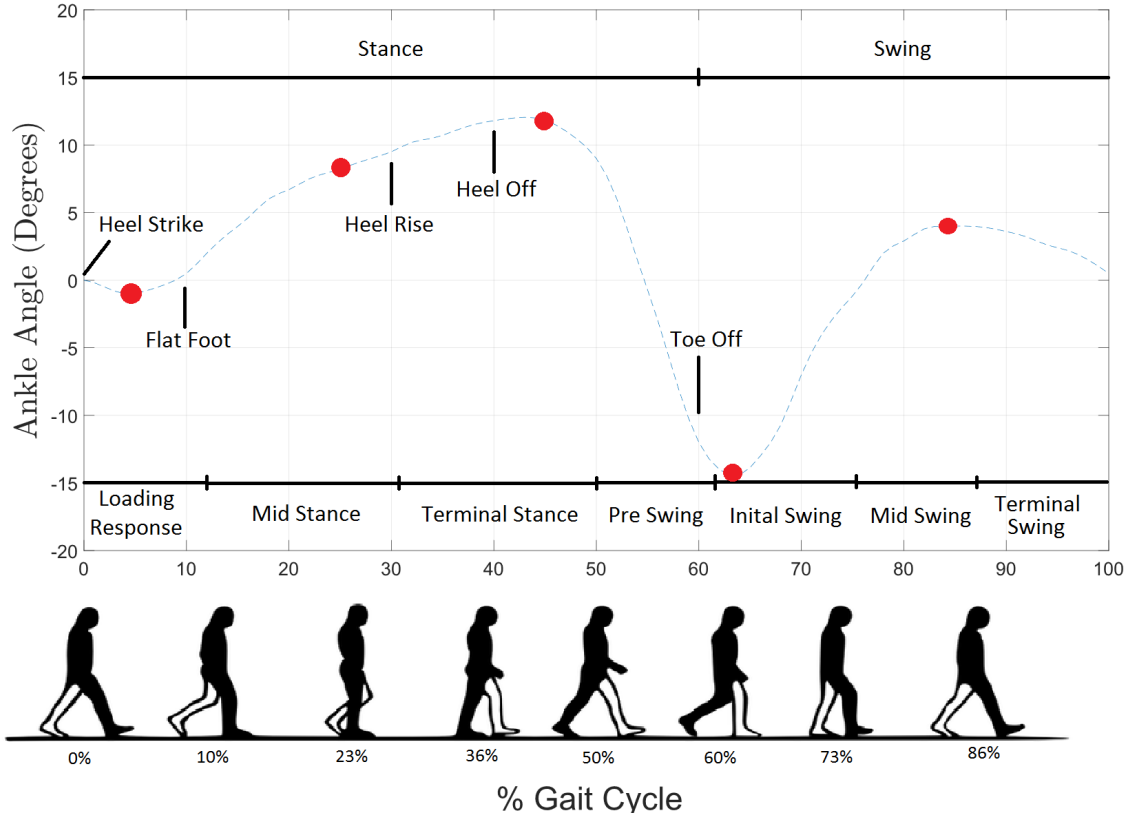

Figure 6.8: Gait cycle, with gait events/phases labelled. The red dots correspond to the point-to-point tracking positions.

6.3.2 Methodology

Experimental trials with healthy individuals were undertaken to evaluate the effectiveness of the designed RC schemes. Following ethical approval (ERGO/FPSE/47517), five unimpaired participants were recruited for this study. Participants 1 and 5 had experienced/partaken in FES studies before, while participants 2, 3 and 4 had not. The participants were asked to sit on an elevated stool, thus leaving the leg able to swing freely.

At the beginning of each experiment, the voltage was tuned to be within the participant's comfort region. This was done by slowly increasing the voltage level of the PWM (with the maximum pulse width length applied) until a sufficient range of motion is achieved or when the participant finds the sensation uncomfortable.

To reduce the time spent in the muscle recruitment deadzone, the first cycle of the control update was set to the initial twitch value of the participant, and the pulse width was constrained within the commonly used region, $0 \leq u \leq 300$, ensuring comfortable use (Wederich et al., 2000). Then the identification procedure discussed in Section 6.2 was performed. This produces the plant model $P(q)$, pictured in Figure 6.6.

To limit the effects of fatigue, there was a 20-minute break between each experiment, allowing the muscles to recover (Graham and Popovic, 2005). To limit the impact of model uncertainty, all experiments for a given participant were conducted in a single session, using the same initial model and pad position.

6.4 Results

The simulations performed in Subsection 5.2 found that point-to-point RC increased convergence speed and robustness compared to traditional RC. As in Subsection 5.2, the convergence speed experiments will be repeated in the initial human experiments for both traditional RC and point-to-point RC. However, instead of the robustness experiments performed in simulations, repeatability experiments are performed to investigate how the controllers deal with the time-varying muscle characteristics, involuntary twitch responses and harmonic oscillations. Previously, the value of the control effort was not focused upon. Now the control effort for each cycle will be measured as it relates to the rate of muscle fatigue and stabilisation of muscle strength.

For all data, unless stated otherwise, the error norm is calculated using the subset of M points for both controllers to ensure the results are comparable ($||\mathbf{\Phi}e||^2$). Note that different starting values are observed due to small variations in starting angle of the resting foot.

6.4.1 Representative Results

Traditional and point-to-point RC were implemented using update (4.86). The latter tracked the indices given by (6.2), and the former tracked all points (i.e. $M = N$, $i_1 = 1, \cdots, i_N = N$). The minimum energy filter is not altered ($F = I$). This was chosen because the minimum jerk filter provided little benefit in the validation simulations (see Section 5.2.1), whilst shortening the plant model length, thereby reducing the model's accuracy. This simplifies the traditional and point-to-point updates to (4.4) and (4.46) respectively.

Figure 6.9 shows the results from representative trials for participant 1 and 2, who had the best and worst tracking performance, respectively. The point-to-point RC tracking is observed to converge faster for both participants, despite the presence of noise, exogenous disturbance and fatigue. This confirms that the gradient algorithm solves the RC update (as shown in Theorem 4.1) and the sufficient convergence criteria (as given by Theorem 4.2). For completeness, Figure 6.10 shows the corresponding stimulation u which produced Figure 6.9. Traditional RC is seen to use more stimulation as it tries to achieve perfect tracking of the full reference. Due to the non-linear relationship between control effort and angular output, the resulting input signals can appear very different.

The convergence speed and control effort are now investigated for each controller. For both cases, results for one participant are focused on in repeatability experiments and then results from all participants are considered to ensure the results are robust to human variation. In all cases, the controller is applied for 30 cycles (60 seconds).

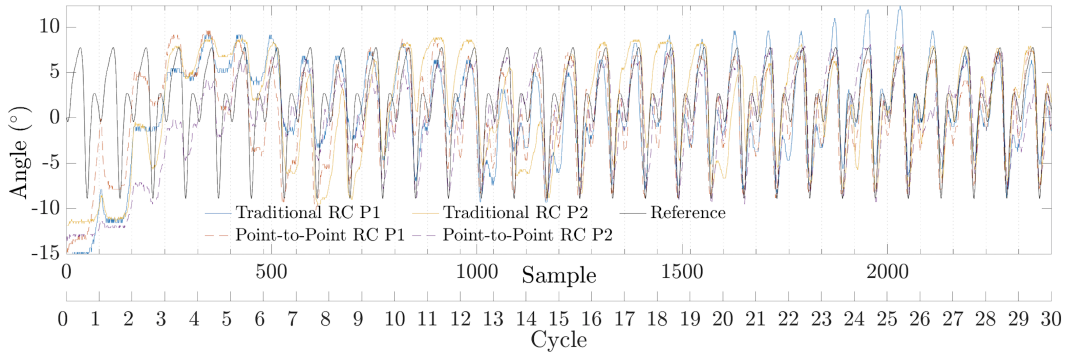

Figure 6.9: Representative outputs, for participant 1 and 2, for traditional and point-to-point RC control schemes.

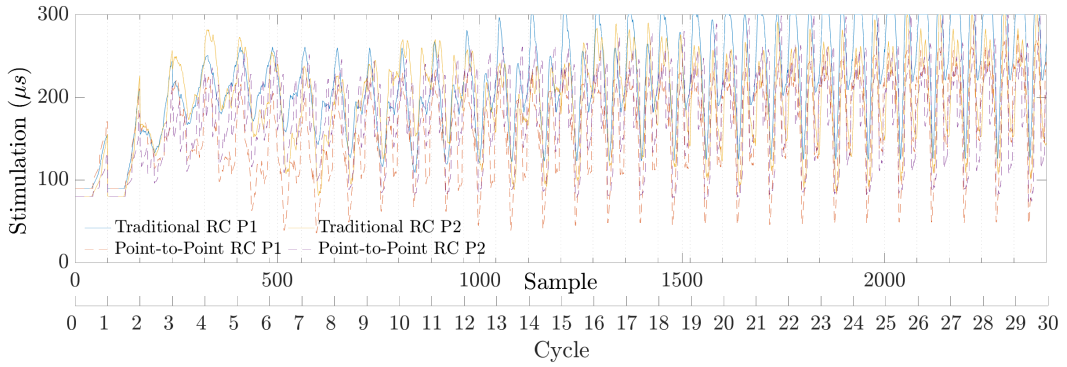

Figure 6.10: Representative inputs, for participant 1 and 2, required to produce the representative outputs.

6.4.1.1 Convergence

First, a repeatability experiment was performed on participant 1. Each control scheme was repeated 3 times with the same learning rate (β) of 80%. The percentage denotes how the selected value differs from the best β value (i.e. producing fastest convergence), which is based on the nominal plant model (Lemma 4.3), i.e. the nominal value

$$\frac{2}{\sup_{\omega\in[0,\pi]} |P(e^{j\omega})|^2}. \tag{6.3}$$

The points of subset M are used to compute the error norm. Figure 6.11 shows that point-to-point controller converges faster (3 cycles until 10% error norm) than traditional repetitive control (7 cycles until 10% error norm). The point-to-point controller also demonstrated desirable repeatable characteristics (point-to-point RC standard deviation 0.04, traditional RC standard deviation 7.44), despite involuntary twitch and fatigue. It was noted that point-to-point had little to no oscillation visible in the error norm, suggesting improved robustness to model uncertainty compared to the traditional controller that was unable to stabilise to a consistent value.

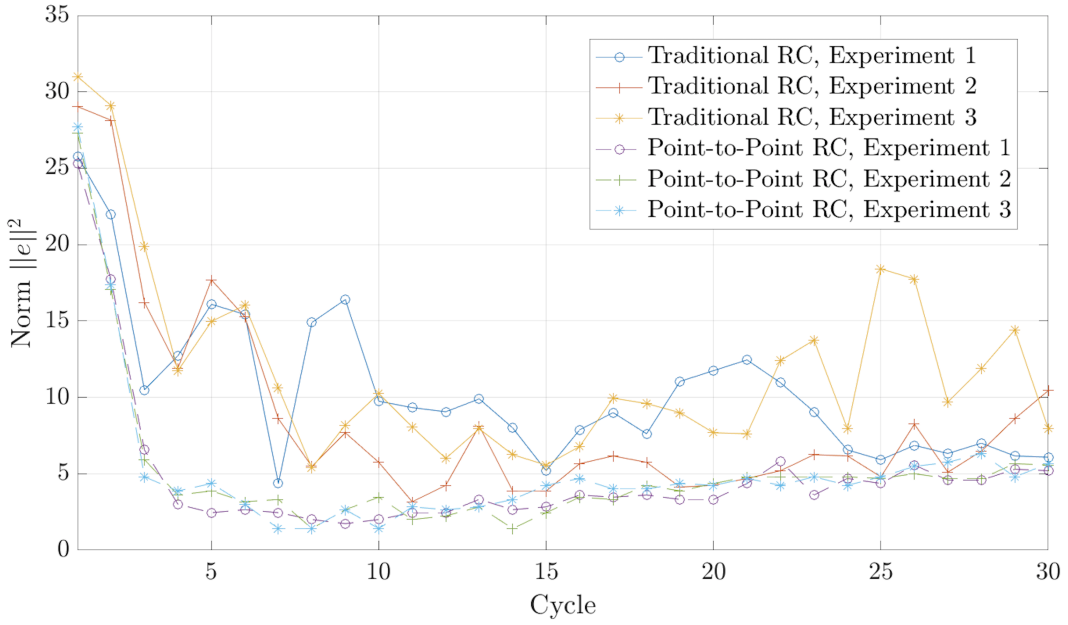

Figure 6.11: Participant 1: repeatability experiment - convergence.

6.4.1.2 Control Effort

The amount of control effort is of interest as it directly correlates with fatigue and possible discomfort. Figure 6.12 shows the control effort norm for each cycle ($||u||^2$) to achieve the tracking motion. The total control effort is consistently lower for the point-to-point controller as well as being highly repeatable. This confirms the minimum energy principle (Theorem 4.5) and suggests the 20 minute recovery time is enough to reduce fatigue between experiments to a suitable level. Point-to-point RC is likely able to achieve lower energy levels as the traditional RC tries to achieve every point. This means the norm stimulation required is more easily overestimated, potentially in areas entering the saturation region of the isometric recruitment curve. Thus, although the same output could be achieved with less stimulation, levels are not reduced as the tracking level has been achieved. The stimulation is also seen to increase with time as it acts against the effect of fatigue until fatigue plateaus. Although this enables tracking to be maintained, this does compound the fatiguing effect and is an inherent limitation of all FES assistive technology. This can also be seen in Figures 6.9 and 6.10. After 25 cycles, the control effort begins to levels off to a fixed value as the initial effect of fatigue is fully realised.

6.4.1.3 Discussion

The key parameters from the repeatability experiments, including the root mean square (RMS) and standard deviation (SD) of the results, are given in Table 6.1. The repeatability of the point-to-point controller is greater compared to traditional RC due to the

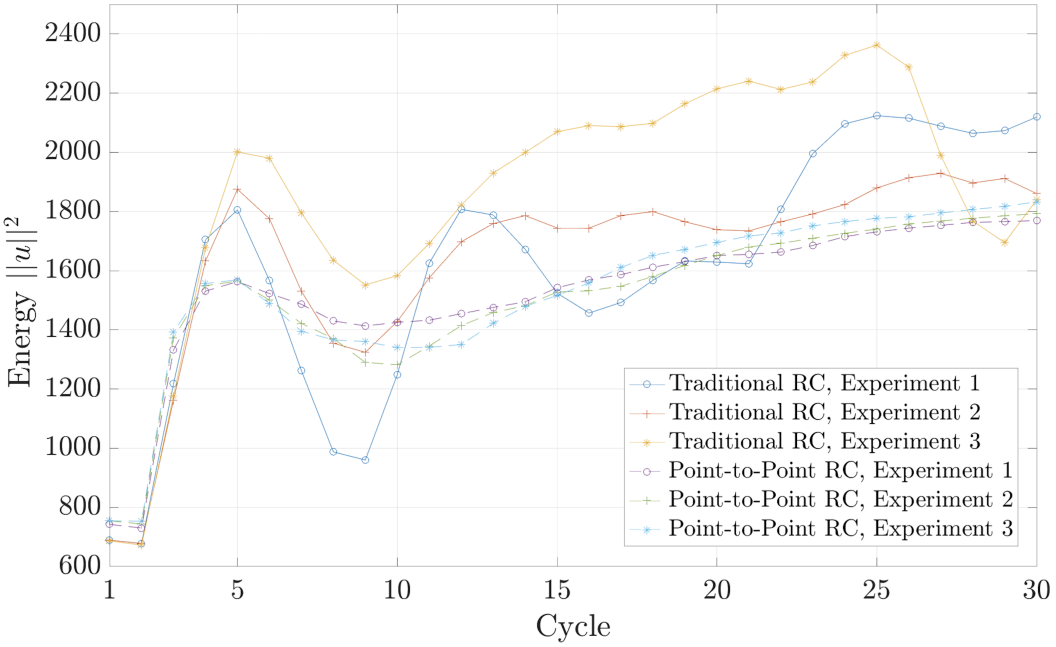

Figure 6.12: Participant 1: repeatability experiment - control effort.

lower standard deviations across all conditions. The point-to-point RC shows better tracking of the M key points, as well as better tracking of the entire signal, reinforcing robustness to non-voluntary twitches or muscle spasms. The control effort is consistently lower for point-to-point RC. The average error for tracking the whole cycle is shown to be within the 4 degrees variation of natural gait (Seel et al., 2016) for both controllers. The convergence for both controllers is repeatable at the 10% error norm level. However, only point-to-point is achievable/reproducible at the 5% error norm level.

	Experiment	Average Norm $(\frac{1}{6}\sum_{n=25}^{30}\|\|\mathbf{\Phi}e_n\|\|^2)$		Control Effort $(\sum_{n=0}^{30}\|\|u_n\|\|^2)$		Full Cycle Error Norm [Average Degree Error] $(\frac{1}{6}\sum_{n=25}^{30}\|\|e_n\|\|^2)$		Cycles to 10% [5%] Error Norm $(\|\|\mathbf{\Phi}e\|\|^2)$
		Value	RMS ± SD	Value	RMS ± SD	Value	RMS ± SD	Value
Standard RC	1	37.17	41.27 ± 4.48	47019	50021 ± 4119	31.89 [3.2]	36.85 ± 7.44 [3.6 ± 0.64]	7 [7]
	2	40.15		48079		32.23 [3.2]		7 [11]
	3	45.99		54625		44.94 [4.3]		8 [N/A]
P-to-P RC	1	30.26	29.02 ± 1.16	44614	44510 ± 309	26.57 [2.4]	26.89 ± 0.04 [2.52 ± 0.11]	3 [4]
	2	27.99		44162		26.69 [2.54]		3 [4]
	3	28.76		44752		27.39 [2.6]		3 [3]

Table 6.1: Key performance parameters of the repeatability experiments.

However, to better confirm the initial findings, further investigation is required. This is achieved by expanding the sample size of the study. Increasing the number of participants introduces different physiologies, voluntary/non-voluntary muscle responses and levels of model uncertainty.

6.4.2 Cohort Study

To provide further transparency, Figure 6.13 graphically displays representative results, specifically cycle 27 to 29, for all participants. It highlights variation caused by disturbances and the update action of the controller between each of the trials.

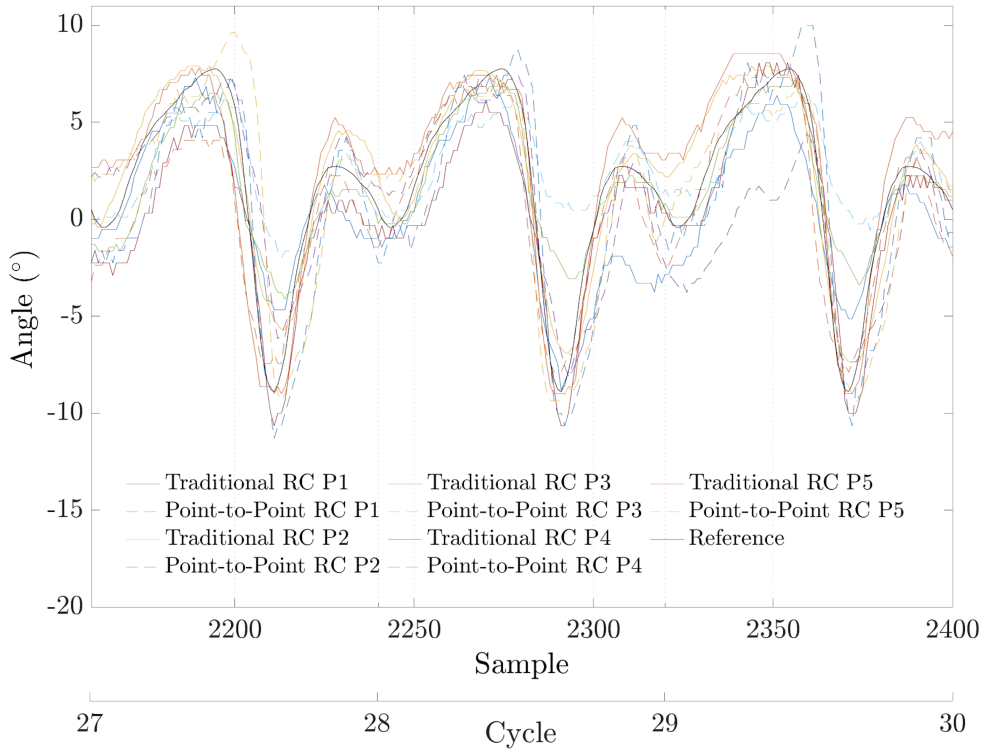

Figure 6.13: Representative outputs for all participants, cycle 27 to 30

Table 6.2 contains data gathered from all participants using a gain value corresponding to 80% of the sufficient learning rate condition equation (6.3). It compares key parameters for both the traditional RC and point-to-point RC. The point-to-point RC and traditional RC controllers achieve similar tracking for the subset of M points. The total control effort for the point-to-point scheme is lower or very similar in the majority of cases, supporting the minimum energy property of Theorem 4.6. Comparing the entire signals (N points) shows both controllers achieve excellent tracking, despite the point-to-point controller having only $\frac{1}{16}$ of the points to track. This justifies the use of the gradient algorithm in Lemma 4.3 and the minimum energy condition from Theorem 4.6. The point-to-point RC can also be seen to converge below the 10% and 5% error norm levels faster.

Table 6.3 contains the Root Mean Square Error (RMSE) in degrees of the last 5 cycles of the recorded data for all 5 participants. The mean and standard deviation of the full cycle error norms for traditional RC is 2.69 ± 0.72 and for point-to-point RC is 3.64 ± 1.4667. Omitting participant 2 (because of a potentially undiagnosed condition of involuntary twitch) leads to traditional RC having 2.56 ± 0.76 and point-to-point RC

Participant	Average Norm (M) ($\frac{1}{5}\sum_{n=26}^{30}\|\|\mathbf{\Phi}e_n\|\|^2$)		Control Effort ($\sum_{n=0}^{30}\|\|u_n\|\|^2$)		Average Norm of Full Cycle (N) ($\frac{1}{5}\sum_{n=26}^{30}\|\|e_n\|\|^2$) [Average Degree Error]		Cycles to 10% [5%] Error Norm ($\|\|\mathbf{\Phi}e\|\|^2$)	
	RC	P-to-P RC	RC	P-to-P RC	RC	P-to-P RC	RC	P-to-P RC
1	45.13	40.16	57519	43598	43.72 [1.8 °]	41.1 [1.6 °]	9 [20]	6 [12]
2	89.8	85.8	51895	48322	63.1 [2.6 °]	110.39 [4.2 °]	16 [N/A]	12 [N/A]
3	75.9	77	49745	46416	56.2 [1.93 °]	78.3 [2.6 °]	10 [15]	7 [10]
4	34.88	39.28	34691	50948	13.1 [1.28 °]	17.67 [1.49 °]	4 [8]	4 [7]
5	47.1	48.8	43779	44501	66.65 [2.33 °]	70.2 [2.48 °]	7 [10]	5 [10]

Table 6.2: Key performance parameters for all participants, $\beta = 80\%$

Participant	RMSE ($\sqrt{\frac{e^2}{5T_s}}$)	
	RC	P-to-P RC
1	2.19 °	2.06 °
2	3.15 °	5.52 °
3	2.81 °	3.91 °
4	1.57 °	1.97 °
5	3.32 °	3.51 °

Table 6.3: Root mean square degree error for both controls (cycle 25-30)

giving 2.99 ± 0.99. In all cases, the RMSE falls within the natural variance of gait (Seel et al., 2016). Additionally, the difference between the RMSE for traditional and point-to-point RC for participant 1 and 5 are the lowest. This confirms observations from other studies, where participants who have not used FES before may exhibit increased involuntary response (Freeman et al., 2015).

It is important to note that, in all cases, both repetitive controller schemes led to a stimulation input that is highly individual to each person, and potentially changes from day to day, without any changes to the FES parametrisation and reference trajectory used.

6.4.2.1 Discussion

Traditional RC and point-to-point RC have been compared in detail. Traditional RC achieved an RMSE of 2.56 ± 0.76 and point-to-point RC achieved 2.99 ± 0.99 across 4 participants. Repetitive control can now be compared more widely to the approaches discussed in Section 3.3. Both controllers performed better than neural networks (RMSE of $8.11, 7.81$ and 5.59), neural network + PID (RMSE of $5.57, 4.83$ and 5.05), neural networks + fuzzy logic (RMSE of $4.07, 3.75$ and 4.19) Chen et al. (2004). They also performed better than model-based open-loop control (RMSE of $8.2 \pm 2.3, 15.1 \pm 1.9$), feedback control (RMSE of $4.6 \pm 0.7, 7.3 \pm 2.4$) and feed-forward feedback hybrid control

(RMSE of $3.4 \pm 0.3, 5.7 \pm 2.6$) (Ferrarin et al., 2001). They achieved similar results to adaptive control (healthy participants 3.2 ± 1.2, stroke participants 3.4 ± 0.2). Note, that simple references, that did not resemble gait, were used (Kobravi and Erfanian, 2009). The RC controllers also achieved this without the time-lag issues that affected the feedback based controllers. They also handled time-varying issues such as fatigue which caused issues for rule-based control approaches. Additionally, the point-to-point repetitive controller has been able to achieve similar or better performance whilst using a fraction of the measurement data compared to traditional RC and significantly less data than what is required to train a neural network. The traditional RC algorithm is noted to generally have slightly better tracking abilities across the entire reference compared to point-to-point RC.

An inherent limitation of point-to-point RC, not investigated here is that it cannot correct for an external disturbance occurring between the tracked points. This, however, may be argued to be unlikely, and in many cases, it can even be considered an advantage to reject aperiodic disturbances. Further to this, stroke participants would be expected to vary from the current participants in terms of age, muscular stiffness and strength. These differences would be expected to be accounted for by the identification method and hence be embedded into the model and controller.

To further improve the results, an initial 'guess' at the required stimulation input needed to achieve the reference could be found by multiplying the inverse model by the reference. Then, instead of starting and converging from the twitch response level as used here for RC, the controller converges from an approximate solution. This was used successfully with the ILC controller in Seel et al. (2016).

6.5 Summary

Repetitive control has been applied experimentally in both its traditional form and point-to-point form. Point-to-point RC has been shown to be more repeatable, as well as more robust to uncertainties and non-linearities. The increased freedom in the signal evolution has allowed for faster convergence while using/storing far less data. Additionally, they were able to successfully maintain tracking despite fatigue by increasing the control effort with time. The controllers put forward have also been compared to other controllers within the literature and found to have better performance and characteristics for FES controlled drop-foot. These characteristics included: not having the time-lag issues that affected feedback controllers, requiring significantly fewer data points to train the model compared to neural networks, passing significantly less data between cycles compared to controllers in the literature and not requiring an initial guess to quickly converge to a solution.

Chapter 7

Pad Pattern Selection

The previous chapter used a fabric-based electrode array to evaluate the controller. This allowed automatisation of pad placement while improving wearability and breathability compared to polycarbonate arrays. To select a specific single pad from the array, a simple search algorithm was used before the proposed repetitive controllers were applied. This chapter proposes a more sophisticated approach that involves selecting a group of array elements. The focus will be on attaining a desired static posture through the application of stimulation to these elements. However, the group of array elements could also be used to apply the stimulation input for the previous repetitive controller.

7.1 Electrode Array Pad Selection

As introduced in Section 2.3.3, electrode arrays embed a number of electrode pads in a predefined 'layout' (the physical position of pads). There are two types of 'layout': the first has pads which are shaped to correspond to muscle positions, e.g. HandNMES (Snoek et al., 2000) and H200 Bioness. However, a mismatch between the muscle and pads can limit effectiveness (Crema et al., 2018) or require a bespoke system for every user. The second employs a grid layout which allows a broader application to different limbs and users, e.g. INTFES (Velik et al., 2011) and ShefStim (Kenney et al., 2016). However, an identification method is required to locate an appropriate electrode pad.

As first reviewed in Section 2.3.3 and further highlighted in Section 6.2, existing pad identification methods (e.g. Schill et al. (2009); O'Dwyer et al. (2006); Micera et al. (2010); Popović-Bijeli et al. (2005)) share a common approach which replicates manual trial and error pad placement. Each pad is activated in turn, and the resulting movement is recorded. The pad which produces the best movement (e.g. greatest dorsiflexion, least roll) is selected. Minor variations exist, including activating pairs or groups of pads, in turn, (Schill et al., 2009) and exchanging cathode and anode positions (O'Dwyer et al.,

2006). The most clinically studied approach is ShefStim system. ShefStim employs 64 electrode pads and combines multiple active pads to form a "virtual electrode" (Prenton et al., 2014; Kenney et al., 2016). A "virtual electrode" comprises 4 electrodes in a 2x2 configuration. The optimal position is identified by sequentially shifting the virtual electrode across and down the array. A participant perception survey, involving 10 individuals ranging from 26 to 79 years old, used ShefStim unsupervised for 2 weeks following initial consultations (Prenton et al., 2014). However, the setup time was found to be over 14 minutes on average, which is longer than setting up their own FES devices. Although ShefStim found the optimal pad position for the wearer, when participants were asked to score their own 2 channel FES devices against ShefStim, the long setup time resulted in the two systems receiving the same score on average.

This chapter investigates more advanced methods to select multiple electrodes to achieve the desired movement. The approach will be to treat the pad selection problem as a model-based optimisation using (linearised) dynamic models to capture the response of each electrode. Rather than solving the optimisation using only prediction, it will be performed iteratively using experimental data. This approach is termed 'Iterative learning'. The next section introduces the model and control approach. This is then experimentally validated in Section 7.4.

7.2 System Description

The approach selected for pad selection utilises an underlying model and the principle of superposition. Superposition states that for linear systems, the net response caused by two or more stimuli is the sum of the responses that would have been caused by each stimulus individually. Superposition has been shown to predict the response to multi-pad stimulation accurately (Popović and Popović, 2009). In this chapter, superposition is fused with learning through repeated attempts in the form of iterative learning control (ILC). A key novelty will be to embed constraints in the selection problem (e.g. selection of adjacent pads) that correspond to simplifications that could then be made to the electronics and/or array manufacture.

The approach requires that the block model structure of the single pad array-based FES (Figure 6.2) needs to be further generalised. The single input to the channel array switch is replaced with a dedicated input for every electrode pad, allowing different stimulation levels to be applied to each pad. A static mapping then translates the stimulation applied to the pads to the stimulation received by the z underlying muscles. Each of these muscles has its own isometric recruitment curve and linear activation dynamics. The resulting force generated by each muscle is combined within a tendon network to produce a net force which is then cascaded with the rigid body dynamics. The overall system model is given in Figure 7.1.

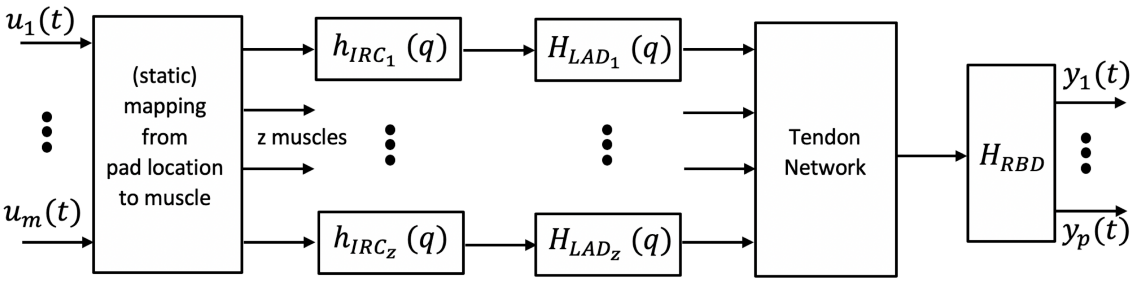

Figure 7.1: Block diagram of multiple-pad FES stimulation dynamics.

The multiple-pad FES stimulation block model is now expressed mathematically. The overall dynamic model links the musculoskeletal response, y, of the p joint angles to the stimulation, u, applied to the m-pads in the array. A general non-linear discrete-time form of the system in Figure 7.1 is given by

$$\begin{aligned} x(t+1) &= f(x(t), u(t)), \qquad & x(0) &= x_0 \\ y(t) &= h(x(t)), & t &= 0, 1, ..., N \end{aligned} \tag{7.1}$$

with state vector $x(t) \in \mathbb{R}^l$. Here $f(\cdot)$ and $h(\cdot)$ are continuously differentiable with respect to their arguments. The stimulation applied to the i^{th} pad is denoted $u_i(t)$, with $y_j(t)$ the angle of the j^{th} joint. The number of active pads defines the stimulation 'pattern'. Without constraints, u, corresponds to a full array with all elements independently controlled.

The model runs over N samples so that the input and output vectors can be arranged more concisely as the super-vectors

$$\begin{aligned} u &= [u(0)^T, u(1)^T, ...u(N-1)^T]^T \in \mathbb{R}^{mN} \\ y &= [y(1)^T, y(2)^T, ...y(N)^T]^T \in \mathbb{R}^{pN} \end{aligned} \tag{7.2}$$

This enables system (7.1) to be equivalently represented by the vector function relationship $y = g(u)$ where $g(u) = [g_1(u)^T, g_2(u)^T, ...g_N(u)^T]^T \in \mathbb{R}^{pN}$ with components

$$\begin{aligned} g_i(x(0), u(0), ..., u(i-1)) &= h(x(i)), \\ &:= h(f(x(i-1)), u(i-1))), \\ &:= h(f(f(x(i-2), u(i-2), u(i-1))), \\ &:= \vdots \\ &:= h(f(f(\cdots f(x(0), u(0), \cdots, u(i-2)), u(i-1))), \end{aligned} \tag{7.3}$$

where $i = 1, ..., N$. This system is now used to define the array pattern selection problem. The previous cost functions within Kenney et al. (2016); Schill et al. (2009); O'Dwyer et al. (2006); Popović and Popović (2009) all involve minimising the difference between joint angle, y, and the desired target movement, r, when stimulation u is applied. If

stimulation is applied to only one pad, then the problems of O'Dwyer et al. (2006); Micera et al. (2010); Popović-Bijeli et al. (2005) are described. Let Ψ be the set of all possible stimulation inputs with one non-zero element, that is

$$\Psi : \left\{ u \in \mathbb{R}^m | \quad u_i \begin{cases} = 0, & i \neq v \\ \neq 0, & i = v \end{cases}, \quad v \in \{1, ..., m\} \right\}. \tag{7.4}$$

The previous array selection problem is then defined as follows:

Definition 7.1. Array Selection Problem: Find a stimulation pattern that solves

$$\begin{aligned} &\text{argmin } J(u), \quad J(u) = \|r - g(u)\|_Q^2 \\ &\text{subject to} \quad 0 \leqslant u \leqslant u_{max}, \quad u(t) \in \Psi, \quad r \in \mathbb{R}^{pN}. \end{aligned} \tag{7.5}$$

Here, $Q \in \mathbb{R}^{N \times N}$ is a symmetric, positive-definitive weighted matrix, which allows the designer to allocate emphasis on minimising specific time points within the target movement.

To extend this objective, the constraint set Ψ is now generalised to enable a lower cost $J(u)$ to be attained within the minimisation problem. The constraint sets will be chosen to 1) simplify hardware manufacture and electronics, and 2) find distinct muscle groups.

7.2.1 Fixed Pad Pattern Size

The most general choice of constraint expands the pattern to include a greater number ($1 \leqslant n \leqslant m$) of active pads, such that disconnected multi-pad patterns can occur. Additionally, each pad in the pattern is allowed to have different levels. This generalises the objective in Popović and Popović (2009) to allow an arbitrary number, n, of pads to be within a pattern. The set is modified to

$$\Psi := \left\{ u \in \mathbb{R}^m | \quad u_i \begin{cases} \neq 0, & i \in S \\ = 0, & i \notin S \end{cases}, \quad S \in I_n \right\}. \tag{7.6}$$

Here, u_i again denotes the i^{th} element of u, and I_n is the set of all n-tuplets that are subsets of the set of all array indices $\{1, 2, ..., m\}$, i.e. each element $S \in I_n$ has form $S = \{i_1, ...i_n\}$. Figure 7.2 provides an example solution to Array Selection Problem (7.5) with Ψ and $n = 5$.

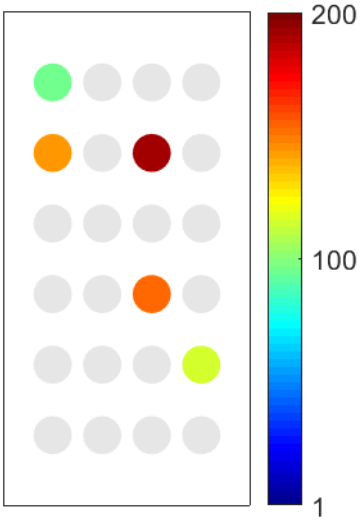

Figure 7.2: Example solution of array selection problem with constraint (7.6) and $n = 5$

7.2.2 Same Amplitude, and Fixed Pad Pattern Size

The next constraint forces all n pads in the pattern to have the same stimulation amplitude. This enables the number of stimulation channels to be decreased (i.e. one input can supply multiple pads), resulting in possible reductions to the number of channels in the electronics. The constraint still allows disconnected multi-pad patterns to occur. This is of particular interest as the same stimulation level across multiple pads has been shown to improve user comfort (Kuhn et al., 2010). Figure 7.3 shows an example solution to the Array Selection Problem (7.5) with $n = 4$ and Ψ equal to

$$\Psi := \left\{ u \in \mathbb{R}^m | \; u_i \begin{cases} = \bar{u}, & i \in S \\ = 0, & i \notin S \end{cases}, \; S \in I_n \right\}. \quad (7.7)$$

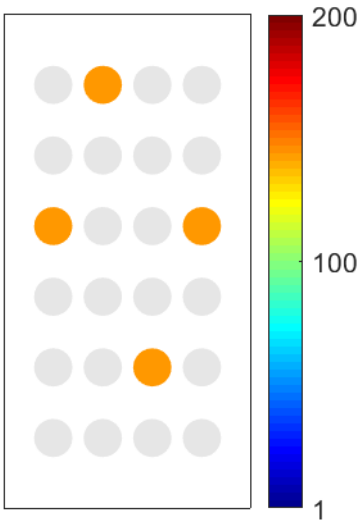

Figure 7.3: Example solution of array selection problem with constraint (7.7) and $n = 4$

7.2.3 Fixed Pad Pattern Size and Adjacent Element

The next constraint forces each pad to be connected, i.e. each selected element must neighbour another selected element. This is motivated by restricting the pattern to correspond to distinct muscle groups. Data from this constraint can be used to design personalised muscle electrode array layouts while reducing manufacturing costs (the number of required pads can be reduced to only cover the corresponding muscle group). Figure 7.4 shows a possible solution to the Array Selection Problem (7.5) with $n = 4$ and Ψ equal to

$$\Psi := \left\{ u \in \mathbb{R}^m | \; u_i \begin{cases} \neq 0, & i \in S_i \\ = 0, & i \notin S_i \end{cases}, \; S \in I_n, \right. \\ \left. \forall i \in S, \text{ such that } \exists j \in S, \right. \\ \left. \text{with } |r_i - r_j| \leqslant 1, \; |c_i - c_j| \leqslant 1 \right\}, \quad (7.8)$$

where, r_i, c_i and r_j, c_j are the row and column position of the i^{th} and j^{th} element respectively.

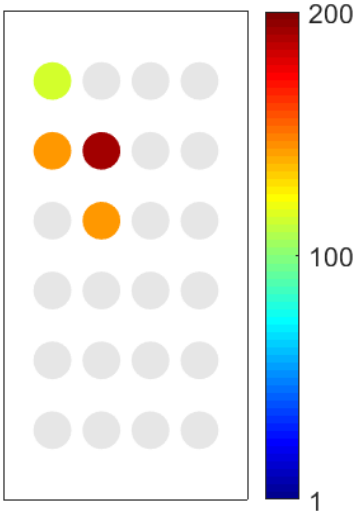

Figure 7.4: Example solution of array selection problem with constraint (7.8) and $n = 4$

7.2.4 Same Amplitude, Fixed Pad Pattern Size and Adjacent Element

Finally, combining the constraints in Section 7.2.2 and Section 7.2.3 enforces a connected pattern where all members have the same stimulation. This is the spatial generalisation of the rectangular virtual electrode approach used by Shefstim (Kenney et al., 2016). This has the most desirable commercial characteristics, as it simplifies hardware (it only needs one stimulation channel), focuses on muscle alignment (stimulates the main muscles, improving angular control) and reduces manufacturing costs as adjacent pads could be combined in personalised electrode arrays. Figure 7.5 gives an example solution to the Array Selection Problem (7.5) with $n = 5$ and Ψ equal to

$$\Psi := \left\{ \begin{array}{r} u \in \mathbb{R}^m \mid \; u_i \left\{ \begin{array}{l} = \bar{u}, \;\; i \in S_i \\ = 0, \;\; i \notin S_i \end{array} \right. , \;\; S \in I_n, \\ \forall i \in S, \;\; \text{such that} \;\; \exists j \in S, \\ \text{with} \;\; |r_i - r_j| \leqslant 1, \;\; |c_i - c_j| \leqslant 1 \end{array} \right\} \tag{7.9}$$

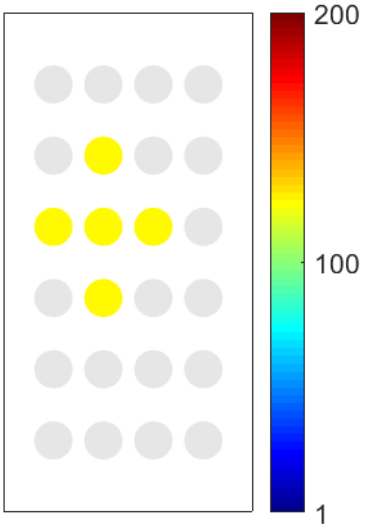

Figure 7.5: Example solution of array selection problem with constraint (7.9) and $n = 5$

7.3 Array Selection Solution using ILC

The Array Selection Problem of Definition 7.1 can be solved computationally by a range of constrained optimisation approaches, such as interior-point methods. However, to achieve the best results, a model-based approach which embeds learning from experimental data is desirable. Accordingly, iterative learning control (ILC) will be employed due to its track record in FES-based rehabilitation (Freeman, 2014). It has not previously handled non-linear systems with constraints of the form (7.5), so it will be extended in the next section.

7.3.1 Newton Method

An ILC algorithm that has been extensively applied to non-linear systems as well as being able to guarantee local convergence is Newton method-based ILC, which was formulated in Lin et al. (2006). The Newton Raphson method is a root-finding algorithm which produces successively better approximations through repeated iterations. To apply it to problem (7.5), first consider the unconstrained solution (i.e. $\Psi = \mathbb{R}^m$). Applying the Newton minimisation method to the pattern selection problem defined by (7.5) produces

the iterative update

$$u_{k+1} = u_k + \alpha \overbrace{g'(u_k)^{-1}\Big(\underbrace{r - g(u_k)}_{e_k}\Big)}^{\Delta u_k}, \tag{7.10}$$

where e_k, u_k are the error and stimulation respectively on the k^{th} iteration and the positive scalar α is the learning rate. As shown in Lin et al. (2006) the change in the input update, Δu_k, can be computed as the solution to

$$\|e_k - g'(u_k)\Delta u_k\|^2 = 0. \tag{7.11}$$

Update u_{k+1} is applied experimentally to the system ($y_{k+1} = g(u_{k+1})$), but solving (7.11) requires a linearised model of the system ($g'(u_k)$) on iteration k. This is used to combine the linear responses of pads and predict Δu. The constraints on Ψ, (7.6)-(7.9), can be embedded into the Newton method-based ILC update by modifying (7.11) to become

$$\begin{aligned} \text{argmin } J(\Delta u_k),\ J(\Delta u_k) &= \|e_k - g'(u_k)\Delta u_k\|^2, \\ \text{subject to, } u_k(t) + \Delta u_k(t) &\in \Psi, \\ -u_k \leqslant \Delta u_k &\leqslant u_{max} - u_k. \end{aligned} \tag{7.12}$$

This form arises by applying the constraints $u_{k+1} \in \Psi$ and $0 \leqslant u_{k+1} \leqslant u_{max}$ to the generalised form of problem (7.10), while noting $u_{k+1} = u_k + \Delta u$.

7.3.2 Identification Problem

The linearised system dynamics required in the ILC computation (7.11) have the standard form

$$g'(u_k) = \begin{bmatrix} \left.\frac{\partial g_1}{\partial u_1(0)}\right|_{u=u_k} & \cdots & \left.\frac{\partial g_1}{\partial u_1(N-1)}\right|_{u=u_k} \\ \vdots & \ddots & \vdots \\ \left.\frac{\partial g_N}{\partial u_1(0)}\right|_{u=u_k} & \cdots & \left.\frac{\partial g_N}{\partial u_{hv}(N-1)}\right|_{u=u_k} \end{bmatrix} \in \mathbb{R}^{pN \times mN}. \tag{7.13}$$

These components require a large amount of data to identify. By selecting $N = 1$, and a large sampling time, steady-state dynamics occur. This corresponds to applying a constant stimulation input u_k, and denoting the resulting steady-state angle output as $y_k = g(u_k)$. The corresponding linearised system for this case then becomes the much simpler static mapping

$$g'(u_k) = \left.\frac{\partial g_1}{\partial u_1(0)}\right|_{u=u_k} \in \mathbb{R}^{p \times m}. \tag{7.14}$$

Its identification is addressed in the next section.

7.3.3 Model Identification

The problem of identifying the matrix $g'(u_k)$ can be stated as

$$g'(u_k) := \underset{X}{\operatorname{argmin}}\ J(X), \quad J(X) = \|\tilde{y} - X\tilde{u}\|^2 \in \mathbb{R}^{p\times m} \tag{7.15}$$

where $\tilde{u}$ is a sufficently exciting input signal applied to the system about u_k and $\tilde{y}$ is the resulting output recorded about $y_k = g(u_k)$. The identification problem (7.15) can be solved efficiently by performing $i = \{1, ..., m\}$ tests. On the i^{th} test u_k is applied to all elements and an extra signal $\tilde{u}_k^i$ is added to element i. The resulting output is measured. From it, $y_{k,j}$ is subtracted from the j output element to produce $\tilde{y}_{k,j}^i$. The solution to (7.15) is then

$$X_{i,j} = \left(\frac{\partial g_1}{\partial u_1(0)}\bigg|_{u=u_k} \right)_{i,j} = (\tilde{u}_k^i)^\dagger \tilde{y}_{k,j}^i. \tag{7.16}$$

This solution then corresponds to the 'line of best fit' when $\tilde{u}_k^i$ is plotted against $\tilde{y}_{k,j}^i$. Hence the approach corresponds to approximating the response of the j^{th} output to the single varying i^{th} input u, by a straight line, thus reducing the effect of noise in a transparent, controlled manner. The approach can be seen clearly when $\tilde{u}_k^i$ is chosen to consist of straight-line segments of width $u_{i,width}$, as shown by Figure 7.6. This provides a smooth input for the user while covering the necessarily exciting $u_{i,width}$.

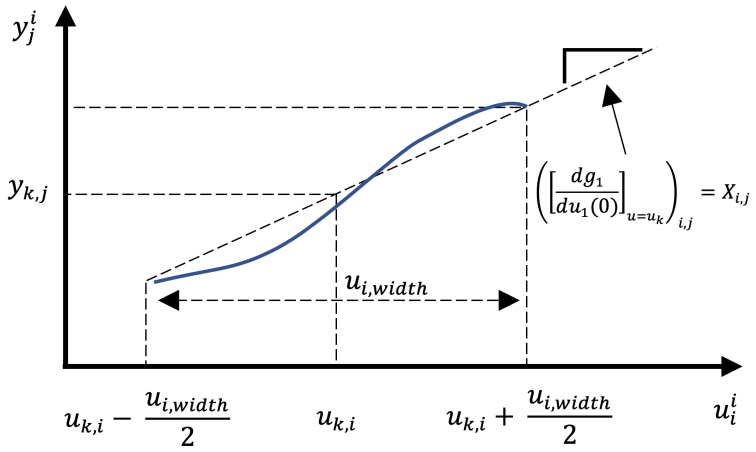

Figure 7.6: Linearised system: j^{th} output plotted against i^{th} input

This section has been summarised to give a procedure (Procedure 1) for the model identification in Algorithm 1.

Algorithm 1: Model identification procedure

Input : stimulation change $\tilde{u}_k^i$, operating point u_k
Output: angular change $\tilde{y}_{j,k}^i$ and linearised model $g'(u_k)$

1 set $i = 1$
2 apply FES stimulation u_k to all pads, and record $y_{k,j}$
3 apply additional signal $\tilde{u}_k^i$ to electrode pad i
4 record steady-state angular position and subtract $y_{k,j}$ to give $\tilde{y}_{k,j}^i$ for each joint j
5 increment i
6 **if** $(i > m)$ compute (7.16) to give $g'(u_k)$ for all pads **end**, **else** go to step 2

7.3.4 Selecting an Optimal Pattern

To find the optimal pattern of size n for a chosen constraint set Ψ, Newton method-based ILC (Section 7.3.1) is applied using the identified linearised model, $g'(u_k)$, which is found using the procedure in Algorithm 1. The optimal pattern selection procedure is given by Algorithm 2. Note, the target error, ε, is selected by the designer; however, for some patterns, it may be unachievable. To ensure an infinite loop does not occur, a maximum number of iterations is also selected.

Algorithm 2: General ILC procedure to solve the Array Selection Problem

Input : constraint Ψ, reference r, error target ε, max number of iterations k_{max}
Output: angular response y, error e and stimulation pattern u

1 set $k = 0$ and $u_k = 0$
2 identify linearised model $g'(u_k)$ using Procedure 1 given by Table 1
3 solve (7.12) to get Δu_k
4 compute $u_{k+1} = u_k + \alpha \Delta u_k$
5 apply u_{k+1} experimentally and record y_{k+1} and e_{k+1}
6 **if** $(\|e_{k+1}\| \leq \varepsilon)$ **then, end**,
else if $(k \geq k_{max})$ **then, end**,
else iterate k and go to step 2

By applying the Algorithm 2, the optimal pattern $(\min(e))$ can be found for a given constraint Ψ. However, applying the Algorithm in its current form would take a substantial amount of time due to re-identifying the m pads between each trial. To reduce the model identification time, the model identification procedure, given by Algorithm 1, is modified to speed up the procedure. This is done by applying the same constraints previously used to constrain the possible patterns.

7.3.5 Modifying the Model Identification Procedure

The model identification procedure performs m tests, one for each pad in the electrode array. However, when $g'(u_k)$ is used in problem (7.12) the solution is constrained by Ψ. Here, Ψ means many of the elements in the model will not be used, so there was no

reason for them to be identified. Therefore, the model identification can be simplified by applying the same constraints to the identification problem (7.15), i.e.

$$g'(u_k) := \underset{X}{\operatorname{argmin}}\ J(X), \quad J(X) = \|\tilde{y} - X\tilde{u}\|^2, u_k + \hat{u} \in \Psi \tag{7.17}$$

Applying the Fixed Pad Pattern Size constraint (7.6) to the model identification procedure, Table 1, causes the number of pads that need to be identified to reduce to only the n pads in the pattern. The model identification procedure, then is only run for the elements of indices $i = \{i_1, ..., i_n\}$. The linearised model is then $\mathbb{R}^{p\times n}$. Figure 7.7 shows the stimulation identification signals, $\tilde{u}_{k,i}$, for the Fixed Pad Pattern Size constraint pattern containing 3 pads. For larger patterns, the identification algorithm can still be time-consuming, requiring n tests. To further simplify the model identification algorithm, the Same Amplitude and Fixed Pad Pattern Size constraint (7.7) can be applied as explained next.

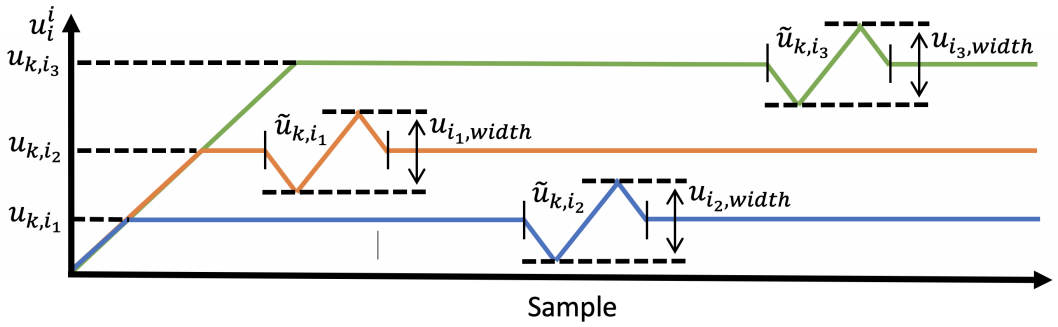

Figure 7.7: Identifying the model with the Fixed Pad Pattern Size constraint ($n = 3$)

The Same Amplitude and Fixed Pad Pattern Size constraint (7.7) again means only the n pads in the pattern need to be identified. However, it also forces all pads in the pattern to have the same stimulation level. This means that the pattern is now considered as a single (virtual) electrode. This means that all models can be identified simultaneously when attempting to identify the model of any single pad. Therefore, only one test is required to identify the model, irrespective of the number of pads, n, in the pattern. The linearised model is then $\mathbb{R}^{p\times 1}$. This simplifies the model identification solution (7.16) to

$$X_j = \left(\frac{\partial g_1}{\partial u_1(0)}\bigg|_{u=u_k} \right)_j = (\tilde{u}_k)^\dagger \tilde{y}_{k,j}, \tag{7.18}$$

consequently, this removes the need for step 5 and alters step 3 and 6 of the model identification algorithm. This also means that step 3 in the general ILC update (Algorithm 2), calculating Δu, is less reliant on the superposition principle since it does not combine separately identified dynamics, but still relies on a linear model of prediction.

Figure 7.8 gives the model identification algorithms with the constraints applied.

Algorithm 3: Fixed Pad Pattern Size constraint

Input : stimulation $\bar{u}_k^i$
Output: angular responce y, error e, stimulation pattern u

1 set $i = 1$
2 apply FES stimulation u_k to all pads, and record $y_{k,j}$
3 apply additional signal $\bar{u}_k^i$ to electrode pad i
4 record steady-state angular position and subtract $y_{k,j}$ to give $\bar{y}_{k,j}^i$ for each joint j
5 increment i
6 **if** $(i > n)$, compute (7.16) to give $g'(u_k)$ **end**, **else** go to step 2

Algorithm 4: Same Amplitude and Fixed Pad Pattern Size constraint

Input : stimulation $\bar{u}_k^i$
Output: angular responce y, error e, stimulation pattern u

1 set $i = 1$
2 apply FES stimulation u_k to all pads, and record $y_{k,j}$
3 apply additional signal $\bar{u}_k^i$ to the all pads simultaneously
4 record steady-state angular position and subtract $y_{k,j}$ to give $\bar{y}_{k,j}^i$ for each joint j
5 *Not applicable*
6 compute (7.18) to give $g'(u_k)$
end

Figure 7.8: Application of constraints to model identification algorithm

7.4 Application to Drop-Foot

The approach described in this chapter is now validated by applying it to the pad placement problem for drop-foot using the same experimental hardware setup, reported in Section 6.1.1.

Following ethical approval (ERGO/FPSE/47517), three healthy participants were recruited. Participant 1 and 3 had experience/partaken in FES studies before. The participants were asked to sit on an elevated stool, leaving the leg able to swing freely, and to relax the muscles in their leg.

To make each test comparable, the effects of fatigue were limited by including a 20-minute break between each test set, allowing the muscles to recover (Graham and Popovic, 2005). As before, the stimulation input on each trial is bounded to ensure comfort, $0 \leq u_k \leq 300$.

7.5 Results

Although the modified model identification algorithms, given in Figure 7.8, are substantially faster to perform, it would still take a substantial amount of time to repeat Algorithm 2 for all possible patterns Ψ. Therefore, to reduce the time it takes to identify a pattern, several simplifications need to be made to Algorithm 2. These are (1) the model is fixed at $g'(u_0)$ and not re-identified and (2) instead of applying the input u experimentally in step 5 the model is used to predict the response, $y_k = g'(u_0)$. Note, that Algorithm 2 solves the array selection problem for a given Ψ. But the more general problem is to find Ψ that minimises the cost. This means that Algorithm 2 needs to be repeated for all Ψ to find the constraint with the lowest cost.

Although the constrained forms of the model identification will considerably speed up the selection of a pattern, not re-identifying the model at the beginning of each trial

around the new operating point increases the discrepancies between the model and the real system. To overcome this, the general form of Algorithm 2, is applied to the selected pad pattern with the modified model identification procedures to fine-tune the stimulation pattern.

The following focuses on results from participant 1. The results for participant 2 and 3 are included in Appendix E, and are referred to throughout this section.

7.5.1 Array Gradients

Drop-foot involves dorsiflexion and roll, thus $p = 2$ (degrees of freedom) is chosen in the dynamic model (Figure 7.1). Step 2 of Procedure 2 is to identify the first linearised model $g'(u_0)$. The model describes the local relationship between the input stimulation for each pad and resulting ankle joint movement. The linearised model is found by following the model identification procedure defined by Algorithm 1. Specifically, the model is identified by first applying $u_0 = 0$ to all pads. The initial joint positions y_k are recorded (Algorithm 1, step 2) and then an additional signal, $\tilde{u}_k^i$ is applied to the i^{th} pad (step 3). This is given as a slow ramping (5 seconds) signal, which ensures steady-state characteristics, followed by a flat period (2 seconds). The additional input signal covers the full stimulation region, $0 \leq u \leq 300$. The resulting change in angle is recorded (Algorithm 1, step 4). Then the additional stimulation is applied to the next pad (Algorithm 1, step 5), resulting in m tests. Once the input has been applied to all the pads, the linearised model $g'(u_0)$ is calculated (Algorithm 1, step 6). The elements in the model $g'(u_0)$ are shown in Figure 7.9 for participant 1. A strong inverse coupled relation can be noticed between the dorsiflexion and the roll movements. The same is observed for participant 2 and 3.

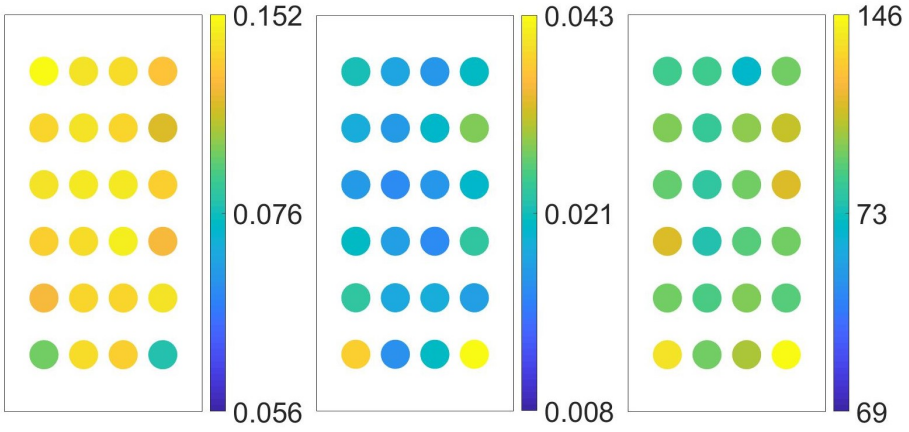

Figure 7.9: 1) dorsiflexsion component, 2) eversion component ($\theta/\mu s$), 3) twitch threshold (μs) values, for each pad. 1) and 2) form the 2-degrees of freedom model $g'(u_k)$ around the joint.

7.5.2 Identified Pad Patterns

The linearised model $g'(u_0)$ (found in the previous section) is now used to find patterns that solve (7.12) and consequently the pad placement problem given by definition 7.1. To do this, the general ILC procedure for optimal pad pattern selection (Algorithm 2) given by Algorithm 2 is followed with the model identification (Algorithm 1) found in Algorithm 1, and the brute force search method is used to solve (7.12) every trial. To speed up the optimal pattern selection the algorithm is simplified by (1) the model is fixed after the first identification at $g'(u_0)$ and is not re-identified (2) instead of applying experimentally in step 5 the input is applied to the model to predict the response, $y_k = g'(u_0)$. The procedure was run using the model $g'(u_0)$, constraints Ψ, learning rate $\alpha = 0.8$, max iterations $= 5$, static reference $r = [20, 7]$ (which corresponds to the maximum dorsiflexion and eversion required during gait) and number of pads $n = 1, 2, 3, 4$ and 5.

The unique pad patterns and stimulation levels for participant 1 are illustrated in Figure 7.10. When $n = 4$ a strong similarity is observed between each constraint (Fixed Pad Pattern Size (7.6), Same Amplitude and Fixed Pad Pattern Size (7.7), Fixed Pad Pattern Size and Adjacent Element (7.8) and Same Amplitude and Pad Pattern Size and Adjacent Element (7.9)) is observed. Specifically, all constraints share at least 2 common pads for $n = 4$ and 5. The Adjacent Element constraints (7.8), (7.9) for $n = 4$ and 5 are identical. Similarly, the Fixed amd Same Amplitude Pad Pattern Size constraints (7.6), (7.7) for $n = 5$ share 4 out of 5 pads. It is also observed that the minimum and maximum stimulation levels in each pattern decreases as the number of pads increases.

7.5.3 Simulation Results

The corresponding predicted error and mean stimulation levels of the pad patterns seen in Figure 7.10 are presented in Figure 7.11. In all cases, including participants 2 and 3, adding additional pads produced a better result which matches the underlying theory. The only exception is the Same Amplitude Fixed Pad Pattern Size and Shape constraint ($n = 5$) for participant 1. The fixed pad pattern size constraint allows patterns with $n > 1$ to achieve near-perfect results. The Same Stimulation constraint can be seen to reduce the accuracy of the result, especially for the Same Amplitude and Fixed Pad Patterns Size constraint, such that the two pad pattern is expected to have the best result.

Two of the constraints allow for each pad in a pattern to have different stimulation levels. The variation between pads can suggest the importance of fine-tuning the stimulation level to achieve gestures accurately. The stimulation levels for participant 1, Fixed Pad Pattern Size (7.6) and Fixed Pad Pattern Size and Adjacent Element (7.8) constraints, had an average percentage variation of 6.3% and 10.7% respectively across

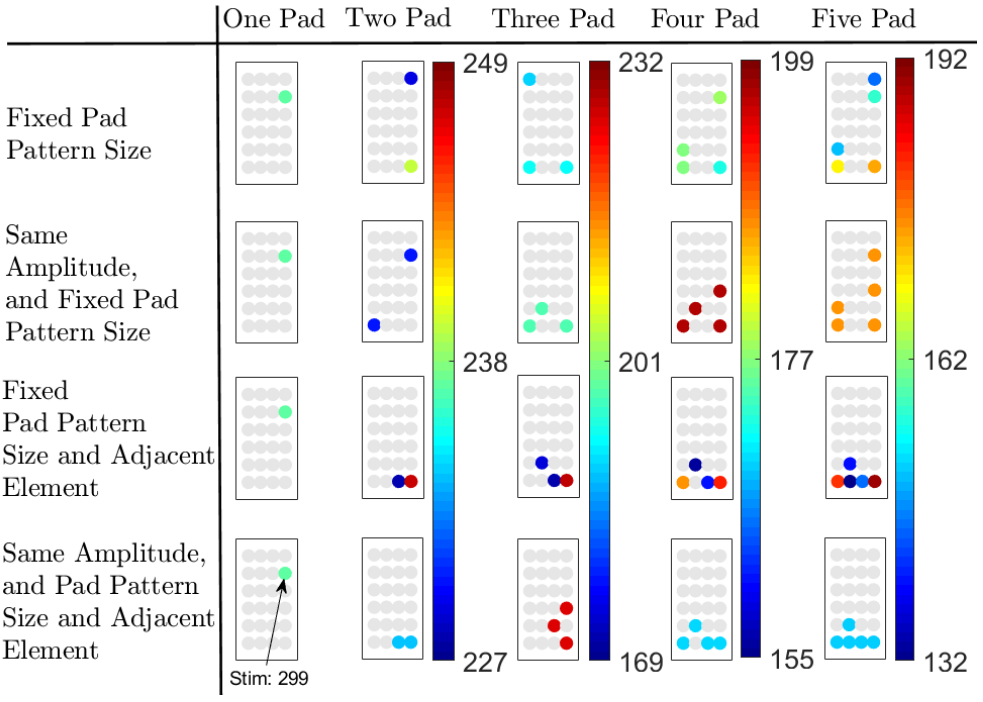

Figure 7.10: Optimal pad patterns for each constraint, with stimulation levels (μs) in grouped columns.

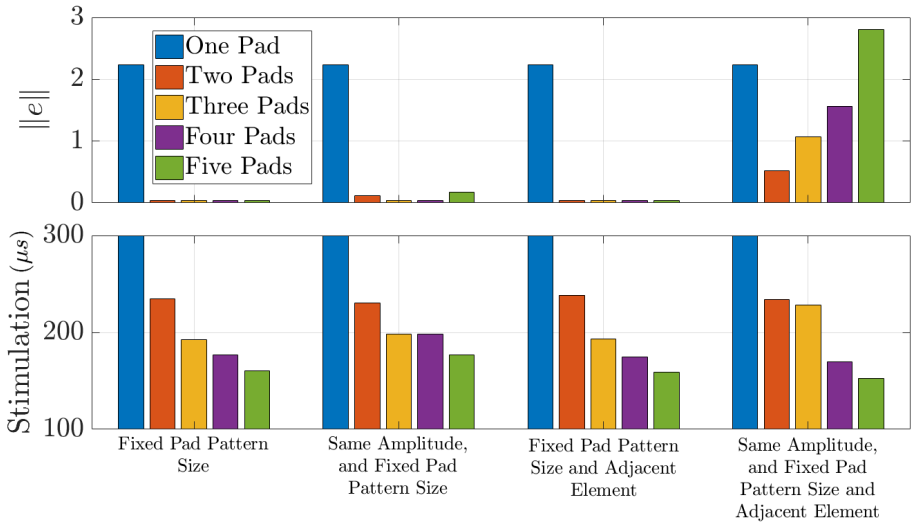

Figure 7.11: Simulation results for participant 1.

each pattern. Participant 2, however, had a stimulation variation of 28.5% and 31.2% respectively, while participant 3 had 0% and 0.75% respectively. This suggests that the importance of fine-tuning the stimulation patterns depends upon the muscle dynamics of each participant.

7.5.4 Experimental Results

Next, the selected pad patterns and corresponding stimulation levels, which were the outputs found by applying a simplified form of Algorithm 2 are now applied experimentally. Note, the pad patterns and stimulation levels, which are shown in Figure 7.10, are applied with no further updating or alteration. This allows the model error to be investigated. This is done by performing 1 iteration of Algorithm 2 but now without the simplifications applied previously and skipping to step 5, as the previous steps (calculating the pad pattern stimulation levels) have already been performed. The resulting change in the angular position of the ankle is recorded. The experimental results are the average of 3 tests with the standard deviation of the results given. The error is calculated using equation (7.5). Table 7.1 contains the results for participant 1.

Participant 1's results generally show that by increasing the number of pads, the error in achieving the results and the modelling error both reduce. This is most likely because adding more pads smoothes the non-linear dynamics of the system, which allows the linear model to represent the dynamics better further away from the operating point. Similarly, the experimental results of participant 2 tended to improve until 3 pads were used. Then the accuracy consistently decreases. The results of participant 3 did not have a clear trend. For all participants, the experimental results were consistently worse than what the model expected. Because only 1 model has been used to generate all the results for each participant, an in-depth study can now be performed into the accuracy of the linear model at representing the non-linear dynamics.

Table 7.1: Simulation and experimental data for participant 1

Constraint	Number of Pads	Simulation		Experimental		
		Stimulation	Error	Dorsiflexsion	Roll	Error
Fixed Pad Pattern Size	1	299	2.24	27.4 ± 0.17	1.77 ± 0.09	12.63 ± 0.26
	2	234 ± 5.5	0.04	22.85 ± 0.36	3.33 ± 0.02	6.52 ± 0.38
	3	192 ± 1.89	0.04	25.36 ± 0.47	2.2 ± 0.08	10.16 ± 0.55
	4	176 ± 25.9	0.04	22.6 ± 1.66	3.93 ± 0.83	5.67 ± 2.49
	5	160 ± 11.45	0.04	20.96 ± 1.15	4.3 ± 0.26	3.66 ± 1.41
Same Amplitude, Fixed Pad Pattern Size	1	299	2.24	27.38 ± 0.62	2.42 ± 0.33	11.96 ± 0.96
	2	230	0.12	25.71 ± 0.52	2.75 ± 0.21	9.96 ± 0.73
	3	198	0.04	23.4 ± 0.67	3.46 ± 0.33	6.94 ± 1.00
	4	177	0.17	22.25 ± 0.92	3.54 ± 0.29	5.71 ± 1.21
	5	158	0.79	19.15 ± 0.38	4.87 ± 0.11	2.98 ± 0.49
Fixed Pad Pattern Size, and Adjacent Element	1	299	2.24	26.67 ± 0.51	3.21 ± 0.48	10.46 ± 1.00
	2	238 ± 10.5	0.04	14.67 ± 1.89	3.21 ± 0.48	9.12 ± 2.33
	3	193 ± 27.35	0.04	21.28 ± 1.78	6.27 ± 0.44	2.01 ± 2.14
	4	175 ± 16.19	0.04	23.02 ± 0.54	3.62 ± 0.19	6.4 ± 0.73
	5	158 ± 23.7	0.04	23.63 ± 4.42	4.49 ± 0.2	6.14 ± 4.62
Same Amplitude, Fixed Pad Pattern Size and Adjacent Element	1	299	2.24	27.51 ± 0.14	2.33 ± 0.13	12.18 ± 0.27
	2	234	0.52	27.08 ± 0.58	2.22 ± 0.4	11.86 ± 0.98
	3	185	1.82	21.58 ± 0.8	4.35 ± 0.22	4.23 ± 1.02
	4	170	1.56	20.46 ± 0.59	4.63 ± 0.17	2.83 ± 0.76
	5	152	2.81	19.44 ± 0.67	5.3 ± 0.59	2.26 ± 1.26

7.5.5 Model Accuracy

A range of different constraints has been applied experimentally in the last section. There are two main ways of grouping the results to consider the model accuracy, (1) grouping in terms of the constraint Ψ or (2) grouping by the number of pads, n, in a pattern. Table 7.2 gives the average error and the standard deviation of the error for each participant and constraint. For each participant, the model uncertainty can be seen to be similar across each constraint, with the standard deviation remaining relatively consistent per participant. Table 7.3 portrays the model mismatch in terms of the number of pads. Again it shows a low model mismatch. This suggests that the model inaccuracy is not strongly related to the number of pads in a pattern or the constraint being used. Therefore suggesting that to improve the model accuracy further, the model needs to represent the non-linearity more accurately or more ILC trials need to be performed. The model inaccuracy for 2-degrees of freedom for each participant is $7.18° \pm 3.73°$, $13.18° \pm 5.42°$ and $8.95° \pm 2.27°$ for participant 1, 2 and 3 respectively and a model error of $9.77° \pm 4.78°$ for all results.

Table 7.2: Model mismatch for participant 1, 2 and 3, grouped by constraint.

		Model Mismatch (degrees)						
		Participant 1		Participant 2		Participant 3		Group
Fixed Pad Pattern Size	1	12.63 ± 0.26	7.73 ± 3.40	9.89 ± 0.75	9.19 ± 2.66	4.33 ± 0.56	9.78 ± 3.38	8.90 ± 3.28
	2	6.52 ± 0.38		6.86 ± 0.61		8.96 ± 0.3		
	3	10.16 ± 0.55		11.09 ± 0.65		11.95 ± 0.99		
	4	5.67 ± 2.49		5.37 ± 0.78		10.27 ± 1.94		
	5	3.66 ± 1.41		12.48 ± 1.48		13.40 ± 2.22		
Same Amplitude, Fixed Pad Pattern Size	1	11.96 ± 0.96	7.51 ± 3.24	9.09 ± 0.98	8.82 ± 1.85	8.11 ± 1.05	15.80 ± 4.27	10.71 ± 4.90
	2	9.96 ± 0.73		9.36 ± 0.92		6.970 ± 5.57		
	3	6.94 ± 1.00		5.51 ± 1.20		18.57 ± 1.35		
	4	5.71 ± 1.21		9.71 ± 0.51		17.52 ± 0.4		
	5	2.98 ± 0.49		10.43 ± 0.45		15.03 ± 1.39		
Fixed Pad Pattern Size, and Adjacent Element	1	10.46 ± 1.00	6.83 ± 3.58	9.69 ± 0.18	8.80 ± 2.65	10.67 ± 1.27	13.48 ± 6.33	9.70 ± 5.27
	2	9.12 ± 2.33		11.65 ± 0.50		18.03 ± 0.52		
	3	2.01 ± 2.14		4.38 ± 1.60		2.85 ± 1.49		
	4	6.4 ± 0.73		10.6 ± 1.38		15.24 ± 1.33		
	5	6.14 ± 4.62		7.44 ± 1.02		20.62 ± 1.27		
Same Amplitude, Fixed Pad Pattern Size and Adjacent Element	1	12.18 ± 0.27	6.67 ± 4.47	7.29 ± 0.64	8.97 ± 1.71	11.39 ± 1.67	13.65 ± 5.39	9.76 ± 5.08
	2	11.86 ± 0.98		7.30 ± 0.82		20.25 ± 0.46		
	3	4.23 ± 1.02		8.71 ± 1.16		18.60 ± 2.28		
	4	2.83 ± 0.76		10.36 ± 1.27		6.44 ± 1.17		
	5	2.26 ± 1.26		11.18 ± 0.84		11.56 ± 2.8		

Table 7.3: Model mismatch for participant 1, 2 and 3, grouped by the number of pads.

Number of Pads	Model Mismatch (degrees)			
	Participant 1	Participant 2	Participant 3	Group
1	11.81 ± 1.00	8.99 ± 1.11	8.63 ± 2.99	9.54 ± 2.85
2	9.87 ± 2.50	8.73 ± 1.92	13.84 ± 5.39	11.32 ± 5.10
3	5.84 ± 3.23	7.49 ± 2.73	12.99 ± 6.60	8.53 ± 5.57
4	5.15 ± 1.82	9.08 ± 2.21	12.37 ± 4.46	8.63 ± 4.43
5	3.76 ± 2.52	10.38 ± 2.01	15.15 ± 3.91	9.50 ± 5.66

7.5.6 Iterative Optimisation

To improve the angular output, the stimulation pattern is now fine-tuned. To do this, the general form of Algorithm 2, is applied with the modified model identification procedures given within Figure 7.8.

First, Algorithm 3, using the model identification procedure modified by the Fixed Pad Pattern constraint (7.6) is applied. The constraint limits the re-identified pads to just the n pads in the pattern and allows each pad in the pattern to have different stimulation levels. The experiment uses the pattern and stimulation solution to the Same Amplitude Fixed 3-Pad Pattern Size constraint as the input. For participant 1 the starting conditions are; pad pattern formed up of pads 8, 12 and 6, starting stimulation solution $u_0 = 210\mu s$, $\alpha = 0.05$, $r = [20, 7]$ and the operating range $u_{i,width} = \pm 20\mu s$.

Figure 7.12, contains the error values for each joint and stimulation levels of each pad for 10 iterations. The dorsiflexion and roll error both reduce below 5 degrees error. The average stimulation value can be seen to increase with time to maintain tracking due to fatigue.

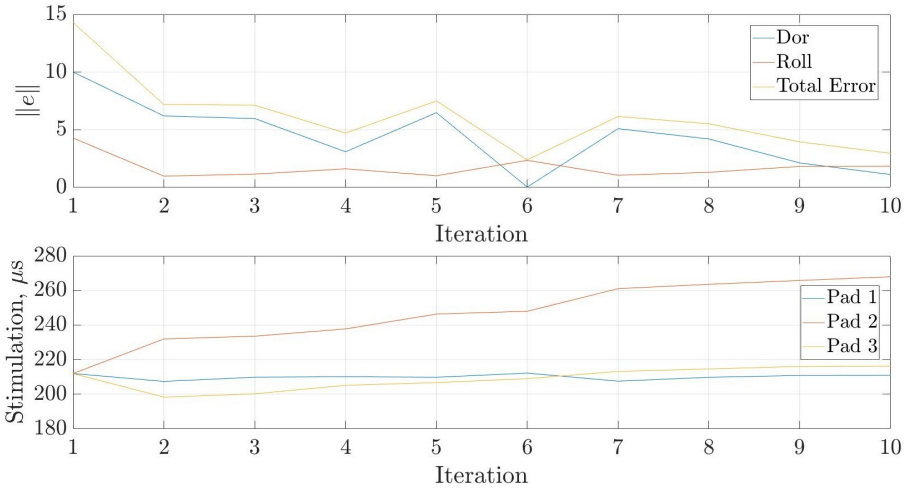

Figure 7.12: Experimental real-time ILC, using positive amplitude constraint.

Next, Algorithm 4 using the model identification procedure with the Same Amplitude Fixed Pad Pattern Size constraint (7.7) is applied. This constraint forces all pads to have the same stimulation level allowing all the pads to be identified at the same time. The experiment is run with the same starting conditions. The results are illustrated in Figure 7.13. Faster convergence is observed. This is likely to be due to a more accurate model because the Same Amplitude constraint has less reliance on superposition. It also requires fewer tests to identify the model, reducing the impact of fatigue.

The most accurate value from the Fixed Pad Pattern Size constraint is found on iteration 6, with the error dropping from 7.82° to 3.12°. To achieve this, the stimulation input

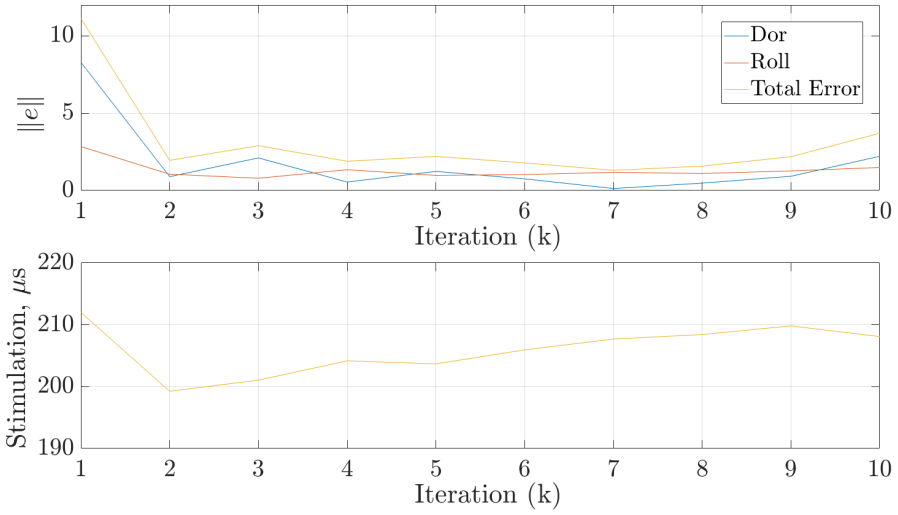

Figure 7.13: Experimental, real-time ILC, using Same Stimulation Amplitude constraint.

only changed by $6.94\% \pm 5.39$ ($163\mu S$ ($\Delta = 7\mu s$), $129\mu s$ ($\Delta = 27\mu s$) $161\mu S$ ($\Delta = 5\mu s$)). To investigate the repeatability, the stimulation levels were re-applied. Each pad was ramped up to its maximum value, and the angular movements are recorded. This was repeated 10 times and led to an angular position of $19.8° \pm 0.87°$ for dorsiflexion and $4.99° \pm 0.37°$ for roll resulting in an error of $2.2° \pm 1.23°$, improving on the un-tuned initial error of $7.82°$. This demonstrates the importance of re-identifying the model for this participant, as small changes in stimulation produce large angular changes.

7.6 Summary

This chapter has developed a framework for identifying multiple electrode pad patterns and considered the implications of constraints, which provide hardware simplifications and cost reductions while improving accuracy and repeatability. The pad selection approach has been justified by the low model mismatch between the predicted outputs and experimental results across all the constraints (error $9.77° \pm 4.78°$ for 2-degrees of freedom). It was specifically found that increasing the number of pads decreases the average stimulation needed across those pads. The patterns tended to converge to similar shapes for larger values of n, suggesting a similar optimal pattern lies within all the constrained systems. The majority of patterns did not, however, resemble rectangular shapes which have been heavily used in virtual electrodes in previous work suggesting the importance of considering the shape of active sites in future work. The importance of online fine-tuning has also been demonstrated, with small stimulation changes required for accurate tracking.

Chapter 8

Conclusions and Future Work

8.1 Conclusions

The focus of this thesis was to address the limitations in the technology available to people with drop-foot. It found that commercial FES stimulators have not been able to achieve a natural gait pattern with FES due to simplistic controllers which were unable to cope with the non-linear time-varying dynamics and voluntary ankle motion. In particular, all commercial systems use simple heel switches to activate the stimulation. This motivated the need for closed-loop model-based control with learning over each cycle. One of the few controllers in the literature able to address the limitations was based on learning (Seel et al., 2016). However, this approach requires a large amount of data to be passed between trials. Additionally, it assumes resetting between each gait cycle, a simplification of the complex periodic nature of walking. The control approach proposed in this thesis overcomes the resetting problem by using repetitive control, which is specially designed to deal with non-resetting continuous signals. Chapter 4 undertook this development, producing an RC implementation that had a set of theoretical properties that enabled the designer to vary the convergence, control effort and the number of points tracked which significantly reduced the amount of data the update required, stored and passed between cycles. The generalisation went on to allow the designer to specify different minimum energy solutions and to apply priority to points by using weightings.

The simulations, presented in Chapter 5, have illustrated that point-to-point RC converges faster and is more robust to model uncertainty than traditional repetitive control. Further to this, experimental results in Chapter 6 involving 5 participants, confirmed the findings of Chapter 5, and established initial clinical feasibility. Specifically, Chapter 6 found point-to-point RC was able to converge faster with similar accuracy and greater repeatability compared to traditional RC (variation 0.04 and 7.44 respectively), despite the point-to-point controller only using $\frac{1}{16}$ of the data traditional RC used. Across the

study, point-to-point RC achieved an error norm of $2.99° \pm 0.99°$ while traditional RC achieved $2.56° \pm 0.76°$. When compared to existing controllers in the literature, both RC controllers were found to have similar or better tracking abilities.

Another limitation in current FES technology relates to the difficulty for users to set-up the hardware, with challenging pad placement impeding user uptake (Dutta et al., 2012). In recent years this has driven focus on electrode array technology to relax the pad positioning problem (Kenney et al., 2016; Yang et al., 2014b), however, crude cost function procedures have limited the effectiveness of selection approaches (Kenney et al., 2016; Heller et al., 2013b). This motivated the second aim of this thesis, which was to develop improved automatisation methods for array positioning. Chapter 7 developed the framework and constraints needed to consider a large number of unique multi-pad pattern combinations by only using data from the individual pads. This speeds up the set-up process (approximate identification time is 3 mins for several thousand pad patterns), which was a consistent limitation of array technology in the literature (Kenney et al., 2016; Heller et al., 2013b), and had been key in preventing array electrodes from being commercial implemented.

The approach in Chapter 7 provides a way of identifying common patterns to activate the peroneal nerve, in either clustered or disjointed groups with the same or varying stimulation levels across the pattern. Although results are initial, the pattern selection model error for the 2-degrees of freedom, across all constraints and participants, was only $9.77° \pm 4.78°$, giving an accuracy band for all results (180 tests) of between 46.1% and 81.5%. Note, this is without re-identifying the model to tune the stimulation level. Once the pad pattern has been selected it is feasible for the model to be re-identifed between iterations. This has been shown to improve results, achieving $2.26° \pm 1.23°$ for the 2-degrees of freedom and an accuracy band of between 87.3% and 96.4%. This shows substantial scope for further refinement as well as the potential for being used to identify personalised drop-foot electrode layouts in the future or as the input to a multiple-input multiple-output (MIMO) point-to-point RC system.

8.2 Future Work

The results presented in this thesis illustrate the feasibility of point-to-point repetitive control for drop-foot as well as procedures identifying multi-pad pattern inputs for FES devices. This motivates the potential of real world application and larger clinical studies, as well as opening further routes of research.

8.2.1 Varying Trial Length - Multiple Model Control

The RC approach put forward in Chapter 4 has been shown able to track natural movement within typical human gait variation. However, it currently uses a fixed gait cycle with no means of effectively modulating the reference to account for changes in walking speed. This is important as a user's walking speed will vary in responce to various factors, including age, time pressure, leg length, tiredness, comfort and safety. To be able to include varying trial lengths, the proposed framework could be combined with multiple model adaptive control. This method updates the plant dynamics and reference between cycles based on how well the signals in the previous cycle matched. For example, the sensor input is used to switch to a suitable model by matching the ankle's angular acceleration and foot velocity.

8.2.2 Gait Reference Tracking

An alternative approach to address potentially varying trial lengths would be to change how the reference is propagated. Currently, the sample position within the reference is propagated independently of the system through the use of time. As RC does not reset between trials (it tracks both the swing and stance phases of gait), the sample position could instead be propagated by tracking and comparing the angular position of another limb to its know reference (Brend et al., 2015; Freeman, 2017; Freeman et al., 2018). For example, the arm or opposing leg position could be tracked (angular position, velocity and acceleration), and with this information, the position in the gait cycle can be ascertained. This approach would inherently account for variations in walking speed without the need for a large number of models.

8.2.3 Set of Optimal Pad Patterns

Commercially inspired array pad selection constraints were presented in Chapter 7. They were found to produce accurate, repeatable multi-pad input patterns. However, they were not yet able to help design personalised electrode array layouts as the constraints do not consider multiple days of data or account for the variation in electrode array placement. The next step would be to combine several models, each identified on a different day with the same participant. Then by using the constraints, a set of patterns could be found to solve the optimisation problem for all models with a minimum number of patterns. By placing the electrode array with enough variance each time, the set of selected patterns will be broad enough to solve the pad placement problem wherever it is placed during day-to-day use. Therefore, the end result would be a small set of patterns that can be quickly stimulated in turn during set-up rather than stimulating all individual pads, dramatically improving the time it takes to setup.

8.2.4 Combining FES with Soft Robotics

FES has been shown to work well, but fatigue is a limitation. Therefore, approaches that would potentially reduce the amount of stimulation required to control the pitch of the foot are desirable. For this reason, the expected next stage for assistive devices will combine mechanical systems and FES. This would also allow for a larger range of people to use assistive technology. However, mechanical systems have various limitations, including size, weight and wearability. Unlike mechanical systems, soft robotics does not limit the flexibility of wearable FES systems. However, soft robotic actuators are still in the early stages of development, as found by Section 2.3.5, and are not able to provide the force and support desired. Because of this, soft robotics should not be considered as actuators in a combined system. Instead, the aim should be to alter the system with soft robotics. Variable stiffness soft robotic fibres can provide extra stiffness around the ankle during swing phase and remove it during stance. This will change the rigid body dynamics slowing the drop of the foot and reducing the amount of stimulation that needs to be applied.

Appendix A

Outreach

During this research, I have been involved with various outreach activities which have helped me bring my work to the attention of the general public. This included presenting my work at a press conference for the 2018 British Science Festival in Hull, and representing the University of Southampton in a multi-university grant looking to combine soft robotics and FES into a wearable pair of trousers. This was called "The Right Trousers" project. I also exhibited at "The Trousers Fest" festival at the University of Bristol Robotic Labs, where I demonstrated the advancements in FES technology to the general public and had the opportunity to take on board user suggestions to develop the general form of the sock sleeve.

Figure A.1: Collage of various outreach events linked to this research.

Appendix B

Additional Physiology

This appendix contains additional detail about gait. This includes, further detail regarding the gait events, the muscles required for achieving the events and explanation of the key metrics measured (with average human values given where available) to evaluate human gait.

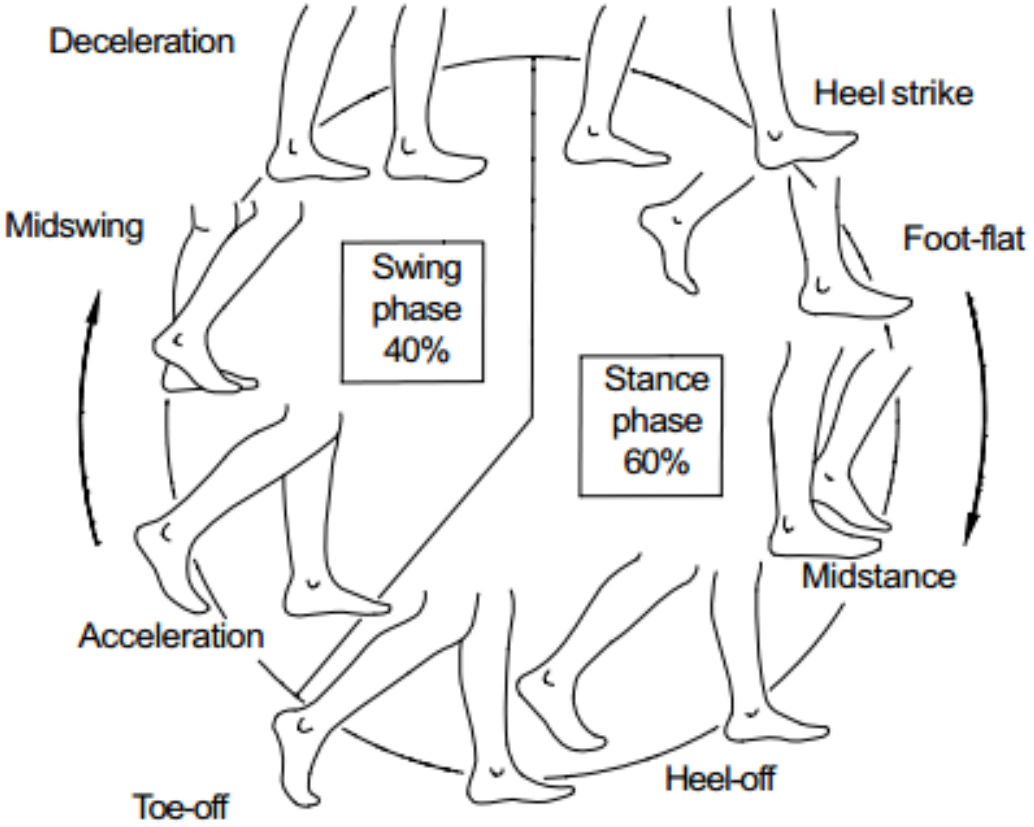

Figure B.1: Gait cycle organised as a clock. Emphasising the cyclic nature of human gait. From Vaughan et al. (1999)

Additional detail about the first 5 events that belong to the stance phase, and their approximate percentage position in the gait cycle, though this will vary from person to person, are given below.

Heel strike The instant the lower limb contacts the ground (0%). This represents the point at which the bodies centre of gravity is at its lowest position. Often referred to as initial contact because many abnormalities lead to the heel not making first contact.

Flat foot The period that the entire plantar aspect of the foot is on the ground (10%).

Midstance The point where the body weight passes directly over the supporting lower extremity (30%). Resulting in the body's centre of gravity being at its highest position. This coincides with a vertically oriented lower leg.

Heel-off The instant the heel leaves the ground (40%). This is initiated via the triceps surae muscles, which plantar flex the ankle.

Toe-off The instant the toe leaves the ground (60%). Ending the stance phase. Sometimes referred to as terminal contact.

Note, sometimes the term push off is used to describe the combined events of heel-off and toe-off.

Additional detail about the 3 events that belong to the last 40% of gait - swing phase, and approximate percentage position in the gait is now provided.

Acceleration Sometimes referred to as initial swing or early swing. The period from toe off to mid swing (60% to 75%). It begins as soon as the foot leaves the ground and the subject activates the hip flexor muscles to accelerate the leg forward.

Mid Swing The period when the foot in swing passes next to the foot in stance position (75% to 85%). This corresponds to the mid stance phase of the opposite lower extremity.

Deceleration Also referred to as terminal swing. The period ranging from mid swing until heel contact (85% to 100%). Muscles slow the leg and stabilize the foot in preparation for the next heel strike.

Figure B.2 shows the muscles fired to achieve the different events in the gait cycle.

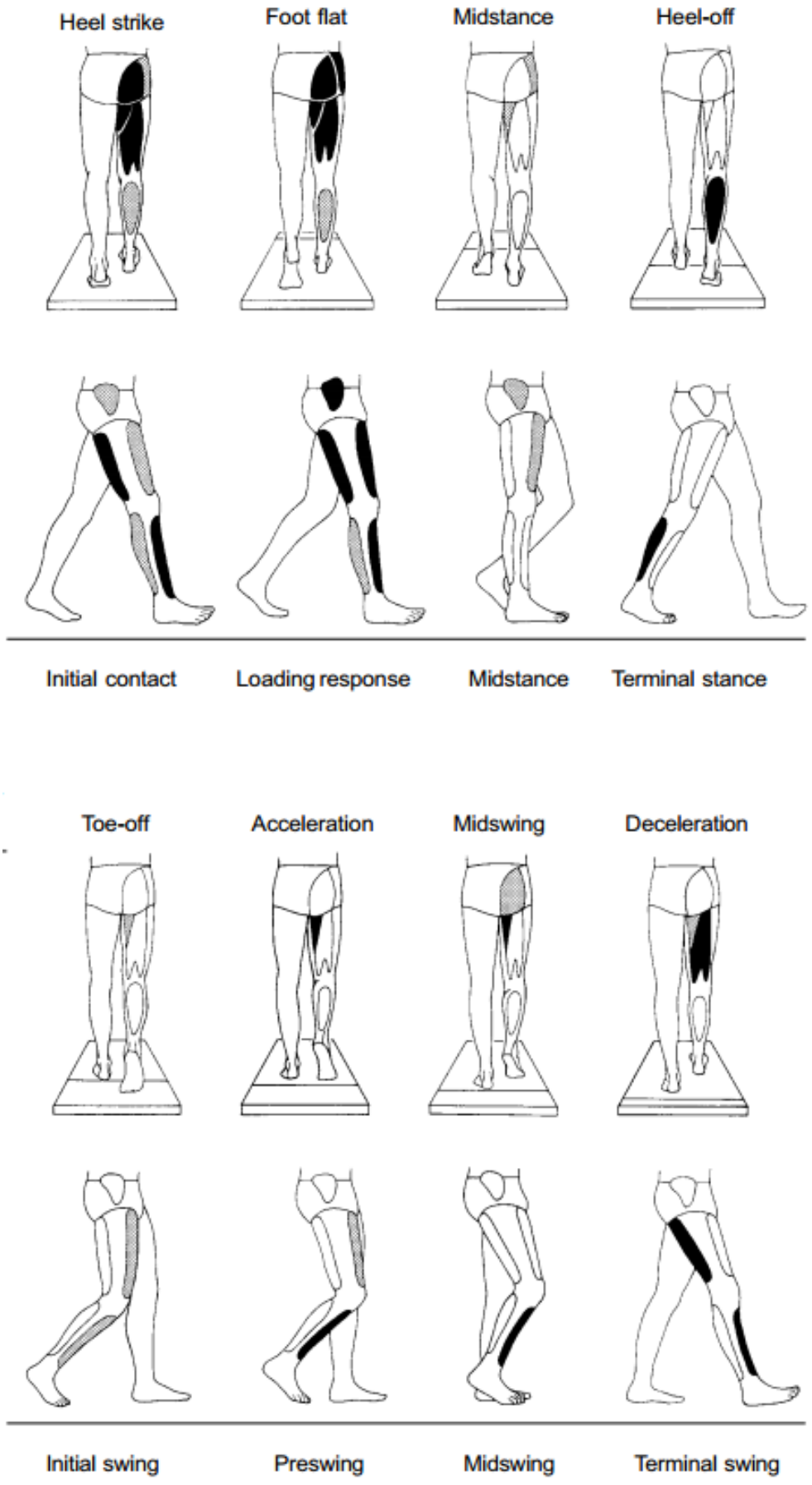

Figure B.2: Grey scaled activation levels of different muscle groups in the lower body during the gait cycle. From Vaughan et al. (1999)

Appendix C

Power Consumption

Due to circumstances (corona virus), I was unable to record the power usage of the system. To provide some clarity the following deriviations look to shine some light on the power consumption of the system. As previously mentioned a 5V battery supplies the Myrio controller, where the control signal is produced. Another 12V supply is used by the optically isolated DC-DC converter, increaseing the input pattern to a muscle stimulating level (120V, at 140mA).

Due to the nature of the signal (PWM), power is only supplied during the active region of the duty cycle. Note that the duty cycle is the controlled parameter, and is varied during operation ($0\mu \leq u \leq 300\mu$), for simplisity an average value of 250μ is used. The percentage value for which the signal is active can be calulcated as follows;

$$D = \frac{D_{active}}{1/F}, \tag{C.1}$$

$$D = \frac{250 \times 10^{-6}}{1/40} = 0.01, \tag{C.2}$$

where F is frequency, $1/F$ is the period of one cycle, and D is the percentage the signal is active for.

The power consumed by the system is given by,

$$P = (I \times V) \times D, \tag{C.3}$$

$$P = 140 \times 10^{-3} \times 120 \times 0.01 = 0.168W. \tag{C.4}$$

Note this doesnt include power loss within the circuit or during the voltage transformation.

Appendix D

Additional Controller Data

Experimental trials with healthy individuals were undertaken to evaluate the effectiveness of the designed RC schemes. Following ethical approval (ERGO/FPSE/47517), five participants were recruited for this study. Participants ranged from 20 to 35 years old and included male and females. Participant 1 and 5 had experienced/partaken in FES studies before, while participants 2, 3 and 4 had not. The participants were asked to sit on an elevated stool, thus leaving the leg able to swing freely.

To limit the effects of fatigue, there was a 20-minute break between each test, allowing the muscles to recover (Graham and Popovic, 2005). To limit the impact of model uncertainty, all tests for a given participant, were conducted in a single session, using the same initial model and pad position.

The voltage is tuned to the participant's comfort at the beginning of each experiment. This is done by slowly increasing the voltage level of the PWM (with the maximum pulse width length applied) until a sufficient range of motion is achieved or when the participant finds the sensation uncomfortable. To reduce the time spent in the muscle recruitment deadzone, the first cycle of the control update is set to the initial twitch value of the participant, and pulse width is constrained within the commonly used region, $0 \leq u \leq 300$, ensuring comfortable use (Wederich et al., 2000).

Chapter 6 discusses the procedures in detail, as well as exploring the experimental findings.

Note, the experiment was drawn short for participant 5 as they reported high levels of fatigue. This was attributed to the high levels of physical activity of the participant.

D.1 Participant 1

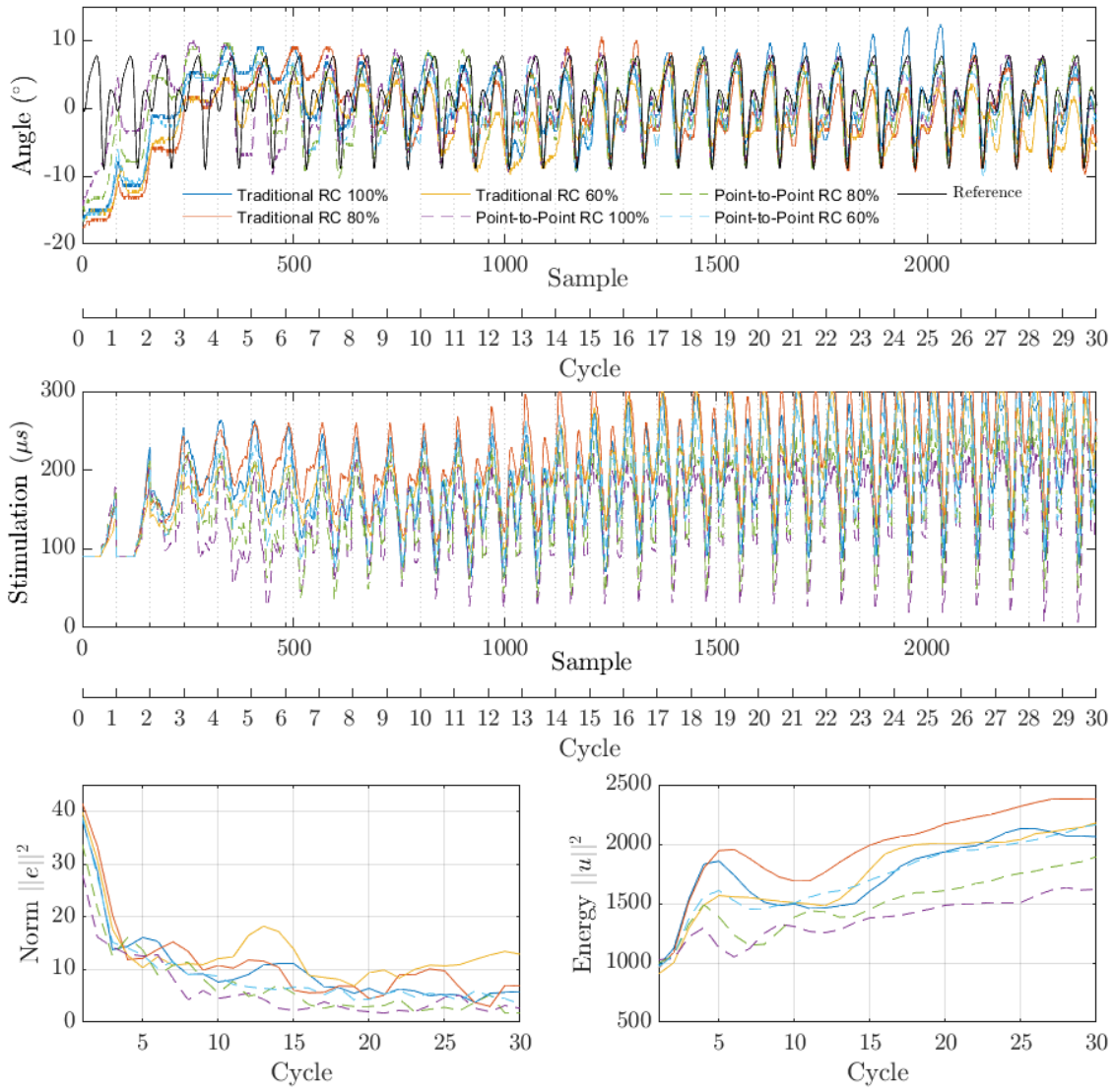

Figure D.1: Participant 1. Top: dorsiflexion outputs, middle: stimulation inputs, bottom left: error norm bottom right: minimum energy, for traditional and point-to-point RC.

D.2 Participant 2

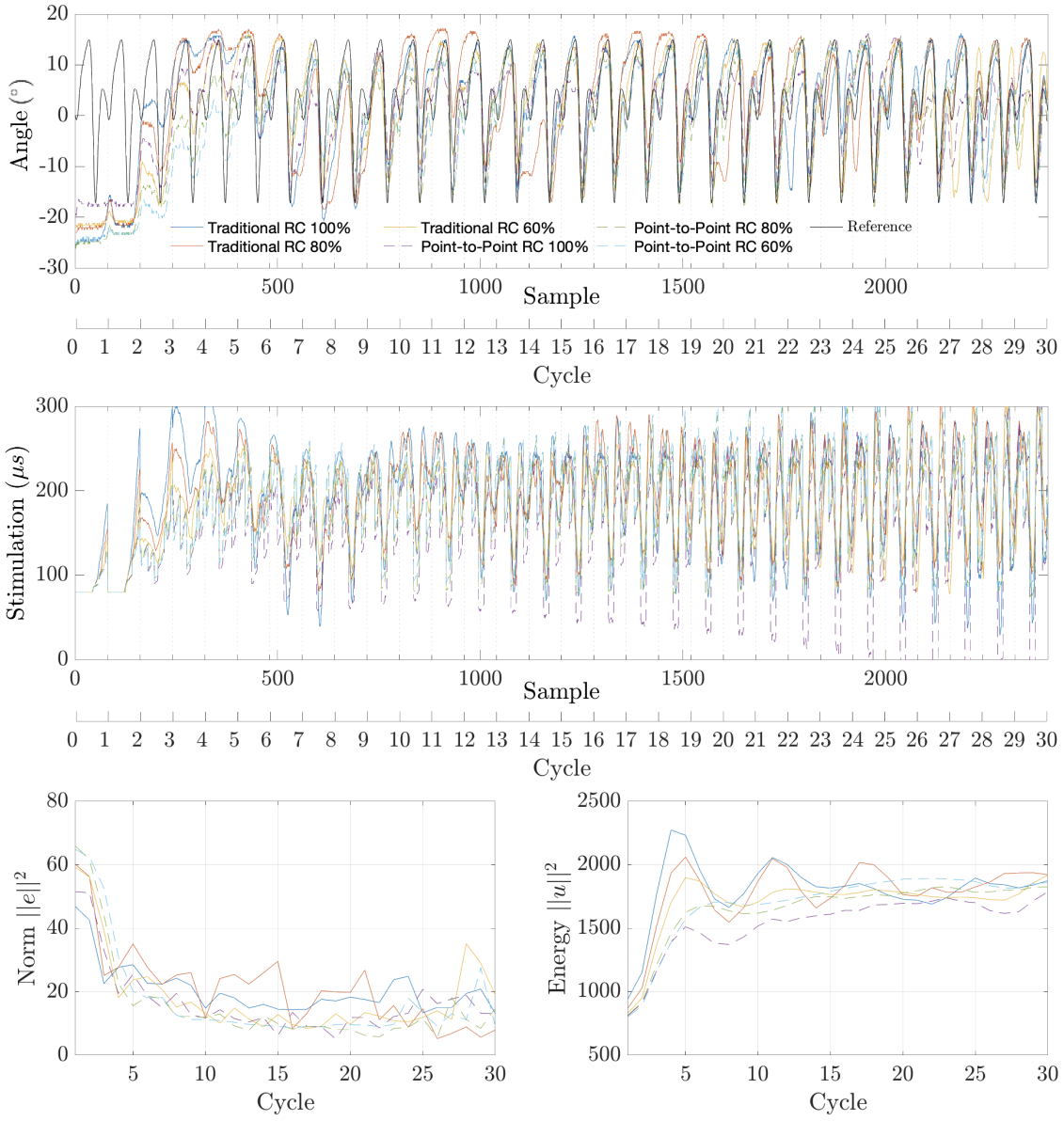

Figure D.2: Participant 2. Top: dorsiflexion outputs, middle: stimulation inputs, bottom left: error norm bottom right: minimum energy, for traditional and point-to-point RC.

D.3 Participant 3

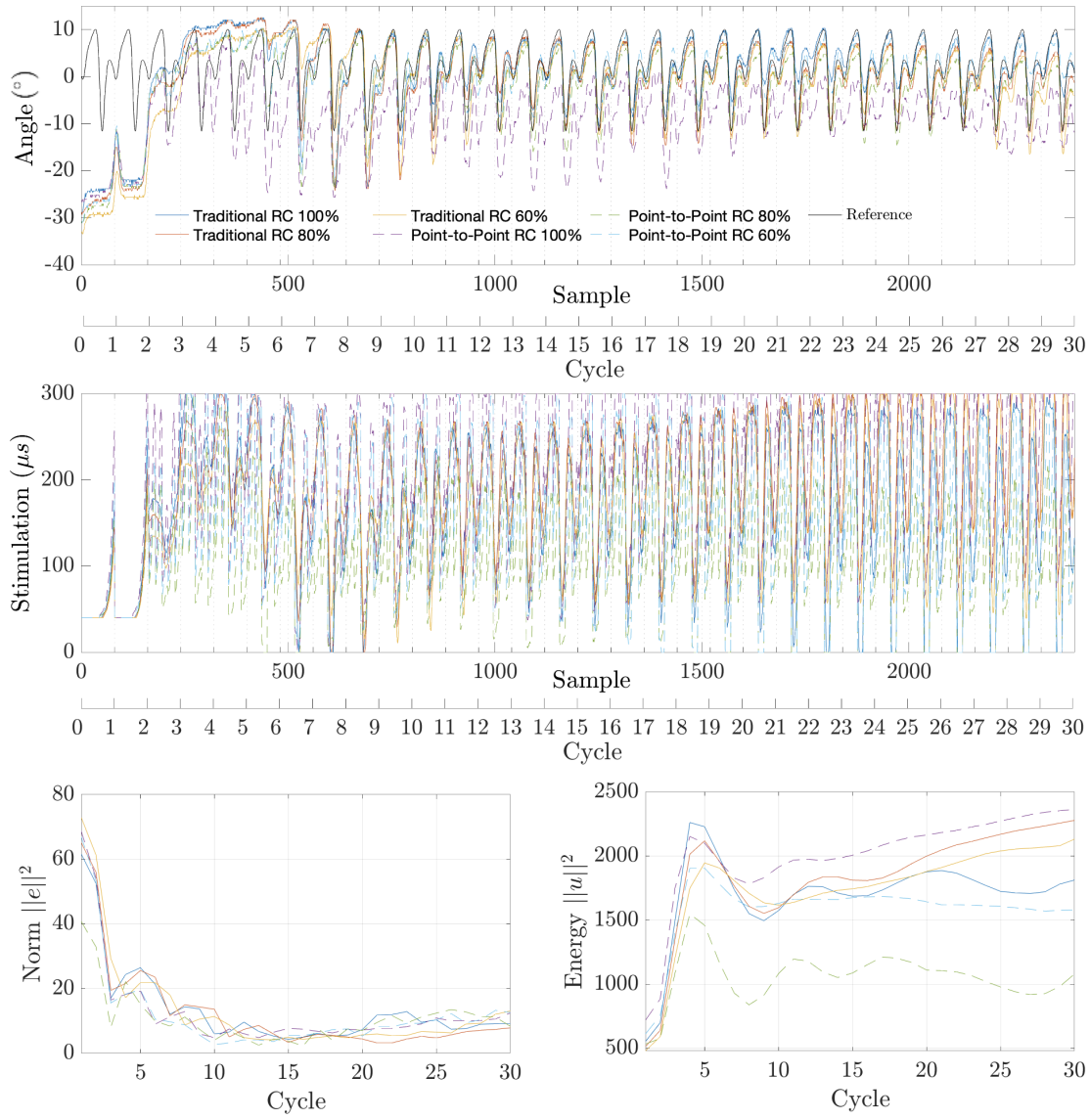

Figure D.3: Participant 3. Top: dorsiflexion outputs, middle: stimulation inputs, bottom left: error norm bottom right: minimum energy, for traditional and point-to-point RC.

D.4 Participant 4

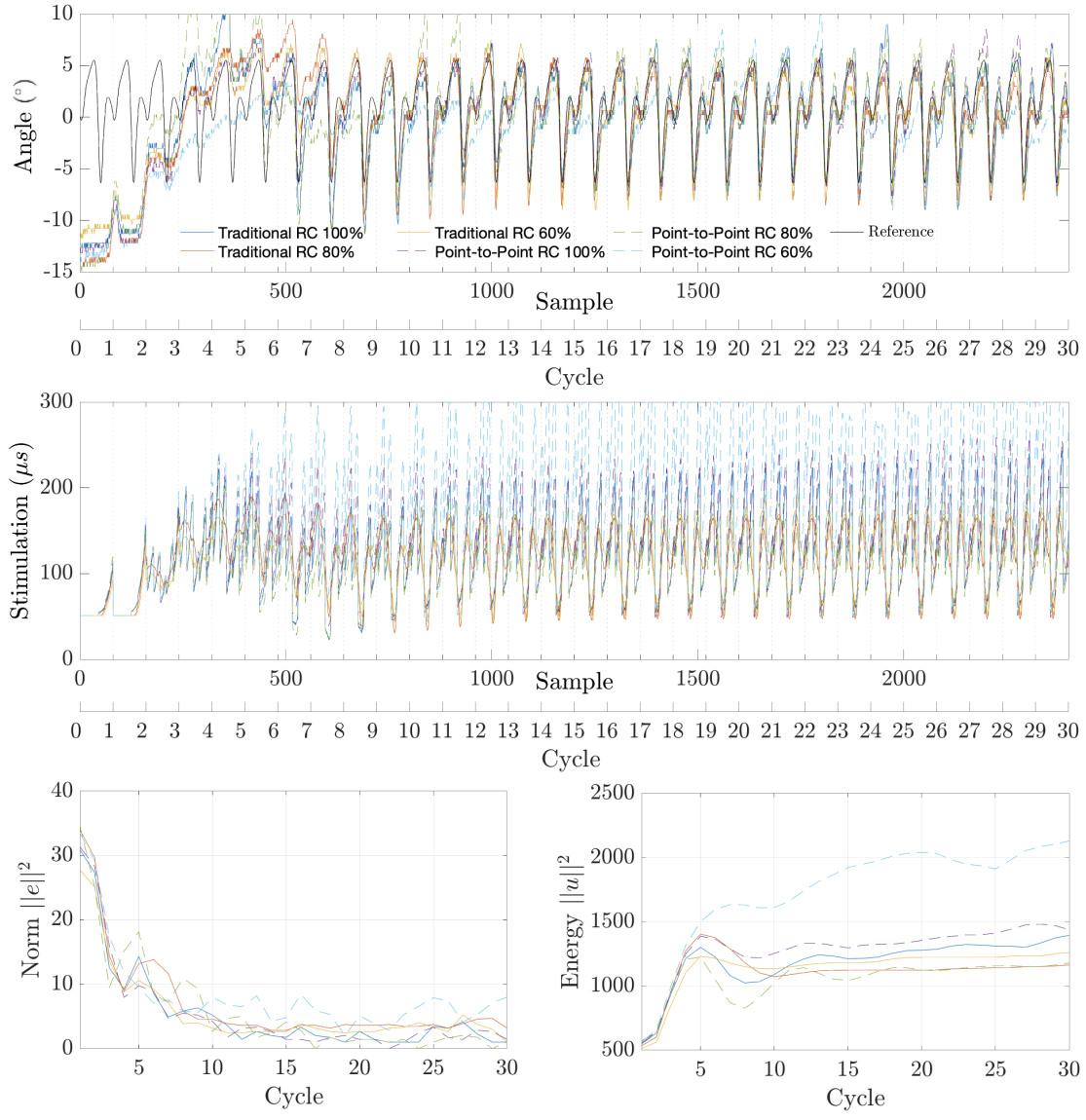

Figure D.4: Participant 4. Top: dorsiflexion outputs, middle: stimulation inputs, bottom left: error norm bottom right: minimum energy, for traditional and point-to-point RC.

D.5 Participant 5

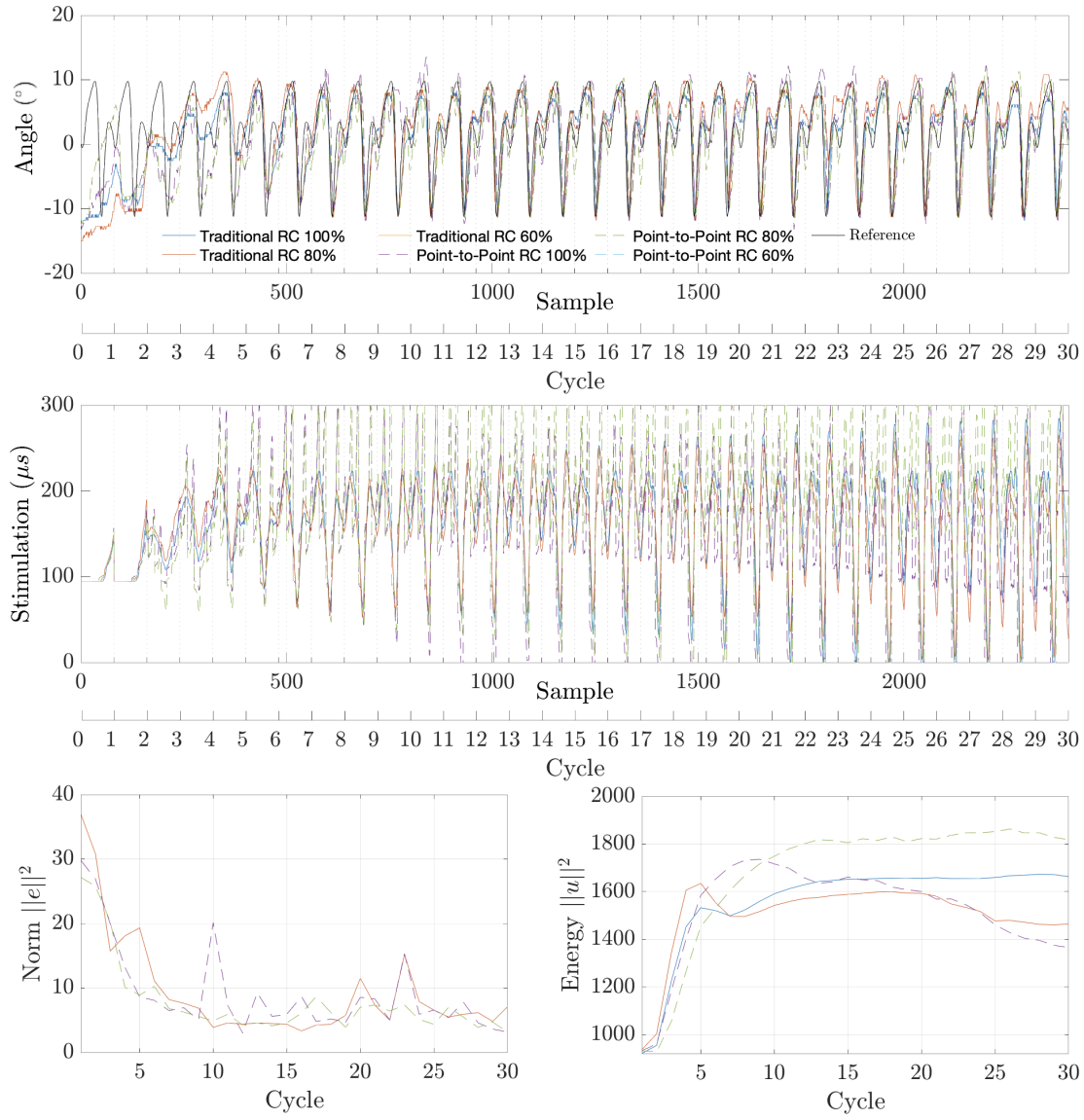

Figure D.5: Participant 5. Top: dorsiflexion outputs, middle: stimulation inputs, bottom left: error norm bottom right: minimum energy, for traditional and point-to-point RC.

Appendix E

Pad Pattern Data

Following ethical approval (ERGO/FPSE/47517), three unimpaired participants were recruited for the multi-pad pattern experiments. Participant 1 and 3 had experienced/-partaken in FES studies before, while participant 2 had not. The participants were asked to sit on an elevated stool, thus leaving the leg able to swing freely.

First, the voltage was tuned to be within the range of the participant's comfort. This was done by slowly increasing the voltage level of the PWM (with the maximum pulse width length applied) until a sufficient range of motion is achieved or when the participant finds the sensation uncomfortable. The pulse width was constrained within the commonly used region, $0 \leq u \leq 300$, ensuring comfortable use (Wederich et al., 2000). To limit the effects of fatigue, there was a 20-minute break between each test, allowing the muscles to recover (Graham and Popovic, 2005).

Chapter 7 discusses the procedures in detail, as well as exploring the experimental findings.

E.1 Participant 1

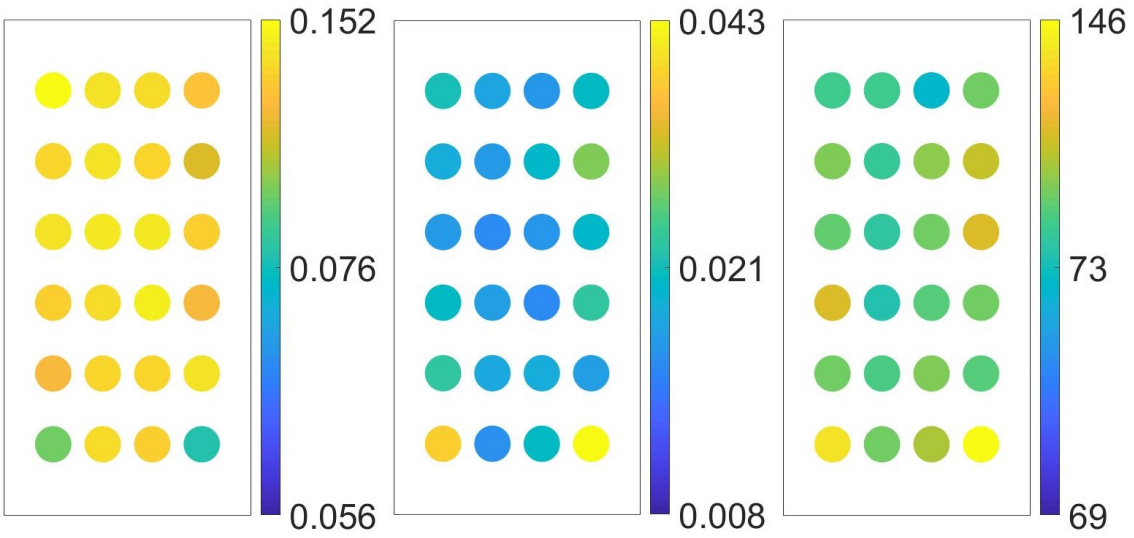

Figure E.1: Participant 1: dorsiflexsion gradients, eversion gradients ($\theta/\mu s$), and twitch threshold (μs) values for each pad.

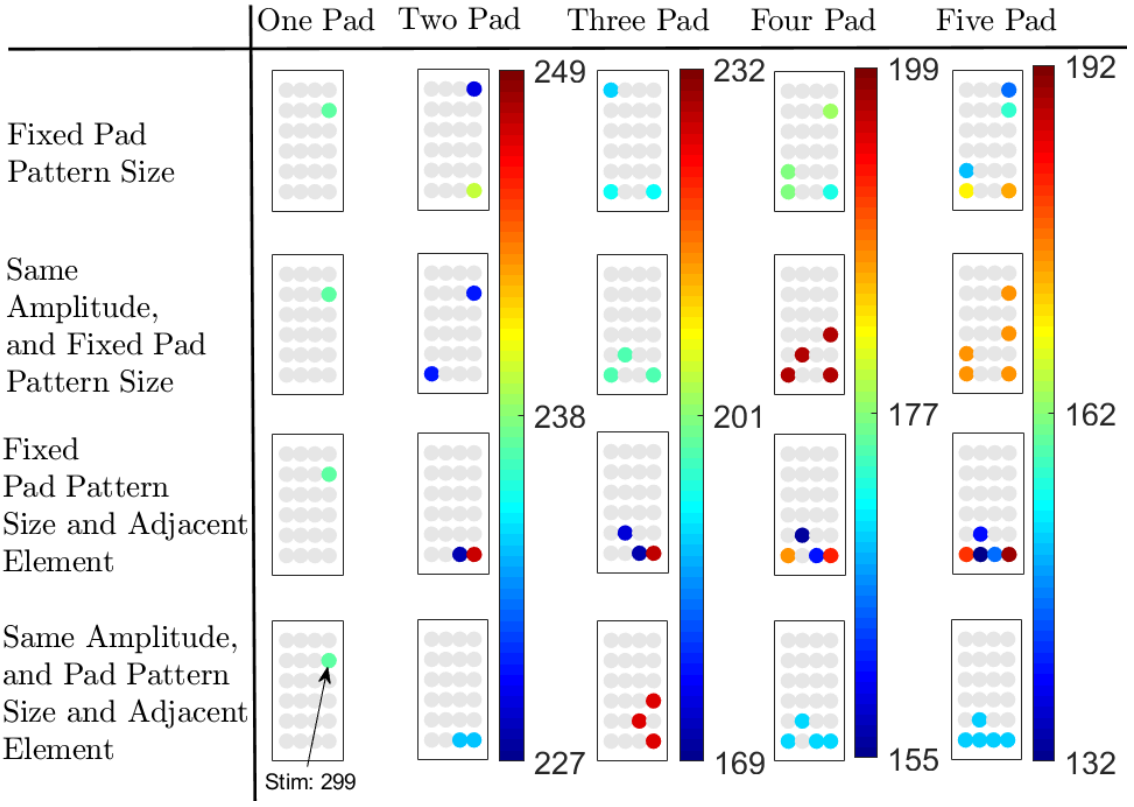

Figure E.2: Participant 1: optimal pad patterns for each constraint, with stimulation levels (μs) in grouped columns.

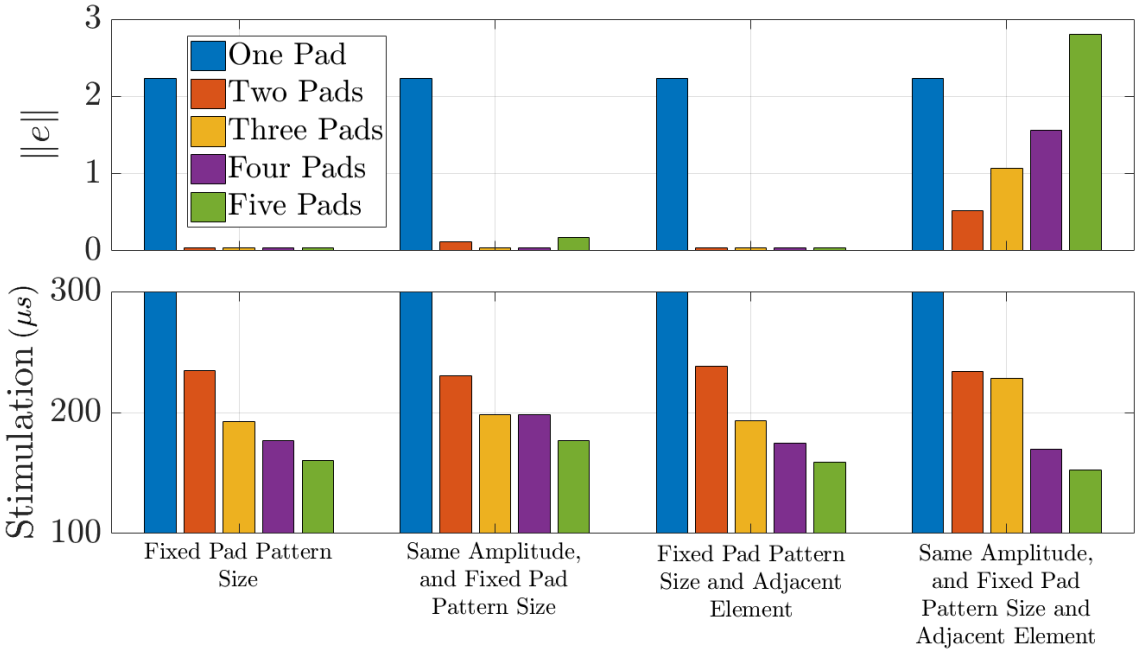

Figure E.3: Participant 1: simulation results.

Constraint	Number of Pads	Simulation		Experimental		
		Stimulation	Error	Dorsiflexsion	Roll	Error
Fixed Pad Pattern Size	1	299	2.24	27.4 ± 0.17	1.77 ± 0.09	12.63 ± 0.26
	2	234 ± 5.5	0.04	22.85 ± 0.36	3.33 ± 0.02	6.52 ± 0.38
	3	192 ± 1.89	0.04	25.36 ± 0.47	2.2 ± 0.08	10.16 ± 0.55
	4	176 ± 25.9	0.04	22.6 ± 1.66	3.93 ± 0.83	5.67 ± 2.49
	5	160 ± 11.45	0.04	20.96 ± 1.15	4.3 ± 0.26	3.66 ± 1.41
Same Amplitude, Fixed Pad Pattern Size	1	299	2.24	27.38 ± 0.62	2.42 ± 0.33	11.96 ± 0.96
	2	230	0.12	25.71 ± 0.52	2.75 ± 0.21	9.96 ± 0.73
	3	198	0.04	23.4 ± 0.67	3.46 ± 0.33	6.94 ± 1.00
	4	177	0.17	22.25 ± 0.92	3.54 ± 0.29	5.71 ± 1.21
	5	158	0.79	19.15 ± 0.38	4.87 ± 0.11	2.98 ± 0.49
Fixed Pad Pattern Size, and Adjacent Element	1	299	2.24	26.67 ± 0.51	3.21 ± 0.48	10.46 ± 1.00
	2	238 ± 10.5	0.04	14.67 ± 1.89	3.21 ± 0.48	9.12 ± 2.33
	3	193 ± 27.35	0.04	21.28 ± 1.78	6.27 ± 0.44	2.01 ± 2.14
	4	175 ± 16.19	0.04	23.02 ± 0.54	3.62 ± 0.19	6.4 ± 0.73
	5	158 ± 23.7	0.04	23.63 ± 4.42	4.49 ± 0.2	6.14 ± 4.62
Same Amplitude, Fixed Pad Pattern Size and Adjacent Element	1	299	2.24	27.51 ± 0.14	2.33 ± 0.13	12.18 ± 0.27
	2	234	0.52	27.08 ± 0.58	2.22 ± 0.4	11.86 ± 0.98
	3	185	1.82	21.58 ± 0.8	4.35 ± 0.22	4.23 ± 1.02
	4	170	1.56	20.46 ± 0.59	4.63 ± 0.17	2.83 ± 0.76
	5	152	2.81	19.44 ± 0.67	5.3 ± 0.59	2.26 ± 1.26

Table E.1: Participant 1: simulation and experimental data

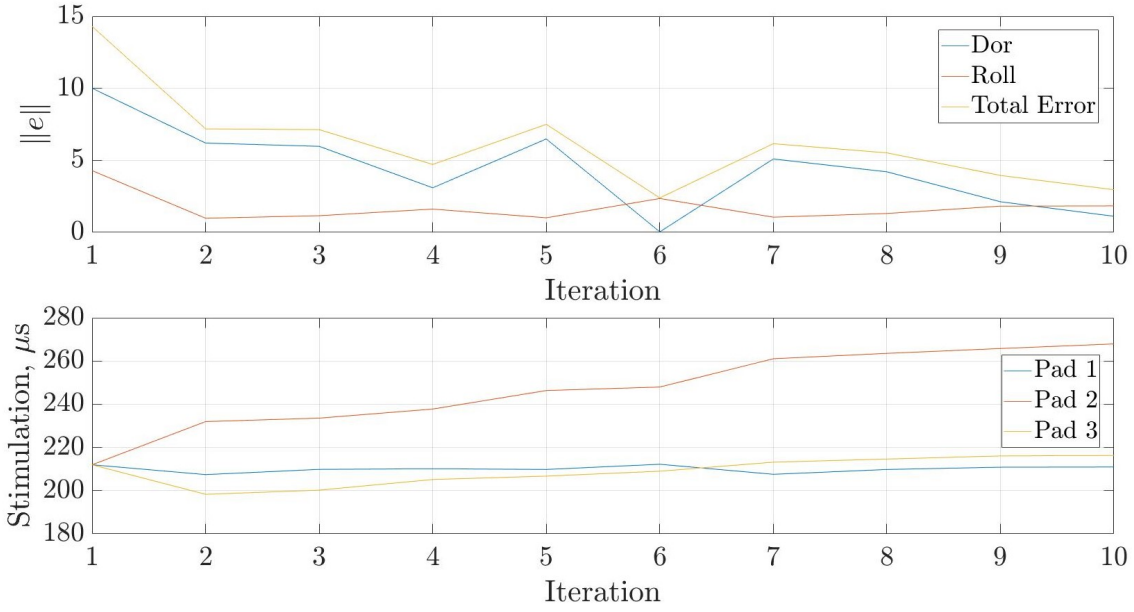

Figure E.4: Participant 1: experimental real-time ILC, using Fixed Pad Pattern Size constraint.

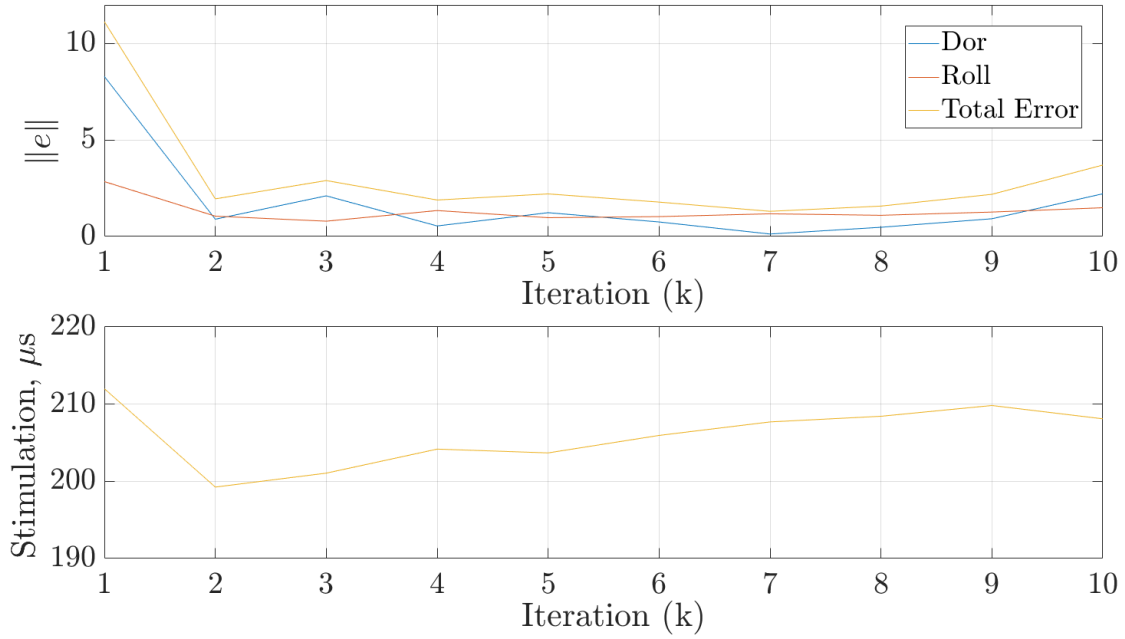

Figure E.5: Participant 1: experimental, real-time ILC, using the Same Stimulation Amplitude Fixed Pad Pattern Size constraint.

E.2 Participant 2

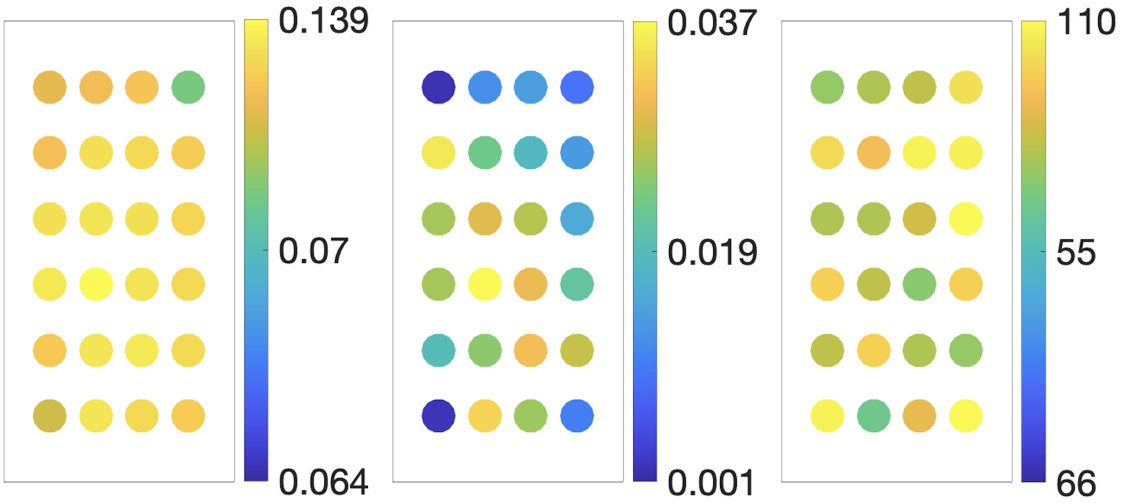

Figure E.6: Participant 2: dorsiflexsion gradients, eversion gradients ($\theta/\mu s$), and twitch threshold (μs) values for each pad.

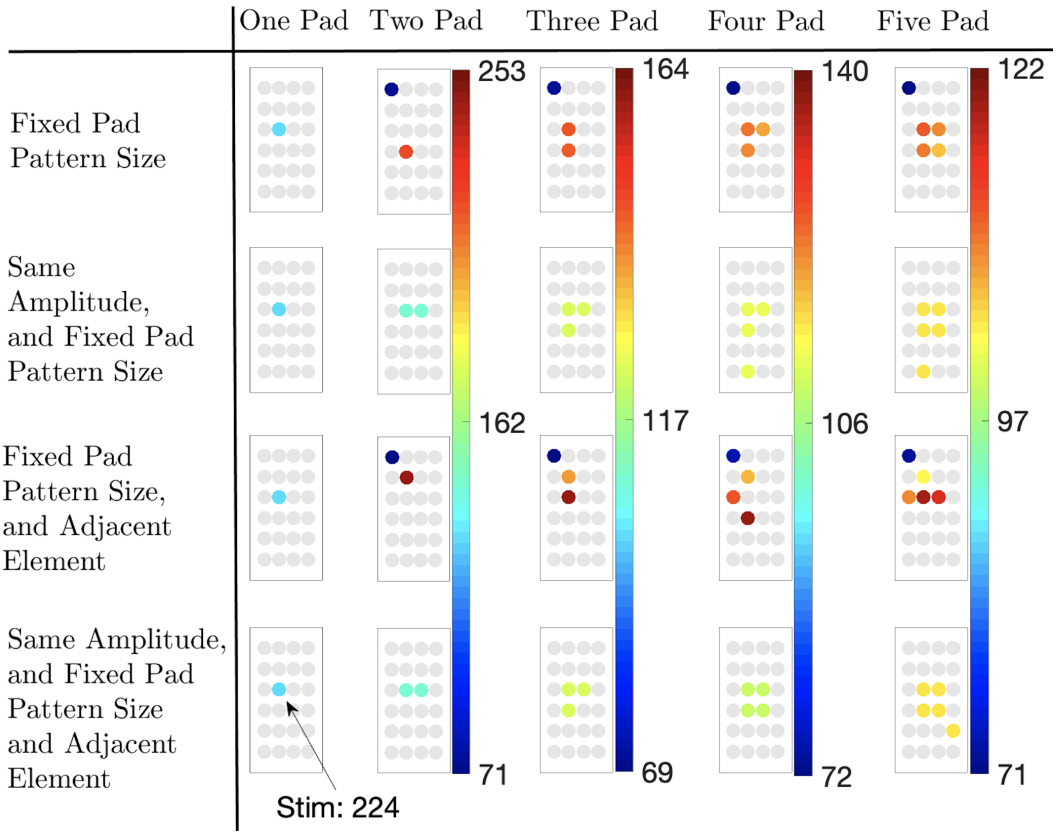

Figure E.7: Participant 2: optimal pad patterns for each constraint, with stimulation levels (μs) in grouped columns.

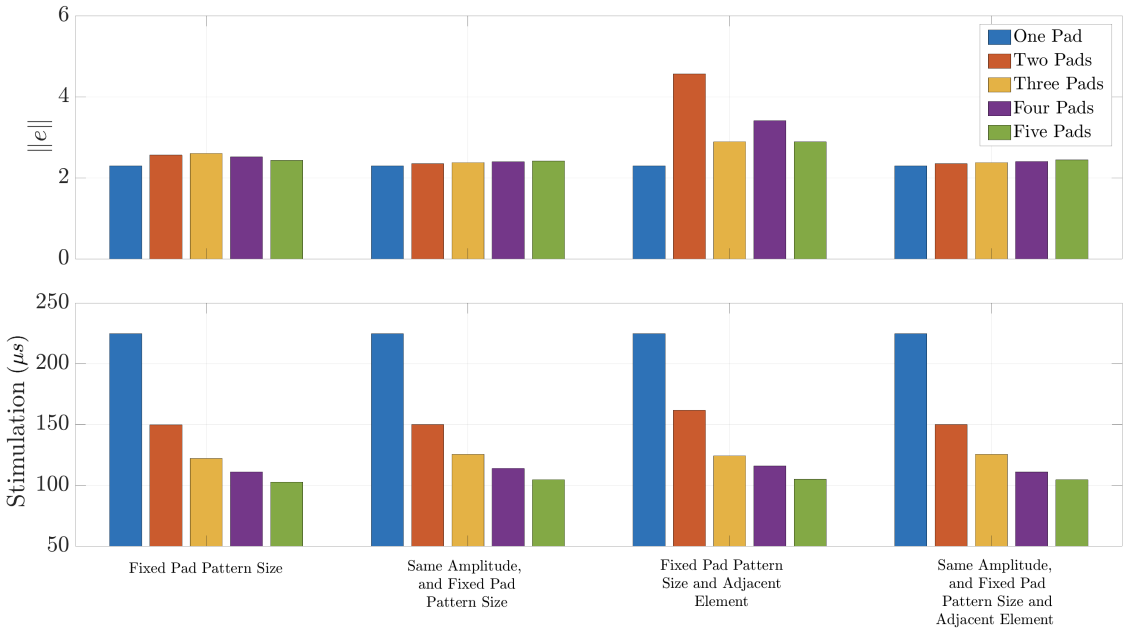

Figure E.8: Participant 2: simulation results.

Constraint	Number of Pads	Simulation		Experimental		
		Stimulation	Error	Dorsiflexsion	Roll	Error
Fixed Pad Pattern Size	1	224 ± 0	2.29	28.60 ± 0.32	5.71 ± 0.43	9.89 ± 0.75
	2	149 ± 75	4.56	23.86 ± 0.49	4.00 ± 0.12	6.86 ± 0.61
	3	121 ± 35	4.93	26.09 ± 0.45	1.99 ± 0.2	11.09 ± 0.65
	4	110 ± 22	3.41	20.24 ± 0.45	1.87 ± 0.33	5.37 ± 0.78
	5	102 ± 15	2.89	12.93 ± 0.76	1.59 ± 0.72	12.48 ± 1.48
Same Amplitude, Fixed Pad Pattern Size	1	224	2.29	27.64 ± 0.66	5.55 ± 0.32	9.09 ± 0.98
	2	149	2.34	23.42 ± 0.82	1.06 ± 0.1	9.36 ± 0.92
	3	125	2.37	18.84 ± 0.21	3.01 ± 0.99	5.51 ± 1.20
	4	114	2.40	13.12 ± 0.46	4.17 ± 0.05	9.71 ± 0.51
	5	104	2.44	12.08 ± 0.29	4.49 ± 0.16	10.43 ± 0.45
Fixed Pad Pattern Size, and Adjacent Element	1	224	2.29	29.16 ± 0.10	6.47 ± 0.08	9.69 ± 0.18
	2	161 ± 90	2.56	30.70 ± 0.26	6.04 ± 0.24	11.65 ± 0.50
	3	123 ± 39	2.60	20.90 ± 0.94	3.52 ± 0.66	4.38 ± 1.60
	4	115 ± 24	2.52	15.84 ± 1.21	0.55 ± 0.17	10.6 ± 1.38
	5	104 ± 17	2.43	14.98 ± 0.63	4.58 ± 0.17	7.44 ± 1.02
Same Amplitude, Fixed Pad Pattern Size and Adjacent Element	1	224	2.29	26.30 ± 0.17	7.99 ± 0.48	7.29 ± 0.64
	2	149	2.34	16.99 ± 0.30	2.71 ± 0.52	7.30 ± 0.82
	3	125	2.37	14.70 ± 0.47	3.59 ± 0.69	8.71 ± 1.16
	4	114	2.39	12.03 ± 1.10	4.61 ± 0.18	10.36 ± 1.27
	5	104	2.41	11.35 ± 0.78	4.47 ± 0.07	11.18 ± 0.84

Table E.2: Participant 2: simulation and experimental data

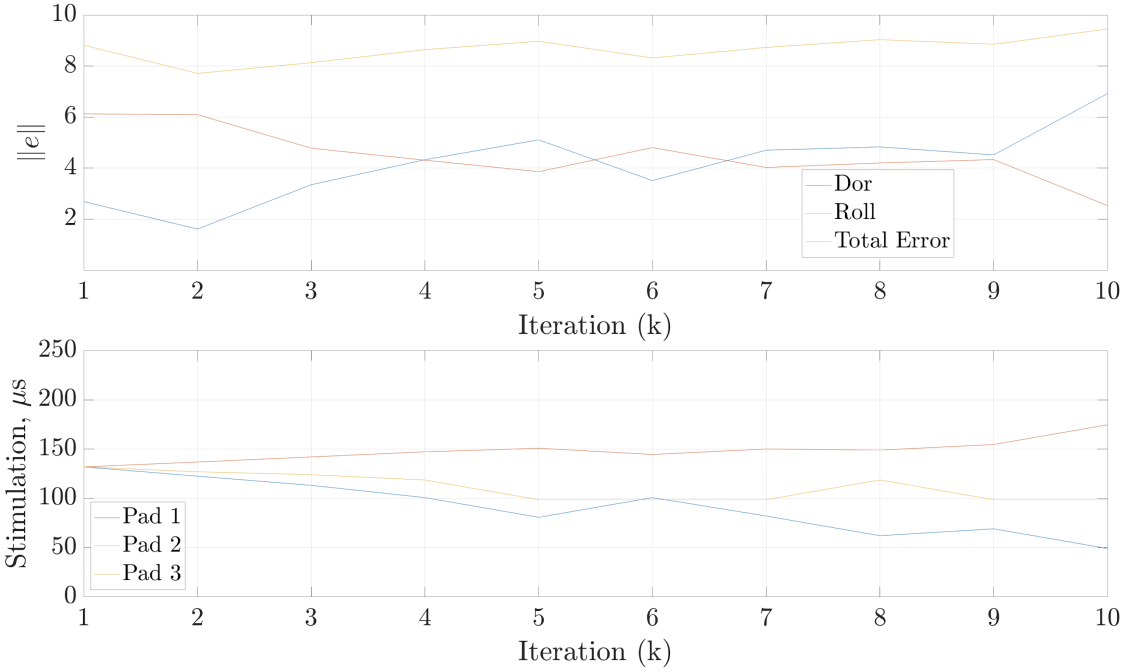

Figure E.9: Participant 2: experimental real-time ILC, using Fixed Pad Pattern Size constraint.

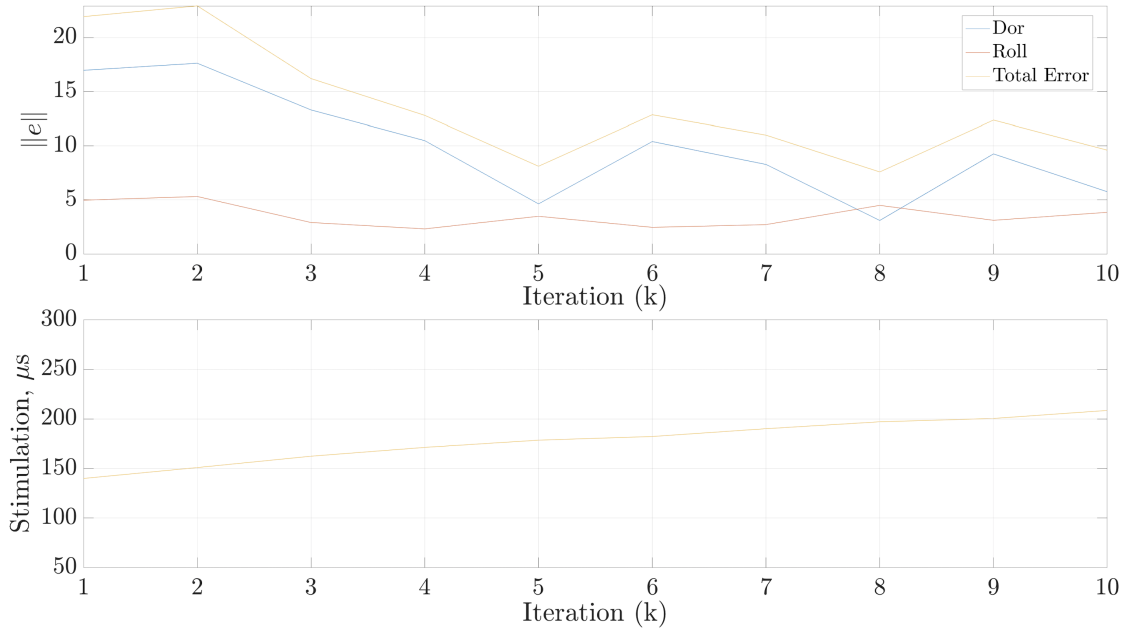

Figure E.10: Participant 2: experimental, real-time ILC, using Same Stimulation Amplitude Fixed Pad Pattern Size constraint.

E.3 Participant 3

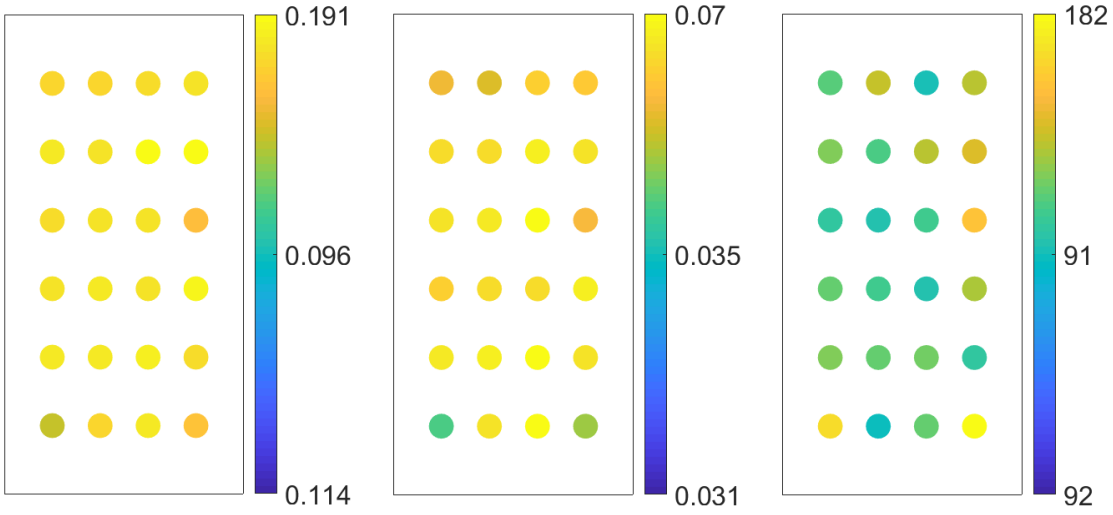

Figure E.11: Participant 3: dorsiflexsion gradients, eversion gradients ($\theta/\mu s$), and twitch threshold (μs) values for each pad.

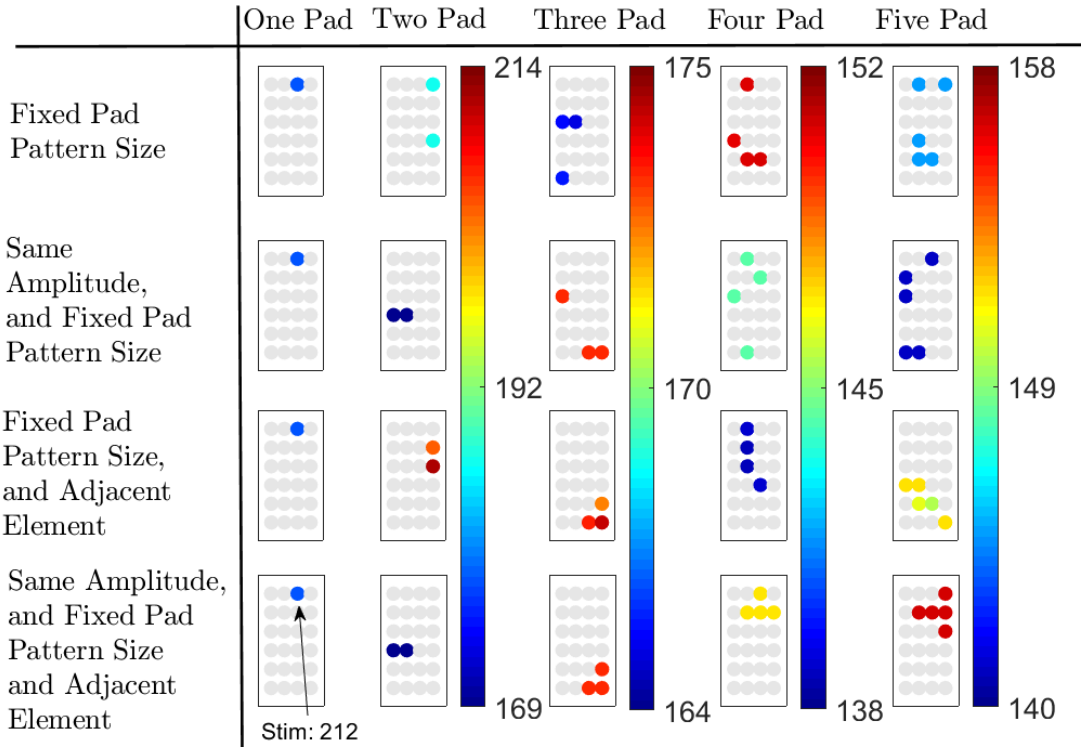

Figure E.12: Participant 3: optimal pad patterns for each constraint, with stimulation levels (μs) in grouped columns.

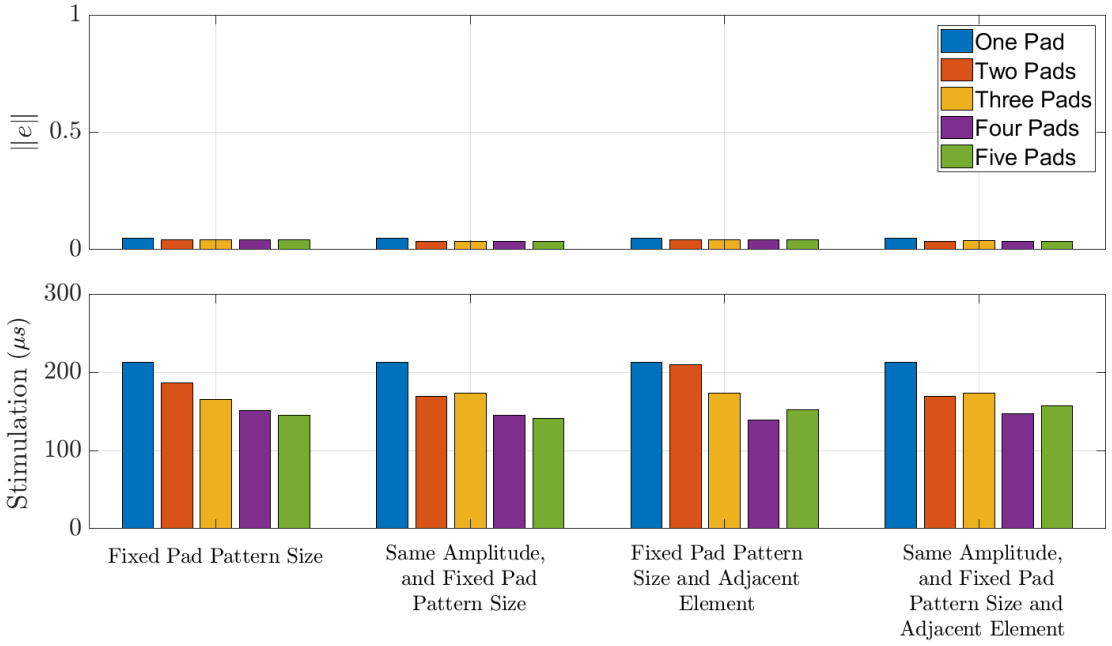

Figure E.13: Participant 3: simulation results.

Constraint	Number of Pads	Simulation		Experimental		
		Stimulation	Error	Dorsiflexsion	Roll	Error
Fixed Pad Pattern Size	1	212	0.05	22.92 ± 0.47	8.42 ± 0.09	4.33 ± 0.56
	2	187	0.04	27.05 ± 0.23	8.91 ± 0.06	8.96 ± 0.3
	3	165	0.04	28.16 ± 0.85	10.79 ± 0.15	11.95 ± 0.99
	4	151	0.04	27.80 ± 0.76	9.47 ± 1.18	10.27 ± 1.94
	5	145	0.04	28.69 ± 0.94	11.70 ± 1.28	13.40 ± 2.22
Same Amplitude, Fixed Pad Pattern Size	1	212	0.05	25.64 ± 0.39	9.47 ± 1.18	8.11 ± 1.05
	2	169	0.04	32.29 ± 0.84	11.01 ± 4.74	6.970 ± 5.57
	3	173	0.03	32.14 ± 1.03	13.43 ± 0.32	18.57 ± 1.35
	4	144	0.04	30.68 ± 0.05	13.84 ± 0.35	17.52 ± 0.4
	5	140	0.04	30.01 ± 0.59	12.02 ± 0.79	15.03 ± 1.39
Fixed Pad Pattern Size, and Adjacent Element	1	212	0.04	27.13 ± 1.07	10.54 ± 0.2	10.67 ± 1.27
	2	209 ± 4	0.04	30.90 ± 0.17	14.13 ± 0.34	18.03 ± 0.52
	3	173 ± 0.82	0.04	21.68 ± 1.03	5.82 ± 0.46	2.85 ± 1.49
	4	139	0.04	31.10 ± 0.85	11.15 ± 0.48	15.24 ± 1.33
	5	151 ± 0.98	0.04	32.78 ± 0.83	14.83 ± 0.44	20.62 ± 1.27
Same Amplitude, Fixed Pad Pattern Size and Adjacent Element	1	212	0.05	26.39 ± 0.65	12.00 ± 1.02	11.39 ± 1.67
	2	169	0.04	31.75 ± 0.22	15.50 ± 0.24	20.25 ± 0.46
	3	173	0.04	31.13 ± 0.98	14.46 ± 1.3	18.60 ± 2.28
	4	147	0.04	23.90 ± 0.34	9.54 ± 0.83	6.44 ± 1.17
	5	157	0.04	26.63 ± 1.46	11.93 ± 1.34	11.56 ± 2.8

Table E.3: Participant 3: simulation and experimental data

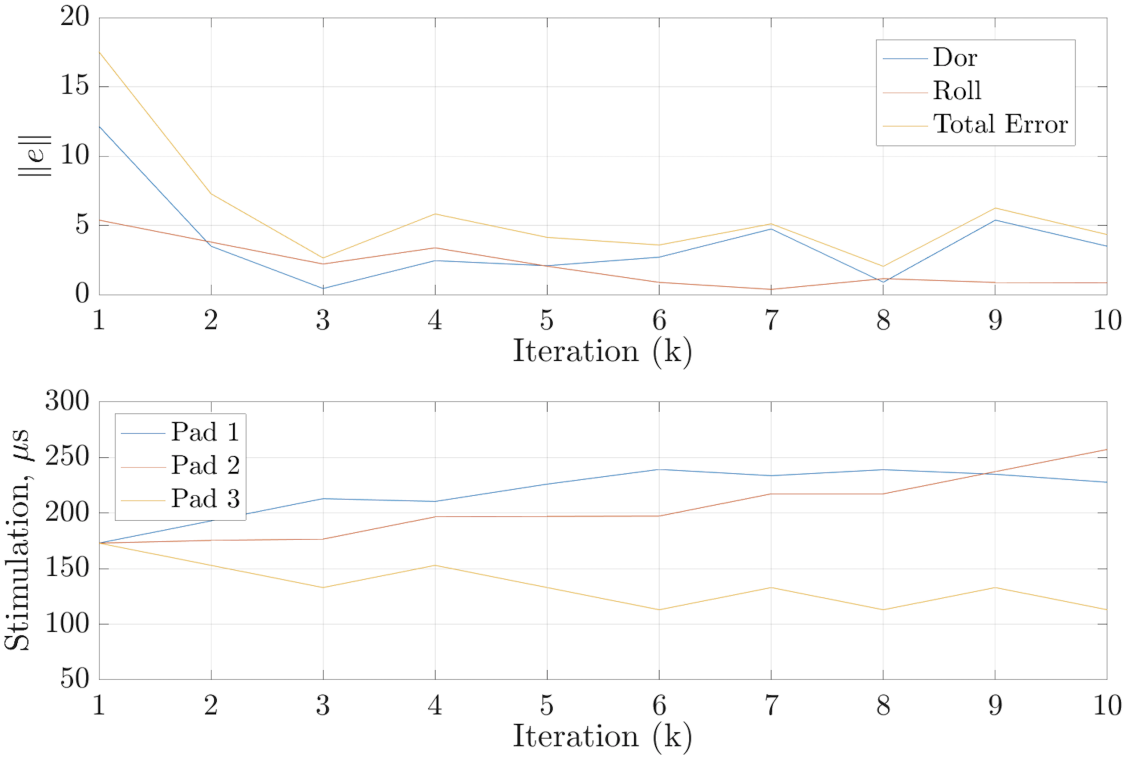

Figure E.14: Participant 3: experimental real-time ILC, using Fixed Pad Pattern Size constraint.

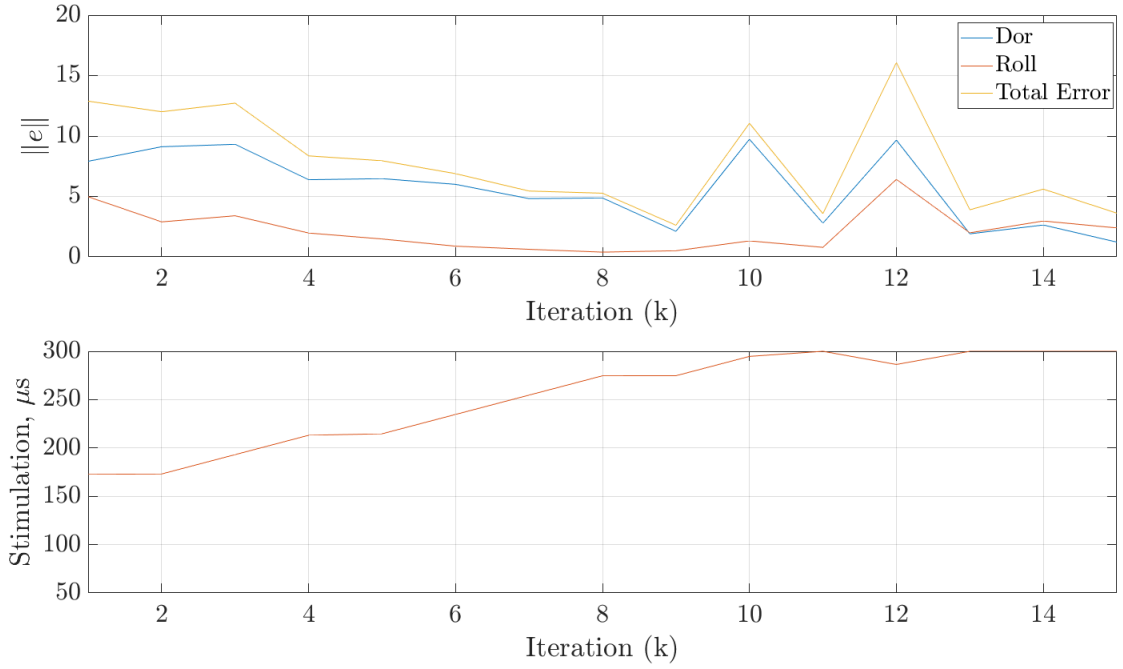

Figure E.15: Participant 3: experimental, real-time ILC, using Same Stimulation Amplitude Fixed Pad Pattern Size constraint.

References

A. Assalone, G. Pin, and T. Parisini. Kernel-based continuous-time identification of hammerstein models: Application to the case of ankle joint stiffness dynamics. In *IEEE International Conference on Rehabilitation Robotics*, pages 2015–2020, 2015.

C. L. Barrett and P. N. Taylor. The effects of the Odstock drop foot Stimulator on perceived quality of life for people with stroke and multiple sclerosis. *Neuromodulation*, 13(1):58–64, 2010.

O. W. Brend, C. T. Freeman, and M. French. Multiple model adaptive control of functional electrical stimulation. *IEEE Transactions on Control System Technology*, 23(5):1901–1913, 2015.

D. A. Bristow, M. Tharayil, and A. G. Alleyne. A survey of iterative learning control a learning-based method for high-performance tracking control. *IEEE Control Systems Magazine*, 26(3):96–114, 2006.

L. Buentjen, A. Kupsch, I. Galazky, R. Frantsev, H. Heinze, J. Voges, J. Hausmann, and C. Sweeney-Reed. Long-term outcomes of semi-implantable functional electrical stimulation for central drop foot. *Journal of NeuroEngineering and Rehabilitation*, 16, 12 2019.

J. Bullock, J. Boyle and M. B. Wang. *Physiology (4th ed.)*. Lippincott Williams and Wilkins., 2001.

Y. Chen, S. Chen, W. Chen, C. Hsiao, T. Kuo, and J. Lai. Neural network and fuzzy control in fes-assisted locomotion for the hemiplegic. *Journal of Medical Engineering & Technology*, 28(1):32–38, 2004.

T. P. Chenal, J. C. Case, J. Paik, and R. K. Kramer. Variable stiffness fabrics with embedded shape memory materials for wearable applications. In *IEEE/RSJ International Conference on Intelligent Robots and Systems*, pages 2827–2831, 2014.

E. Copur, C. Freeman, B. Chu, and D. laila. Repetitive Control of Electrical Stimulation for Tremor Suppression. *IEEE Transactions on Control Systems Technology*, 2017.

A. Crema, N. Malesevic, I. Furfaro, F. Raschella, A. Pedrocchi, and S. Micera. A Wearable Multi-Site System for NMES-Based Hand Function Restoration. *IEEE Transactions on Neural Systems and Rehabilitation Engineering*, 26(2):428–440, Feb 2018.

A. M. Dollar and H. Herr. Lower extremity exoskeletons and active orthoses: challenges and state-of-the-art. *IEEE Transactions on Robotics*, 24(1):144–158, 2008.

W. K. Durfee and K. E. MacLean. Methods for estimating isometric recruitment curves of electrically stimulated muscle. *IEEE Transactions on Biomedical Engineering*, 36 (7):654–667, July 1989.

W. K. Durfee and K. I. Palmer. Estimation of force-activation, force-length and force-velocity properties in isolated, electrically stimulated muscle. *IEEE Transactions on Biomedical Engineering*, 41(3):205–216, 1994.

A. Dutta, A. Thondiyath, and A. Banerjee. Evaluation of an instrumented sleeve for myoelectrically-triggered functional electrical therapy: indo-german stroke study. In *The 2nd IASTED International Conference on Assistive Technologies*, S, 2012.

J. E. Esnouf, P. N. Taylor, G. E. Mann, and C. L. Barrett. Impact on activities of daily living using a functional electrical stimulation device to improve dropped foot in people with multiple sclerosis, measured by the Canadian Occupational Performance Measure. *Multiple Sclerosis*, 16:1141–1147, 2010.

D. G. Everaert, R. B. Stein, G. M. Abrams, A. W. Dromerick, G. E. Francisco, B. J. Hafner, T. N. Huskey, M. C. Munin, K. J. Nolan, and C. V. Kufta. Effect of a Foot-Drop Stimulator and Ankle–Foot Orthosis on Walking Performance After Stroke: A Multicenter Randomized Controlled Trial. *Neurorehabilitation and Neural Repair*, 27 (7):579–591, 2013.

R. J. Farris, H. A. Quintero, T. J. Withrow, and M. Goldfarb. Design of a joint-coupled orthosis for FES-aided gait. In *IEEE International Conference on Rehabilitation Robotics*, pages 246–252, 2009.

Z. Fenfang, G. Zhu, Y. H. Tsoi, and S. Xie. A computational biomechanical model of the human ankle for development of an ankle rehabilitation robot. In *IEEE/ASME 10th International Conference on Mechatronic and Embedded Systems and Applications*, pages 1–6, 2014.

M. Ferrarin, F. Palazzo, R. Riener, and J. Quintern. Model-Based Control of FES-Induced Single Joint Movements. *IEEE Transactions on Neural Systems and Rehabilitation Engineering*, 9(3):245–57, sep 2001.

E. M. Ficanha, G. A. Ribeiro, L. Knop, and M. Rastgaar. Time-varying impedance of the human ankle in the sagittal and frontal planes during straight walk and turning steps. In *International Conference on Rehabilitation Robotics*, pages 1413–1418, July 2017.

T. Flash and N. Hogan. The coordination of arm movements: An experimentally confirmed mathematical model. *Journal of Neuroscience*, 5:1688–1703, 1985.

Mayfair FootCare. Foot drop, 2018. URL http://www.mayfairfootcare.com/foot-drop.php.

S. Forghany, R. Jones, S. Preece, C. Nester, and S. Tyson. Early Observations of the Effects of Lateral Wedge Orthoses on Lower Limb Muscle Length and Potential for Exacerbating Spasticity. *Prosthetics and Orthotics International*, 34(3):319–326, 2010.

B. Forrester and J. Petrofsky. Effect of Electrode Size, Shape, and Placement During Electrical Stimulation. *The Journal of Applied Research*, 4, 01 2004.

B. Francis and W. Wonham. The Internal Model Principle of Control Theory. *Automatica*, 12:457–465, 09 1976a.

B. A. Francis and W. M. Wonham. The internal model principle of control theory. *Automatica*, 12(5):457 – 465, 1976b.

C. Freeman, M. Spraggs, A. Hughes, K. Yang, M.Tudor, and N. Grabham. Multiple model adaptive ILC for human movement assistance. *IFAC European Control Conference*, 12(15):6, June 2018.

C. T. Freeman. Electrode array-based electrical stimulation using ILC with restricted input subspace. *Control Engineering Practice*, 23(2):32–43, 2014.

C. T. Freeman. Multiple model switched repetitive control. In *IEEE Conference on Decision and Control*, 2017.

C. T. Freeman, A. M. Hughes, J. H. Burridge, P. H. Chappell, P. L. Lewin, and E. Rogers. A model of the upper extremity using FES for stroke rehabilitation. *ASME Journal of Biomechanical Engineering*, 131(3):031006–1–031006–10, 2009.

C. T. Freeman, P. Sampson, J. H. Burridge, and A. M. Hughes. Repetitive control of functional electrical stimulation for induced tremor suppression. *Mechatronics*, 32:79 – 87, 2015.

C. T. Freeman, K. Yang, J. Tudor, and M. Kutlu. Feedback Control of Electrical Stimulation Electrode Arrays. *Medical Engineering and Physics*, doi:10.1016/j.medengphy.2016.07.002, 2016. doi: doi:10.1016/j.medengphy.2016.07.002.

J. Goodman. Grocery shopping: who, where and when, 2016.

A. Thrasher G. Graham and M. Popovic. Reducing Muscle Fatigue Due to Functional Electrical Stimulation Using Random Modulation of Stimulation Parameters. *Artificial Organs*, 29(6):453–458, 2005.

J. Graham. Foot drop: Explaining the causes, characteristics and treatment. *British Journal of Neuroscience Nursing*, 6(4):168–172, 2010.

J. J. Hätönen, C. T. Freeman, D. H. Owens, P. L. Lewin, and E. Rogers. Robustness analysis of a gradient-based repetitive algorithm for discrete-time systems. In *43th Conference on Decision and Control*, pages 1301–1306, 2004.

J. J. Hätönen, C. T. Freeman, D. H. Owens, P. L. Lewin, and E. Rogers. A gradient-based repetitive control algorithm combining ILC and pole placement. *European Journal of Control*, 12(3):278–292, 2006.

B. W. Heller, A. J. Clarke, T. R. Good, T. J. Healey, S. Nair, and E. J. Pratt. Automated setup of functional electrical stimulation for drop foot using a novel 64 channel prototype stimulator and electrode array: results from a gait-lab based study. *Medical Engineering and Physics*, 35(1):74–81, 2013a.

B. W. Heller, A. J. Clarke, T. R. Good, T. J. Healey, S. Nair, E. J. Pratt, M. L. Reeves, and A. T. Barker. Automated setup of functional electrical stimulation for drop foot using a novel 64 channel prototype stimulator and electrode array: Results from a gait-lab based study. *Medical Engineering and Physics*, 35(1):74 – 81, 2013b.

O. A. Howlett, N. A. Lannin, L. Ada, and C. McKinstry. Functional Electrical Stimulation Improves Activity After Stroke: A Systematic Review With Meta-Analysis. *Archives of Physical Medicine and Rehabilitation*, 96(5):934 – 943, 2015.

W. Huaming, W. Yang, Y. Weidong, and Z. Yinlong. Implementation and application of a 2-dof dielectric elastomer actuator. In *IEEE International Conference on Cyber Technology in Automation, Control, and Intelligent Systems (CYBER)*, pages 1316–1320, 2015.

A. Hughes, J. Burridge, S. Demain, C. Ellis-Hill, C. Meagher, L. Tedesco-Triccas, R. Turk, and I. Swain. Translation of evidence-based Assistive Technologies into stroke rehabilitation: users' perceptions of the barriers and opportunities. *BMC Health Services Research volume*, 14(124), 2014.

HumanBodyforEducation. Diagram of a neuron, 2018. URL http://bodypics.club/diagram-of-a-neuron.

S. Hwang, J. Kim, J. Yi, K. Tae, K. Ryu, and Y. Kim. Development of an active ankle foot orthosis for the prevention of foot drop and toe drag. In *International Conference on Biomedical and Pharmaceutical Engineering*, pages 418–423, 2006.

D. Hyndman, A. Ashburn, and E. Stack. Fall events among people with stroke living in the community: Circumstances of falls and characteristics of fallers. *Archives of Physical Medicine and Rehabilitation*, 83(2):165 – 170, 2002.

M. Ilic, D. Vasiljevic, and D. B. Popovic. A programmable electronic stimulator for fes systems. *IEEE Transactions on Rehabilitation Engineering*, 2(4):234–239, Dec 1994.

V. Illingworth. *The Penguin Dictionary of Physics*. Penguin Books, 1991.

T. Inoue, M. Nakano, T. Kubo, S. Matsumoto, and H. Baba. High Accuracy Control of a Proton Synchrotron Magnet Power Supply. In *8th International Federation of Automatic Control world congress*, volume 14, pages 3137 – 3142, August 1981. 8th IFAC World Congress on Control Science and Technology for the Progress of Society, Kyoto, Japan, 24-28 August 1981.

Z. Z. Karu, W. K. Durfee, and A. M. Barzilai. Reducing muscle fatigue in fes applications by stimulating with n-let pulse trains. *IEEE Transactions on Biomedical Engineering*, 42(8):809–817, 1995. ISSN 0018-9294.

T. Keller. Textile neuroprosthesis garment for functional electrical stimulation. *International Workshop on Functional Electrical Stimulation*, 2007.

T. Keller and A. Kuhn. Electrodes for transcutaneous (surface) electrical stimulation. *Journal of Automatic Control*, 18, 01 2008.

S. Kelso. *Human Motor Behavior: An Introduction*. Psychology Press, 1982.

L. Kenney, B. Heller, A. Barker, M. Reeves, T. Good, N. Sha, S. Prenton, A. Liu, and D. Howard. A review of the design and clinical evaluation of the shefstim array-based functional electrical stimulation system. *Medical Engineering & Physics*, 38(11):1159 – 1165, 2016.

T. Kesar, L. Chouand, and S. Binder-Macleod. Effects of stimulation frequency versus pulse duration modulation on muscle fatigue. *Journal of electromyography and kinesiology*, 18:662 – 671, 2008.

S. Khurana, T. Ference, and A. Beranger. Comparison of functional electric stimulation neuroprosthesis and ankle foot orthosis in persons with multiple sclerosis. In *26th European Committee for Treatment and Research in Multiple Sclerosis Congress and 18th Rehabilitation in Multiple Sclerosis Meeting*, pages 2–5, 2013.

S. T. Kikuchi, S. Tanida, K. Otsuki, T. Yasuda, and J. Furusho. Development of third-generation intelligently controllable ankle-foot orthosis with compact mr fluid brake. In *IEEE International Conference on Robotics and Automation*, pages 2209–2214, 2010.

S. King. Is stroke care improving? *Second Annual Report Royal College of Physicians Sentinel Stroke National Audit Programme (SSNAP)*, 2015.

M. Kluding, K. Dunning, W. Michael, S. Wu, J. Ginosian, J. Feld, and K. McBride. Foot drop stimulation versus ankle foot orthosis after stroke. *Stroke*, 44(6), 2013.

H. Knotkova. *Practical Guide to Transcranial Direct Current Stimulation Principles, Procedures and Applications.* Springer International Publishing, 2019.

H. Kobravi and A. Erfanian. Decentralized adaptive robust control based on sliding mode and nonlinear compensator for the control of ankle movement using functional electrical stimulation of agonist–antagonist muscles. *Journal of Neural Engineering*, 6(4):046007, jul 2009.

A. Kostov, R. B. Stein, D. Popovic, and W. W. Armstrong. Improved Methods for Control of FES for Locomotion. *IFAC Proceedings Volumes*, 27(1):445 – 450, 1994. ISSN 1474-6670. IFAC Symposium on Modelling and Control in Biomedical Systems, Galveston, TX, USA, 27-30 March 1994.

H. I. Krebs, N. Hogan, M. L. Aisen, and B. T. Volpe. Robot-aided neurorehabilitation. *IEEE Transactions on Rehabilitation Engineering*, 6:75–87, 1998.

A. Kuhn, T. Keller, M. Lawrence, and M. Morari. The influence of electrode size on selectivity and comfort in transcutaneous electrical stimulation of the forearm. *IEEE Transactions on Neural Systems and Rehabilitation Engineering*, 18(3):255–262, June 2010.

E. Kurniawan. *Robust Repetitive Control and Applications.* PhD thesis, Swinburne University of Technology, 2013.

M. Lin L. Q. Zhang, D. Makhsous. Stiffness and viscous damping of the human leg. *American Society of Biomechanics*, 2000. Chicago.

R. P. Lane. Combined dropfoot treatment using dynamic splinting with fes: a case study. 2015.

F. Le, I. Markovsky, C. T. Freeman, and E. Rogers. Identification of the dynamics of human arms after stroke. In *23rd Annual workshop on advanced control diagnosis*, 2008.

F. Le, I. Markovsky, C. Freeman, and E. Rogers. System identification of muscle dynamics for ilc-based stroke rehabilitation. In *UKACC Research Student Event*, 2009.

F. Le, I. Markovsky, C. T. Freeman, and E. Rogers. Identification of electrically stimulated muscle models of stroke patients. *Control Engineering Practice*, 18(4):396 – 407, 2010.

D. Levine. *Whittle's Gait analysis.* Elsevier, 2012. D. Levine and J. Richards and M. W. Whittle.

L. Li, Z. Kuanyi, and U. R. Acharya. Fes controller design based on threshold control theory for single joint movement. In *1st Middle East Conference on Biomedical Engineering*, pages 304–307, Feb 2011.

C. Li-Wei and A. Binder-Macleod. The effects of stimulation frequency and fatigue on the force–intensity relationship for human skeletal muscle. *Clinical Neurophysiology*, 118(6):1387 – 1396, 2007.

W. T. Liberson, H. J. Holmquest, D. Scot, and M. Dow. Functional electrotherapy: stimulation of the peroneal nerve synchronized with the swing phase of the gait of hemiplegic patients. *Archives of Physical Medicine and Rehabilitation.*, 42(1):202–205, 1961.

T. Lin, D. H. Owens, and J. J. Hatonen. Newton method based iterative learning control for discrete non-linear systems. *International Journal of Control*, 79(10):1263–1276, 2006.

R. Longman. Iterative learning control and repetitive control for engineering practice. *International Journal of Control*, 73(10):930–954, 2000.

R. W. Longman. On the theory and design of linear repetitive control systems. *European Journal of Control*, 5:447–496, 2010.

T. Lu and S-H. Shiou. Inverses of 2 x 2 block matrices. *Computers and Mathematics with Applications*, 43:119–129, 2002.

G. M. Lyons, G. E. Lane, M. Clarke-Maloney, J. V. O'Brien, and P. A. Grace. An investigation of the effect of electrode size and electrode location on comfort during stimulation of the gastrocnemius muscle. *Medical Engineering and Physics*, 26(10): 873–878, 2004.

G. Mann, J. Burridge, L. Malone, and P. Strike. A pilot study to investigate the effects of electrical stimulation on recovery of hand function and sensation in subacute stroke patients. *Neuromodulation: Technology at the Neural Interface*, 8(3):193–202, 2005.

L. Marc. *Transcutaneous Electrode Technology for Neuroprostheses.* phdthesis, Eth Zaœrich, 2009.

M. G. Mataee and M. Andani, M. T.and Elahinia. Adaptive ankle-foot orthoses based on superelasticity of shape memory alloys. *Journal of Intelligent Material Systems and Structures*, 26(6), 2014.

L. Mesin, E. Merlo, R. Merletti, and C. Orizio. Investigation of motor unit recruitment during stimulated contractions of tibialis anterior muscle. *Journal of Electromyography and Kinesiology.*, 20(4):580 – 589, 2010.

S. Micera, T. Keller, M. Lawerence, M. Morari, and D. B. Popovic. Wearable neural prosthesis: Restoration od sensory-motor function by transcutaneous electrical stimulation. *IEEE Engneering in Medicine and Biology Magazine*, pages 64–69, May/June 2010.

L. Miller, A. McFadyen, A. C. Lord, R. Hunter, L. Paul, D. Rafferty, R. Bowers, and P. Mattison. Functional Electrical Stimulation for Foot Drop in Multiple Sclerosis: A Systematic Review and Meta-Analysis of the Effect on Gait Speed. *Archives of Physical Medicine and Rehabilitation*, 98(7):1435 – 1452, 2017.

M. Moltedo, T. Bacek, T. Verstraten, C. Rodriguez-Guerrero, B. Vanderborght, and D. Lefeber. Powered ankle-foot orthoses: the effects of the assistance on healthy and impaired users while walking. *Journal of NeuroEngineering and Rehabilitation*, 15 (86), 2018.

R. Momosaki, M. Abo, S. Watanabe, W. Kakuda, N. Yamadaand, and S. Kinoshita. Effects of ankle–foot orthoses on functional recovery after stroke: A propensity score analysis based on japan rehabilitation database. *PLoS ONE*, 10:e0122688, 04 2015.

P. Morasso. Spatial control of arm movements. *Experimental Brain Research*, 42(2): 223–227, Apr 1981.

M. Munih, K. Hunt, and N. Donaldson. Variation of recruitment nonlinearity and dynamic response of ankle plantarflexors. *Medical Engineering and Physics*, 22(2):97 – 107, 2000.

N. Negrd. *Controlled FES-assisted gait training for hemiplegic stroke patients based on inertial sensors*. PhD thesis, TU Berlin, 2009.

V. Nekoukar and A. Erfanian. A decentralized modular control framework for robust control of fes-activated walker-assisted paraplegic walking using terminal sliding mode and fuzzy logic control. *IEEE Transactions on Biomedical Engineering*, 59(10):2818–2827, Oct 2012.

R. Neptune and K. Sasaki. Ankle plantar flexor force production is an important determinant of the preferred walk-to-run transition speed. *Journal of Experimental Biology*, 208(5):799–808, 2005.

M. Neuman. *Biopotential Electrodes - The Biomedical Engineering Handbook: Second Edition.* CRC Press LLC, 2000.

NICE. Functional electrical stimulation for drop foot of central neurological origin. Website, January 2009. URL https://www.nice.org.uk/Guidance/IPG278. National Institute for Health and Clinical Excellence.

S. B. O'Dwyer, D. T. O'Keeffe, S. Coote, and G. M. Lyons. An electrode configuration technique using an electrode matrix arrangement for fes-based upper arm rehabilitation systems. *Medical Engineering Physics*, 28:166–176, 2006.

T. R. Oliveira, L. R. Costa, and A. V. Pino. Extremum Seeking applied to Neuromuscular Electrical Stimulation. *Cyber-Physical and Human-Systems*, 49(32):188 – 193, 2016.

A. P. Page and C. T. Freeman. Point-to-point repetitive control of functional electrical stimulation for drop-foot. *Control Engineering Practice*, 96:104280, 2020.

A. P. Page, C. T. Freeman, and B Chu. Weighted point-to-point repetitive control for drop-foot assistance. In *UKACC 12th international conference on control*, pages 468–473, 2018a.

A. P. Page, C. T. Freeman, and B Chu. Point-to-point repetitive control with application to drop-foot. in 2018 european control conference. In *European Control Conference,*, pages 2399–2404, 2018b.

Y. L. Park, B. R. Chen, N. O. Perez-Arancibia, D. Young, L. Stirling, R. J. Wood, E. C. Goldfield, and R. Nagpal. Design and control of a bio-inspired soft wearable robotic device for ankle-foot rehabilitation. *Bioinspir Biomim*, 9(1):016007, 2014.

E. W. Peterson. Fear of falling and associated activity curtailing among middle aged and older adults with multiple scleosis. *Multiple Sclerosis*, 13:1168–1175, 2007.

G. Pipeleers and K. L. Moore. Unified analysis of iterative learning and repetitive controllers in trial domain. *IEEE Transactions on Automatic Control*, 59(4):953–965, 2014.

D. Popovic, R. Tomovic, and L. Schwirtlich. Hybrid assistive system-the motor neuroprosthesis. *IEEE Transactions on Biomedical Engineering*, 36(7):729–737, 1989.

D. B Popović and M. B. Popović. Automatic determination of the optimal shape of a surface electrode: Selective stimulation. *Journal of Neuroscience Methods*, 178(1): 174–181, 2009.

A. Popović-Bijeli, G. Bijeli, N. Jorgovanovi, D. Bojanic, M. B. Popović, and D. B. Popović. Multi-field surface electrode for selective electrical stimulation. *Artificial Organs*, 29(6):448–452, 2005.

N. Postans and M. Granat. Effect of functional electrical stimulation, applied during walking, on gait in spastic cerebral palsy. *Developmental Medicine and Child Neurology*, 47(1):46–52, 2005.

E. Pourhosseingholi, B. Farahmand, A. Bagheri, M. Kamali, and M. Saeb. Efficacy of different techniques of AFO construction for hemiplegia patients: A systematic review. *Medical journal of the Islamic Republic of Iran*, 33:50, 06 2019.

S. Prenton, L.P. Kenney, C. Stapleton, G. Cooper, M.L. Reeves, B.W. Heller, M. Sobuh, A.T. Barker, J. Healey, T.R. Good, Sibylle B. Thies, and T. Howard, D.and Williamson. Feasibility study of a take-home array-based functional electrical stimulation system with automated setup for current functional electrical stimulation users with foot-drop. *Archives of Physical Medicine and Rehabilitation*, 95(10): 1870–1877, 2014.

S. Prenton, K. Hollands, L. Kenney, and P. Onmanee. Functional electrical stimulation and ankle foot orthoses provide equivalent therapeutic effects on foot drop: A meta-analysis providing direction for future research. *Journal of Rehabilitation Medicine*, 50:129–139, 2017.

M. H. Ramlee, M. R. A. Kadir, and H. Harun. Three-dimensional modeling and analysis of a human ankle joint. In *IEEE Student Conference on Research and Developement*, pages 74–78, 2013.

J. Ratcliffe, P. Lewin, E. Rogers, J. Hätönen, and D. Owens. Norm-Optimal Iterative Learning Control Applied to Gantry Robots for Automation Applications. *IEEE Transactions on Robotics and Automation*, 22(6):1303–1307, 2006.

J. Ratcliffe, J. Hätönenand P. Lewin, and E. Rogersand D. Owens. Repetitive control of synchronized operations for process applications. *International Journal of Adaptive Control and Signal Processing*, 21(4):300–325, 2007.

A. Roche, G. O. Laighin, and S. Coote. Surface-applied functional electrical stimulation for orthotic and therapeutic treatment of drop-foot after stroke: a systematic review. *Physical Therapy Reviews*, 14(2), 2009.

E. J. Rouse, R. D. Gregg, L. J. Hargrove, and J. W. Sensinger. The difference between stiffness and quasi-stiffness in the context of biomechanical modeling. *IEEE Trans. Biomed. Eng.*, pages 562–568, 2013.

D. N. Rushton. Functional Electrical Stimulation and rehabilitation - an hypothesis. *Medical Engineering and Physics*, 25(1):75–78, 2003. ISSN 1350-4533.

O. Schill, R. Rupp, C. Pylatiuk, S. Schulz, and M. Reischl. Automatic adaptation of a self-adhesive multi-electrode array for active wrist joint stabilization in tetraplegic SCI individuals. In *Science and Technology for Humanity (TIC-STH), 2009 IEEE Toronto International Conference*, pages 708 –713, 2009.

T. Seel, C. Werner, J. Raisch, and T. Schauer. Iterative learning control of a drop foot neuroprosthesis generating physiological foot motion in paretic gait by automatic feedback control. *Control Engineering Practice*, 48(3):87–97, 2016.

K. Shamaei, M. Cenciarini, A. A. Adams, K. N. Gregorczyk, J. M. Schiffman, and A. M. Dollar. Design and evaluation of a quasi-passive knee exoskeleton for investigation of motor adaptation in lower extremity joints. *IEEE Transactions on Biomedical Engineering*, 61(6):1809–1821, 2014.

G. J. Snoek, M. J. IJzerman, F. A. in 't Groen, T. S. Stoffers, and G. Zilvold. Use of the NESS Handmaster to restore handfunction in tetraplegia: clinical experiences in ten patients. *Spinal Cord*, 38:244–249, 2000.

L. Stirling, Chih-Han. Yu, J. Miller, E. Hawkes, R. Wood, E. Goldfield, and R. Nagpal. Applicability of shape memory alloy wire for an active, soft orthotic. *Journal of Materials Engineering and Performance*, 20(4):658–662, 2011.

L. Sun, Y. Sun, Z. Huang, J. Hou, and J. Wu. A hill-type submaximally-activated musculotendon model and its simulation. In *14th International Symposium on Distributed Computing and Applications for Business, Engineering and Science*, pages 439–442, 2015.

G. Tack, J. S. Choi, J. H. Yi, and C. H. Kim. Relationship between Jerk Cost Function and Energy Consumption during Walking. pages 2917–2918, 2007.

A. K. Tangirala. *Principles of System Identification: Theory and Practice*. CRC Press, 2018. ISBN 9781439896020.

P. Taylor, J. Burridge, A. Dunkerley, A. Lamb, D. Wood, J. Norton, and I. Swain. Patients' perceptions of the odstock dropped foot stimulator (odfs). *Clinical Rehabilitation*, 13(5):439–446, 1999.

X. Tu, J. Huang, and J. He. Leg hybrid rehabilitation based on hip-knee exoskeleton and ankle motion induced by fes. In *2016 International Conference on Advanced Robotics and Mechatronics (ICARM)*, pages 237–242, 2016.

S. F. Tyson, E. Sadeghi-Demneh, and C. J. Nester. A systematic review and meta-analysis of the effect of an ankle-foot orthosis on gait biomechanics after stroke. *Clinical Rehabilitation*, 27(10):879–891, 2013.

C. L. Vaughan, B. L. Davis, and J. C.Connor. *Dynamics of Human Gait*. Kiboho Publishers, 1999.

J. M. Veerbeek, van E. Wegen, R. Peppen, P. J. van der Wees, E. Hendriks, M. Rietberg, and G. Kwakkel. What is the evidence for physical therapy poststroke? A systematic review and meta-analysis. *PLoS ONE*, 9(2):e87987, February 2014.

R. Velik, N. Malesevic, L. Maneski, U. Hoffmann, and T. Keller. A Multi-pad Electrode System for Selective Transcutaneous Electrical Muscle Stimulation. In *INTFES*, 01 2011.

Y. Wang, F. Gao, and F. Doyle. Survey on iterative learning control, repetitive control, and run-to-run control. *Journal of Process Control*, 19(10):1589 – 1600, 2009.

L. Bakerand L. Wederich, R. Mcneal, C. Newsam, and L. Waters. *Neuromuscular electrical stimulation: A practical guide*. Los Amigos Research & Education Institute, Inc, 2000.

F. Westhout, L. Paré, and M. Linskey. Central causes of foot drop: rare and underappreciated differential diagnoses. *The journal of spinal cord medicine*, 30:62–66, 2007.

K. Yang, C. Freeman, R. Torah, S. Beeby, and J. Tudor. Screen printed fabric electrode array for wearable functional electrical stimulation. *Sensors and Actuators A: Physical*, 213:108–115, January 2014a. ISSN 0924-4247.

K. Yang, C. T. Freeman, R. N. Torah, S. P. Beeby, and J. Tudor. Screen Printed Fabric Electrode Array for Wearable Functional Electrical Stimulation. *Sensors and Actuators A: Physical*, 213:108–115, 2014b.

K. Yang, K. Meadmore, C. Freeman, N. Grabham, A. Hughes, Y. Wei, R. Torah, M. Glanc-Gostkiewicz, S. Beeby, and J. Tudor. Development of user-friendly wearable electronic textiles for healthcare applications. *Sensors*, 18:2410, 07 2018.

K. Yang, B. Isaia, L. Brown, and S. Beeby. E-textiles for healthy ageing. *Sensors*, 19 (20), October 2019a.

K. Yang, M. Liu, T. Ward, D. Young, H. Matos, W. Yang, and J. Adams. Electronic textiles based wearable electrotherapy for pain relief. *Sensors and Actuators A: Physical*, November 2019b.

W. Young. Electrical stimulation and motor recovery. *Cell Transplantation*, 24(3): 429–446, 2015.

H. Zhang, J. Qian, L. Shen, and Y. Zhang. Research on healthy subject gait cycle phase at different walking speeds. In *IEEE International Conference on Robotics and Biomimetics*, pages 1349–1354, 2012.